Advanced Electromagnetic Modelling of the Next Generation (XG) Wireless Communication Systems

Ozzola, R.

DOI
10.4233/uuid:a8cb99b1-961c-486d-b3d3-2f2f8eb96136

Publication date
2024

Document Version
Final published version

Citation (APA)
Ozzola, R. (2024). *Advanced Electromagnetic Modelling of the Next Generation (XG) Wireless Communication Systems*. [Dissertation (TU Delft), Delft University of Technology]. https://doi.org/10.4233/uuid:a8cb99b1-961c-486d-b3d3-2f2f8eb96136

Advanced Electromagnetic Modelling of the Next Generation (XG) Wireless Communication Systems

Riccardo Ozzola

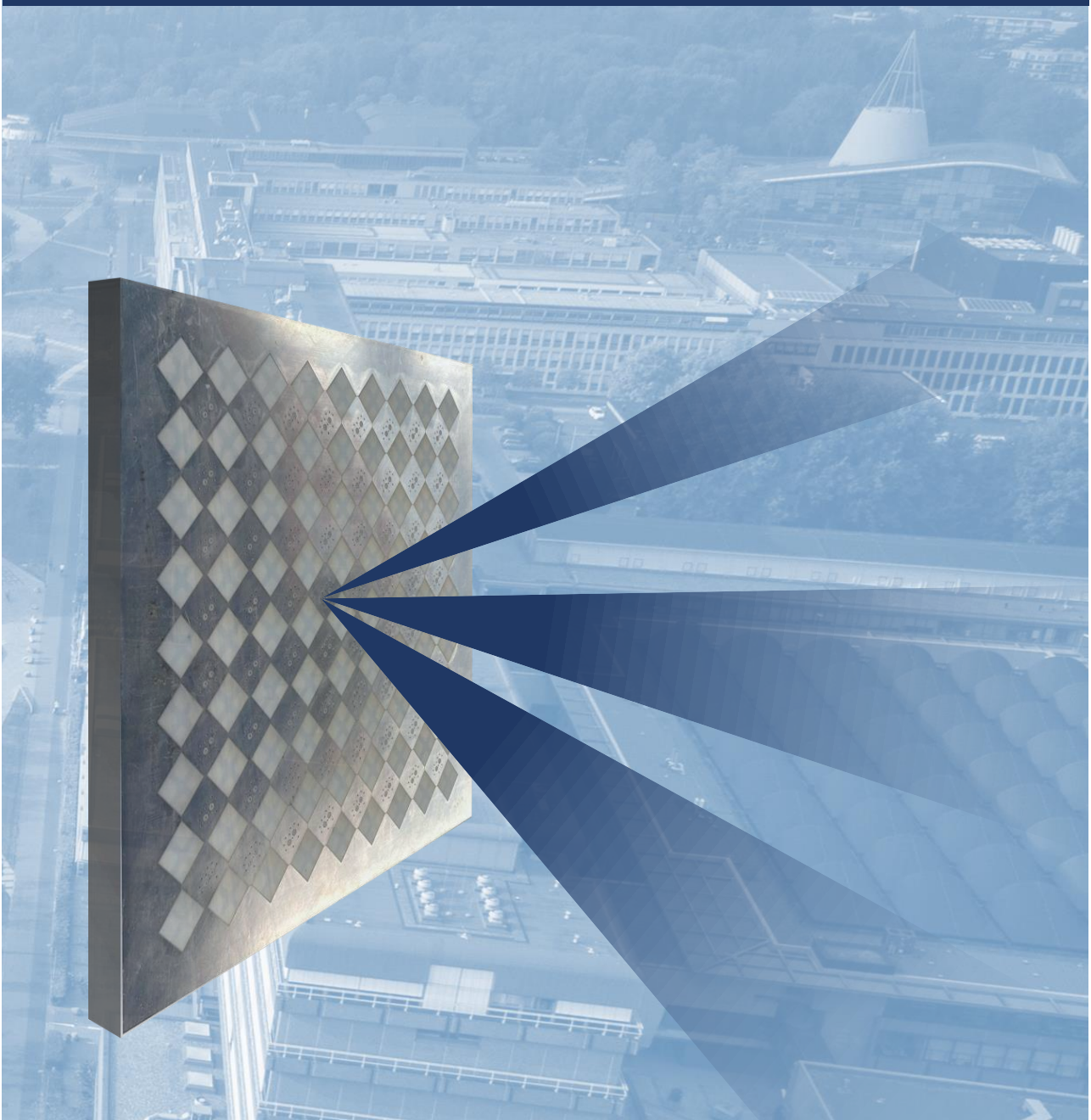

Advanced Electromagnetic Modelling of the Next Generation (XG) Wireless Communication Systems

Advanced Electromagnetic Modelling of the Next Generation (XG) Wireless Communication Systems

DISSERTATION

for the purpose of obtaining the degree of doctor
at Delft University of Technology
by the authority of the Rector Magnificus, Prof. dr. ir. T. H. J. J. van der Hagen,
Chair of the Board for Doctorates,
to be defended publicly on
Monday 21 October 2024 at 17:30

by

Riccardo OZZOLA

Master of Science in Telecommunications Engineering,
University of Florence, Italy,
born in Bibbiena, Italy.

This dissertation has been approved by the promotors.

Composition of the doctoral committee:

Rector Magnificus,	Chairperson
Prof. dr. ing. A. Neto,	Delft University of Technology, promotor
Dr. D. Cavallo,	Delft University of Technology, promotor
Independent members:	
Prof. dr. N. Llombart Juan	Delft University of Technology
Prof. dr. ir. M. C. van Beurden	Eindhoven University of Technology
Dr. G. Carluccio	NXP Semiconductors
Prof. A. Freni	University of Florence
Prof. dr. O. Quevedo-Teruel	KTH Royal Institute of Technology
Reserve member:	
Prof. dr. J. J. A. Baselmans	Delft University of Technology

The work presented in this dissertation has been performed at Delft University of Technology, and financed by Huawei Technologies Sweden AB, under the Grant YBN2020045031.

Keywords:	antennas, phased arrays, MIMO systems, 5G, 6G, computational electromagnetics, applied electromagnetics
Cover design:	showcase of the different objects of the modelling: the connected array, MIMO communications, the printed dipole with nonzero metal thickness, and lens antennas. The aerial view of the campus was provided by TU Delft. Cover design by R. Ozzola, G. Ozzola, and dr. D. Cavallo.
Printed by:	Ipskamp Drukkers B. V., Enschede – The Netherlands

An electronic version of this dissertation is available at https://repository.tudelft.nl/

ISBN 978-94-6384-633-2

To my parents

L'ottimismo che viene dalla conoscenza
The optmimism which comes from knowledge
–Prof. Guido Silvestri

Contents

Summary

The expectation is that XG communications will have a disruptive impact in their applications in smart cities, industrial automation, agriculture, e-health, smart grids, domotics, and autonomous driving. However, such scenarios imply the availability of technology that cannot be met resorting to incremental changes in present techniques. Specifically, it is now apparent that the ultrawideband massive MIMO in both the microwave and sub-THz bands will be needed.

By exploiting larger bandwidths, unprecedented data rates will be achieved for MIMO applications in the microwave band. Before this work, wideband arrays have been considered unsuitable for MIMO applications due to the high levels of inter-elements mutual coupling. However in this work it has been proven that if the entire array is coherently excited, multiple orthogonal beams can be generated, regardless of the inter-element mutual coupling. The orthogonality levels depend solely on the beam overlap and, therefore, on the beam width, the side lobes, and the position of the nulls.

Moreover, a wideband phased array has been designed for sub-8 GHz MIMO communications. The array is realized in the form of a dual-polarized connected slot array with interchangeable Artificial Dielectric Layers (ADLs) radome. This allows the array to scan up to 60° in every azimuthal cut while being matched between 6 and 8 GHz with the first radome, and 2 and 8 GHz with the second one. Finally, an 8×8 prototype is manufactured and tested.

Due to the long wavelength at microwave bands, the antenna size is the largest constraint when it comes to MIMO applications, especially for wideband operations. To this aim, a new metric is developed to assess the signal and the interference of MIMO antennas constrained within a given volume. This allows us to compare the performance of an intended antenna design or even a realized prototype to the one of the maximum gain antenna located within the given volume. By means of these concepts, it is possible to link the MIMO performance with the antenna size to optimize the space.

By exploiting larger bandwidths, unprecedented data rates will be achieved for MIMO applications in the microwave band.

The second road to high data rates for MIMO application is the use of higher frequencies (sub-THz) communications. The main hindrance to integrated antennas for this regime is the technological challenge due to microfabrication and the integration with the electronics. This calls for accurate simulations that enable optimal designs.

For this purpose, an integral equation solver was developed to study dielectric lenses together with their feeds. At high frequency, the thickness of the metal plays an important role and cannot be neglected. Due to the different scales involved in the feed and in the lens, the required computational effort might be prohibitive. Therefore, a method has been devised to combine the numerical solution with analytical results to enable large-scale simulations. The impedance of an integrated antenna can be seen as composed of the reactance of the feed, the impedance of the feed radiating in a semi-infinite space without reflections, and an impedance associated with the reflections. While the former two can be evaluated analytically or with fast numerical simulations, the latter requires a time-intensive full-wave simulation of the entire problem. However, this can be simplified by synthesizing a much coarser feed, which radiates equivalently into the semi-infinite medium. Having this much coarser discretization it allows us to simplify the simulation of the entire problem and to isolate the reflections conveniently. Then, all the components can be combined together, and the input impedance can be estimated accurately.

Samenvatting

De verwachting is dat XG-communicatie een ontwrichtend effect zal hebben op toepassingen in slimme steden, industriële automatisering, landbouw, e-gezondheid, slimme netwerken, domotica en autonoom rijden. Dergelijke scenario's impliceren echter de beschikbaarheid van technologie waaraan niet kan worden voldaan door middel van incrementele veranderingen in de huidige technieken. Het is nu met name duidelijk dat ultrabreedband massieve MIMO in zowel de microgolf- als de sub-THz-banden nodig zal zijn.

Door gebruik te maken van grotere bandbreedtes zullen ongekende datasnelheden worden bereikt voor MIMO-toepassingen in de microgolfband. Vóór dit werk werden breedbandige arrays ongeschikt geacht voor MIMO-toepassingen vanwege de sterke onderlinge koppeling tussen de elementen. In dit werk is echter aangetoond dat als de hele array coherent wordt geëxciteerd, er meerdere orthogonale stralingsbundels kunnen worden gegenereerd, ongeacht de onderlinge koppeling tussen de elementen. De orthogonaliteitsniveaus hangen alleen af van de overlap van de bundel en dus van de bundelbreedte, de zijlobben en de positie van de nullen.

Bovendien is er een breedbandige fase-gestuurde array ontworpen voor sub-8 GHz MIMO-communicatie. De array is gerealiseerd in de vorm van een dubbel lineair gepolariseerde verbonden gleuf array met verwisselbare kunstmatige diëlektrische lagen (ADL's) radome. Hierdoor kan de array tot 60° in elke azimutale snede scannen terwijl die afgestemd blijft tussen 6 en 8 GHz met de eerste radome, en 2 en 8 GHz met de tweede. Tenslotte wordt een prototype van 8×8 elementen gefabriceerd en getest.

Vanwege de lange golflengte op de microgolfbanden is de antennegrootte de voornaamste beperking als het gaat om MIMO-toepassingen, vooral voor breedbandig gebruik. Met het oog hierop is een nieuwe metriek ontwikkeld om het signaal en de interferentie van MIMO-antennes met een bepaald volume te beoordelen. Dit stelt ons in staat om de prestaties van een beoogd antenneontwerp of zelfs een gerealiseerd prototype te vergelijken met die van de antenne met maximale versterking binnen het gegeven volume. Met behulp van deze concepten is het mogelijk om de

MIMO-prestaties te koppelen aan de antenneafmetingen om de gebruikte ruimte te optimaliseren.

De tweede weg naar hoge datasnelheden voor MIMO-toepassingen is het gebruik van communicatie op hogere frequenties (sub-THz).

Het belangrijkste obstakel voor geïntegreerde antennes in dit deel van het spectrum is de technologische uitdaging als gevolg van microfabricage en de integratie met de elektronica. Dit vraagt om nauwkeurige simulaties die optimale ontwerpen mogelijk maken.

Hiervoor werd een integraalvergelijkingsoplosser ontwikkeld om diëlektrische lenzen samen met hun voeding te bestuderen. Bij hoge frequenties speelt de dikte van het metaal een belangrijke rol die niet verwaarloosd kan worden. Door het grote verschil in relevante afmetingen tussen de voeding en de lens kan de benodigde rekenkracht onhaalbaar zijn. De impedantie van een geïntegreerde antenne kan worden gezien als opgebouwd uit de reactantie van de voeding, de impedantie van de voeding die straalt in een semi-oneindige ruimte zonder reflecties, en een impedantie geassocieerd met de reflecties. Terwijl de eerste twee analytisch of met snelle numerieke simulaties kunnen worden geëvalueerd, vereist de laatste een tijdrovende volledige-golfsimulatie van het hele probleem. Dit kan echter vereenvoudigd worden door een veel grovere voeding te synthetiseren, die equivalent uitstraalt in het semi-oneindige medium. Met deze veel grovere discretisatie kunnen we de simulatie van het hele probleem vereenvoudigen en de reflecties gemakkelijk isoleren. Vervolgens kunnen alle componenten worden gecombineerd en kan de ingangsimpedantie nauwkeurig worden geschat.

Preface

This dissertation describes the research work carried out at the THz Sensing Group of the Delft University of Technology over a period of four years (from May 2020 to April 2024).

The research shown in this dissertation was supported by HUAWEI Sweden AB, under the contract YBN2020045031.

Riccardo Ozzola
Delft, May 2024

Chapter 1

Introduction

Conoscere per deliberare
You have to know before you decide
–Luigi Einaudi

1.1. The Next Generation (XG) of Mobile Communications

The fifth generation (5G) and beyond (XG) of mobile communications are meant to provide low-latency and high data rate connectivity for consumer services (e.g., ultra-HD video streaming, virtual and augmented reality, and cloud gaming) and for several new services and applications such as smart cities, industrial automation, smart agriculture, e-health, smart grids, smart homes, and autonomous driving [1–5].

Due to their prospected revolutionary performance and extensive applications, 5G and XG will have a massive economic and societal impact. It was estimated that the adoption of 5G will contribute to $3 trillion to the global Gross Domestic Product by 2030 [6]. In the three-year period 2022-2025, $600 billion will be invested by mobile operators to upgrade their network infrastructure to 5G [7]. Due to their application in healthcare, manufacturing processes, logistics, domotics, and farming, XG communications are aligned with the United Nations' Sustainable Development Goals [8].

On the technical standpoint, the new revolutionary applications need a high data rate, low latency, ubiquitous, reliable, and efficient network, and such requirements can be met only through radical innovations in the network architecture and its de-

ployment [9, 10], signal processing [11], receiver and transmitter front ends [12–15], accurate link budget modeling [16, 17], and advanced antenna architectures [18–24].

The new requirements on the links' capacity call for the vast exploitation of the massive Multiple Input-Multiple Output (MIMO) paradigms, which allows for the creation of multiple and independent space channels. This has pushed for advancement in the research of low-complexity multibeam antennas and their development [18, 21–25] and in the modeling of MIMO or innovative links [26, 27].

The crowdedness of the microwave spectrum and the different quality of service and requirements needed by the network deployment call for the use of new frequency bands for either the microwave, the millimeter wave, and the sub-THz regime [1–4, 28–30]. In particular, thanks to the large bandwidth available, the mm- and sub mm-wave have emerged as the candidate bands for ultra high-speed data rate applications [26, 31, 32], and this has pushed for the development of high-frequency antennas [20, 22, 24, 31, 33–35].

Moreover, the ambitious data rate requirements and the ubiquitous connectivity have required to upgrade propagation scenarios, at every frequency, into smart radio environments to enhance the connectivity [23, 36, 37].

High user density environments, e.g., the stadium and the auditorium in Fig. 1.1(a) and (b), are the most demanding scenarios for high quality of service communications. The issue of establishing links in these challenging scenarios can be addressed either in the sub-THz and in the microwave spectrum. The former case is presented in [31], where numerous lenses are used to radiate narrow beams in the one-beam-per-lens configuration, as sketched in 1.1(c). Due to the high-frequency use, high-gain antennas can be designed in a compact volume, allowing for easy maximization of the independent data streams. However, this configuration suffers from the technological constraints of the manufacturing technologies, the challenging integration with the electronics, and the efficiency of the front-ends. Therefore, it becomes fundamental to devise efficient tools and accurate simulation strategies to obtain effective designs to exploit the potentiality of the sub-THz spectrum. The latter case, i.e., microwave links, can achieve similar performance with wideband operation through wideband phased arrays. Antenna manufacturing technologies are mature in the microwave regime, where, in turn, mutual coupling issues constitute the biggest hindrance. In fact, the longer wavelength is such that the antenna size is the main constraint, as the electrical size widens the antenna patterns, creating interference and reducing the number of independent spatial channels [see Fig. 1.1(d)]. Therefore, it is crucial to assess the limits of an antenna with respect to its physical dimension, especially when operating over a wide bandwidth.

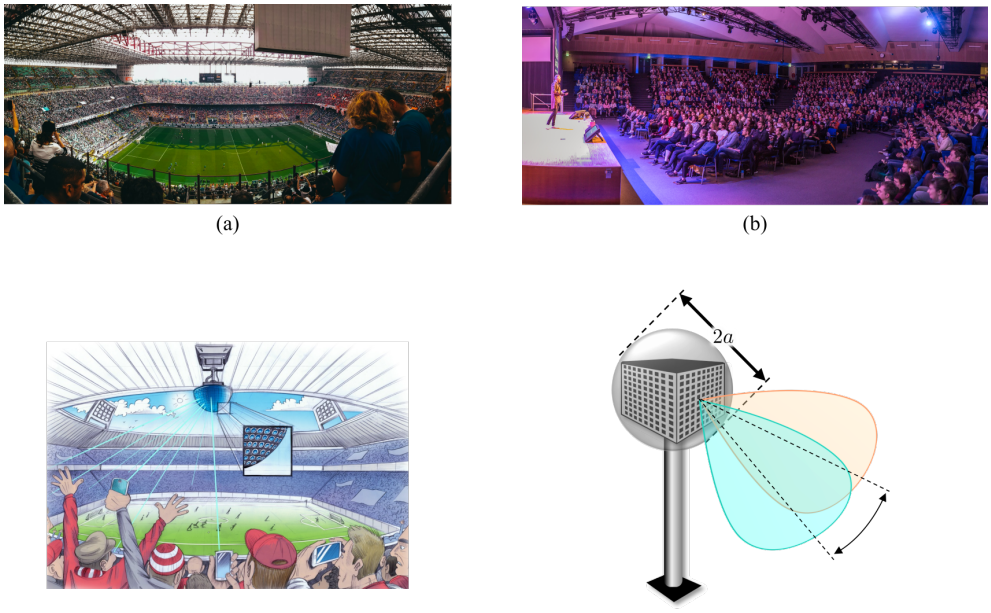

Figure 1.1: Photo of a crowded (a) football stadium and (b) auditorium (photo of the auditorium provided by TU Delft), (c) sketch of the example of a massive MIMO scenario for a stadium obtained with high-frequency lenses (courtesy of [38]), and (d) beam overlap for microwave wideband phased arrays.

1.2. The Modelling and Design of Wideband Massive MIMO Phased Arrays

1.2.1. Wideband Phased Arrays

Differently from the previous standards, in 5G multiple frequency bands are being licensed as shown in Fig. 1.2(a), and this aspect calls for the integration of multiple antennas on the same site. However, this yields an increased site complexity and occupied space, leading to higher installation, maintenance, and renting costs. These concerns are valid throughout the entire frequency spectrum but are of utmost importance in the sub-8 GHz band due to the large physical size of the antennas. For these reasons, there is an increasing interest in antennas that integrate multiple frequency bands in the same aperture.

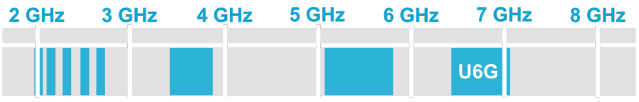

(a)

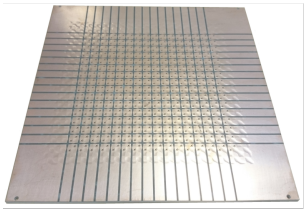

(b)

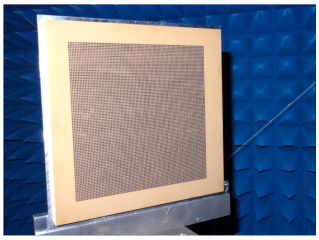

(c)

Figure 1.2: (a) Licensed bands in the sub-8 GHz spectrum, and photo of (a) a PCB connected slot array and (b) the connected array with its ADL superstrate (courtesy of [41]).

In this thesis, connected arrays [39, 40] with Artificial Dielectric Layers (ADLs), as the one shown in Fig. 1.2(b) and (c), have been chosen as wideband array concept. In fact, these wideband antennas can be realized in multi-layer Printed Circuit Board (PCB) implementation as in [41–43], and can be combined with ADLs to extend the operation bandwidth and the antenna scanning volume. The design results in considerably complex antenna assemblies, which are extremely challenging to study with commercial solvers alone. However, connected array unit cells can be conveniently studied thanks to their active impedance closed form formula [39, 40], and their equivalent circuit [44]. In addition to this, the presence of the ADLs radomes can be easily accounted for in the stratified media Green's function [45], also thanks to the analytical susceptance describing each layer, which considers the inter-layer effects [46–50]. Furthermore, thanks to the equivalent transmission line description of the layered media problem, the ADL stack's realistic dielectric and bond layers can also be efficiently included in the simulation, allowing for fast design cycles.

The modelling of connected array and ADLs was developed in previous works and used in this dissertation to design a wideband array for MIMO applications.

1.2.2. Wideband Massive MIMO

The need for a high data rate has called for the exploitation of massive MIMO [9, 51] and for the research of innovative MIMO concepts [52–54]. The growing complexity of the scenario and the hardware architecture and the use of advanced electromagnetic techniques in MIMO have called for increasing attention to the electromagnetic

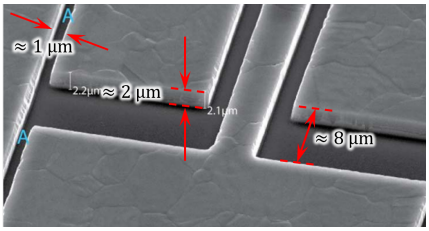

Figure 1.3: Detail of an on-chip 0.3 THz antenna. Courtesy of [60].

modeling of MIMO systems [5, 26, 52–59]. More specifically, [52] has drawn the attention on the use of connected arrays to maximize the data rate, by exploiting unprecedentedly larger bandwidths. Over its wide operation bandwidth, the antenna cannot hold the same high-gain performance, which can ensure low-interference data streams. Therefore, assessing the MIMO performance concerning the antenna's electrical size becomes crucial for its applicability. Moreover, connected arrays are notoriously known for their high mutual coupling, which is required for their wideband operation, and because of this, their use in MIMO is questioned.

1.3. The Modelling of High Frequency Integrated Antennas

At sub-THz frequencies, the antenna manufacturing relies on integrated technologies. Due to the micrometric designs, the thickness of the metallization can be comparable with the features of the design, such as track and gap width, as for instance in the double slot in [60], as shown in Fig. 1.3, and invalidating the assumptions on the use of planar components. In fact, the metal thickness can affect the characteristic impedance and the losses of the feeding lines, and it can carry strong capacitive effects in the feeding gaps, which can impact the input impedance. Such modeling has to include features, such as, for instance, the metal thickness and the feed length, which present different sizes at very different scales. Such modeling can be performed with state-of-the-art full-wave numerical solvers, e.g., [61, 62], at the expense of cumbersome simulations, also considering that the problem might be ill-conditioned, due to the decreasing size of the basis functions, used to represent the thin metallization. Due to these limitations, the simulations can become exceptionally challenging when dealing with lens antennas, constituted by inhomogeneous dielectrics, and whose diameter is in the order of some wavelengths [63, 64]. For these reasons, asymptotic techniques [65–77] are often used for the analysis of lens antennas. However, the telecommunication requirements and the technological challenges of mm-waves and

sub-THz frequency have pushed for the use of small lens antennas [78], to ease their front-end integration [63, 64] and to be employed in the scan lens array configuration [33, 79]. However, for small lens antennas, the accuracy of asymptotic techniques decreases [77], inherently leaving a void in the analysis tools, as, on the other hand, full-wave solvers can be excessively slow.

For these reasons, a technique that can hybridize numerical solvers with semi-analytical solutions is a winning strategy for such applications. In practice, a deep understanding of the problem allows to formulate a semi-analytical solution, which simplifies the model, simulated at enhanced speed in a second step with the numerical solver. Finally, the complete solution can be reconstructed by combining the semi-analytical solution with the numerical one.

1.4. The Scientific Contribution of This Thesis

This thesis has brought to the antenna and telecommunication community the following scientific contributions.

In Part I

- The theory to assess how many beams can be generated, for a target signal-to-interference ratio, from a massive MIMO antenna. It, therefore, links the size of the antenna platform to the maximum number of space channels that can be established;

- If the entire array is excited coherently, orthogonal antenna patterns can be obtained in a massive MIMO system regardless of the inter element mutual coupling. Therefore, wideband phased arrays can be used in MIMO systems. The orthogonality levels depend only on the beam overlap and are affected by the beamwidth and the sidelobes;

- The design and manufacturing of a connected array combined with interchangeable ADL radomes, allowing it to operate over different frequency bands. It shows how, in a phased array design, the radiating antenna section can be decoupled from the matching radome. This proves the flexibility of connected arrays with artificial dielectric layers radomes, and it constitutes a scalable and appealing solution for commercial applications;

- An alternative formulation of the aperture efficiency is defined. This quantity is calculated by resorting to the observable field, and it is bounded by unity, regardless the antenna size. Therefore, it constitutes an absolute metric to assess the effectiveness of an antenna design;

- The closed form formula of a singularity-free Green's function, which can be used to calculate the mutual coupling of the far-field patterns in a multi beam configuration.

In Part II

- The equivalent circuit of an antenna radiating in proximity to a dielectric body is derived. The input impedance is constituted by three components: the reactance of the feed, the impedance of the antenna in the absence of the reflections, i.e., when radiating into a dielectric half space, and a term accounting for the reflections given by the discontinuity of the finite size dielectric;
- The previously derived equivalent circuit yields an efficient full wave analysis of integrated antennas with the proxy sources method. This allows for the analysis of integrated antennas combining the reactance of the feed, the reflectionless impedance, and the reflection term extracted from a much coarser and faster simulation;
- The semi-analytical description of the current spectrum of an infinitely long dipole with nonzero metal thickness is derived. This constitutes an effective tool for the analysis of printed microstrips at sub-THz frequencies, where the metal thickness is comparable with the design parameters;
- The different spectral contributions of the current in an infinitely long dipole are analyzed, allowing us to derive an equivalent circuit that takes into account the reactance of the feeding gap and the propagation along the dipole;
- The semi-analytical description of the infinitely long dipoles is extended to the analysis of finite length dipoles radiating in layered media.

1.5. Thesis Outline

The present dissertation is structured as follows

Chapter 2 defines a metric to assess the beam independence in a massive MIMO scenario by resorting to the concept of the observable field. Then, the maximum number of independent beams generated by the platform is linked to its electrical size.

Chapter 3 shows that orthogonal beams can be generated regardless of the inter element coupling. It dispels the misconception that high mutual coupling arrays cannot be used for massive MIMO applications, and it paves the

way for ultra wideband massive MIMO and connected arrays for MIMO applications.

Chapter 4 presents the design and the measurements of a connected array for MIMO applications combined with two interchangeable ADL radomes, allowing operations in the bands $6-8\,\mathrm{GHz}$ and $2-8\,\mathrm{GHz}$ when scanning up to $60°$ in the main planes.

Chapter 5 exposes a technique, i.e., the proxy sources method, to simulate efficiently integrated lens antennas. It allows us to decouple the analysis of the feed from the analysis of the lens, entities that require different levels of discretization. This approach allows the handling of accurate full wave lens antenna simulations without excessively increasing the number of unknowns.

Chapter 6 discusses the derivation the current spectrum of a dipole of nonzero metal thickness and rectangular cross section embedded in layered media. This is used to characterize printed transmission lines at sub-THz frequency in terms of characteristic impedance, propagation constant, and losses. A transmission line equivalent circuit representing the different spectral components is finally derived.

Chapter 7 extends the findings of Chapter 6 to the study of finite length dipoles radiating in layered media. This constitutes an efficient method for the analysis of integrated dipoles.

I

The Modelling and Design of Wideband Massive MIMO Phased Arrays

Chapter 2

The Number of Independent Beams from a Given Volume Platform

L'arte non è mai finita, solo abbandonata
Art is never finished, only abandoned
–Leonardo da Vinci

2.1. Introduction

The next generation of wireless communication systems [80, 81] will soon require multi-beam antenna system capabilities [20, 31], similar to those employed in satellite-based communication [82–86]. In these systems, the efficient use of the platform volume is a significant challenge, especially for the lower frequency bands. This issue has been recently recognized as significant also by the telecommunication industry [87]. However, it had been anticipated by the scientific community with the original studies on the degrees of freedom of the field [88, 89], or in the related electromagnetic MIMO scientific community [55, 56]. In this contribution, the emphasis is posed on Line-of-Sight (LoS) communication scenarios, where several beams corresponding to different data streams are directed towards the antenna platform (Fig. 2.1). The beams from the users can be plane waves, e.g., for far-field links, or, more generally, spectra of multiple plane waves, e.g., for near-field communication scenarios. For a given link, its data stream corresponds to the desired signal, while the other data streams interfere. Links are assumed to be independent if the Signal to Interference Ratio (SIR) remains above a predefined threshold. It is known that the mutual cou-

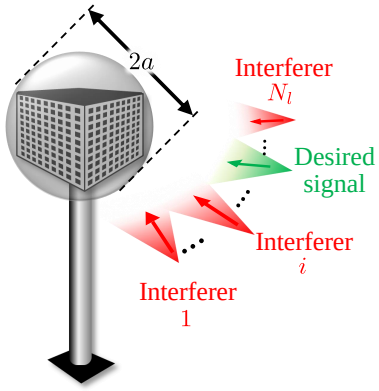

Figure 2.1: Depiction of a multi-beam LoS scenario with N_l simultaneous links, each associated with an incident beam.

pling between the beams limits the maximum number of independent beams hosted by a platform [90]. Satellite-based multi-beam communications mainly use aperture antennas that are large in terms of wavelength. Thus, the aperture efficiency is the main parameter to consider. Tapering the aperture distribution leads to lower side-lobes at the cost of beam widening and aperture efficiency reduction. However, the aperture efficiency concept, defined for electrically large antennas, cannot be applied for antennas whose size is comparable with the wavelength. Accordingly, to date, an appropriate metric to state how many independent links can be established on a platform of moderate size does not exist. To define such a metric, one needs to know how much power an antenna with a given radiation pattern can receive. For this purpose, this chapter exploits the concept of the observable field [91] to represent the portion of the incident field that can be received. This allows the introduction of a novel coupling coefficient, which correlates the observable field and the pattern under investigation. The square magnitude of this coefficient represents the fraction of the maximum power the antenna bounded by a given volume can receive. If one or more interferers are present, one can express the Signal to Interference Ratio (SIR) by using the introduced coupling coefficient. This allows us to study several antenna aperture distributions compatible with the antenna volume, regardless of the specific antenna design. The proposed method constitutes a useful tool to relate the SIR to the antenna dimensions, aperture distribution, and the number of simultaneous independent links.

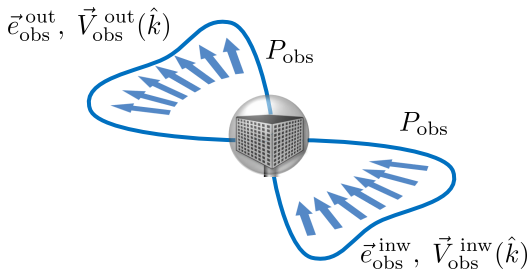

Figure 2.2: A pictorial representation of the inward and outward components of the observable field associated with the sphere of radius a enclosing the base station platform.

2.2. The Observable Field Pattern

For antennas whose dimensions are comparable with the wavelength, we resort to the concept of the observable field [91, 92] and its associated observable power $P_{\rm obs}$, which is the maximum power that can be received by an antenna enclosed in a given spherical volume of radius a. The observable field, depicted in Fig. 2.2, can be expressed as the superposition of an inward and an outward propagating waves

$$\vec{e}_{\rm obs}\left(\vec{r}\right) = \vec{e}_{\rm obs}^{\,\rm inw}\left(\vec{r}\right) + \vec{e}_{\rm obs}^{\,\rm out}\left(\vec{r}\right) \tag{2.1}$$

where $\vec{r} = (r, \theta, \phi)$ is a point in the far-field region of the antenna domain. Both terms are characterized by an angular pattern $\vec{V}_{\rm obs}^{\,\rm inw/out}$ and a spherical spreading

$$\vec{e}_{\rm obs}^{\,\rm inw/out}\left(\vec{r}\right) = \vec{V}_{\rm obs}^{\,\rm inw/out}(\hat{k})\frac{e^{\pm jkr}}{r} \tag{2.2}$$

where the separation of the spatial variables r, θ, ϕ is used, and $\hat{k}$ is defined as $\hat{k} = \sin\theta\cos\phi\hat{x} + \sin\theta\sin\phi\hat{y} + \cos\theta\hat{z}$. The "classic" procedure to define the observable field resorts to a spherical mode (SM) expansion of the incident field [93, 94] and retains only the first $N_{\rm sp} < ka$ modes, where k is the free-space wavenumber. An alternative representation is based on the Physical Optics (PO) currents and was proposed in [91, 92]. It resorts to a spatial windowing to select the equivalent currents distributed on the surface enclosing the finite domain under analysis: these currents radiate the outward component of the observable field.

Fig. 2.3 shows the observable far-field patterns evaluated using both the PO and the SM procedures for $a = 0.02\lambda_0$ and for $a = 7\lambda_0$. The PO and SM curves coincide for the smaller radius case [see Fig. 2.3(a)], while they are very similar up to the fourth side lobe for the larger antenna case [see Fig. 2.3(b)]. However, for antenna dimensions comparable with the wavelength, the two procedures give origin to significantly different patterns. In Fig. 2.4, the observable field patterns are reported for

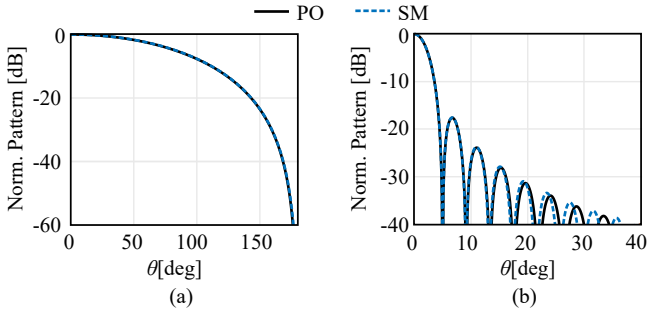

Figure 2.3: Observable field patterns for spherical antenna domains of radius (a) $a = 0.02\lambda_0$ and (b) $a = 7\lambda_0$.

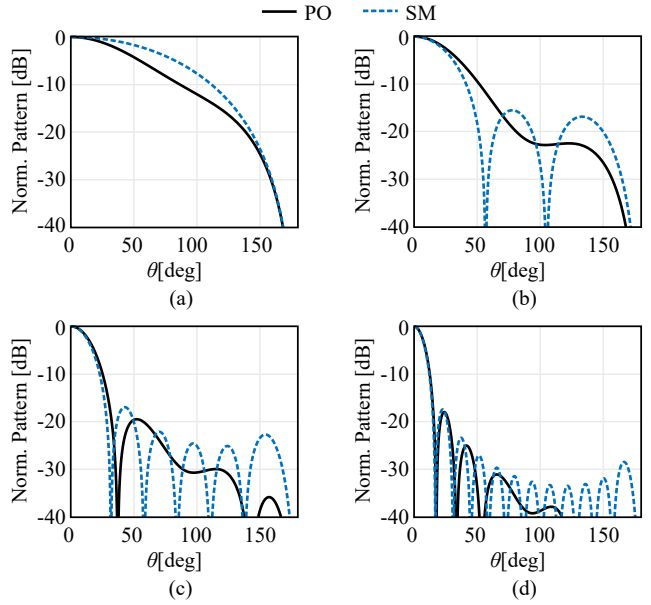

Figure 2.4: Observable field patterns for small to moderate spherical antenna domains of radius (a) $a = 0.3\lambda_0$, (b) $a = 0.5\lambda_0$, (c) $a = \lambda_0$, and (d) $a = 2\lambda_0$.

different radii a. It is apparent that, for these intermediate platform sizes, the SM observable field patterns are characterized by a larger number of nulls (equal to the number of modes N_{sp}) than the PO patterns. Moreover, the SM pattern changes in a quantized manner, related to the discrete number of retained modes N_{sp}. On the

contrary, the PO observable field has patterns that change in a continuous way with respect to size.

2.3. Received Signals in Terms of the Observable Field

In this section, we use the observable field to evaluate the beam coupling for a receiving antenna, introducing new coefficients.

2.3.1. Introduction of the Reception Coupling Coefficients

Let us consider the receiving platform enclosed by the minimum spherical volume of radius a, as shown in Fig. 2.1. Assume that N_l sources are located in different positions, and they are all in the far-field with respect to the antenna platform, which results in N_l plane waves reaching the receiving antenna. Following the procedure in [91, 92] or using the spherical modes expansion [94], the observable field can be calculated for the i-th wave impinging from the direction $\hat{k}_i$. Correspondingly, the associated power can be indicated as P^i_{obs}. The capability of a specific antenna, contained in a spherical volume of radius a and pointing to the $\hat{k}_j$ direction, to receive the wave impinging from the direction $\hat{k}_i$ can be expressed by defining a reception coupling coefficient $C^{ij}_{\text{obs,a}}$ as follows

$$P^{ij}_{\text{r}} = P^i_{\text{obs}} |C^{ij}_{\text{obs}}|^2 \tag{2.3}$$

where $C^{ij}_{\text{obs,a}}$ is the coupling coefficient between the observable field of the incident beams $\vec{V}^{\text{inw}}_{\text{obs},i}(\hat{k})$ and the pattern of the receiving antenna $\vec{V}^{\text{inw}}_{\text{a},j}(\hat{k})$. To calculate $C^{ij}_{\text{obs,a}}$, one can first express the received power for the j-th antenna under conjugate matching conditions, following the procedure reported in Appendix A.1, as

$$P^{ij}_{\text{r}} = \frac{|V^{ij}_{oc} I^j_{\text{a}}|^2}{16 P^j_{\text{a}}} \tag{2.4}$$

where V^{ij}_{oc} is the open-circuit voltage at the input terminals of the receiving j-th antenna when the i-th wave is impinging, and P^j_{a} is the power radiated by the j-th antenna when operated in transmission, fed by the input current I^j_a. The product $V^{ij}_{oc} I^j_{\text{a}}$ can be interpreted as the reaction between the observable field associated with the direction i and the source feeding the j-th antenna, as described in Appendix A.2, where we made use of Lorentz's reciprocity theorem [95–98]. Comparing (2.3) with

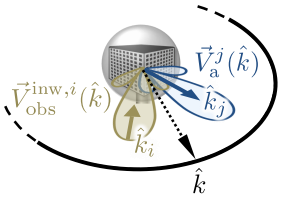

Figure 2.5: Depiction of the antenna and observable field patterns used for the calculations of the $\hat{k}$-integrals in (2.6) and (9).

(2.4), we can define the coupling coefficient as follows

$$C_{\rm obs,a}^{ij} = \frac{V_{oc}^{ij} I_{\rm a}^{j}}{4\sqrt{P_{\rm a}^{j} P_{\rm obs}^{i}}} \tag{2.5}$$

In particular, (2.5) can be evaluated by exploiting the reciprocity theorem. As shown in Appendix A.2, when the i-th interfering source and the antenna are at far-field distance, we have

$$V_{oc}^{ij} I_{\rm a}^{j} = \frac{2}{\zeta} \iint_{4\pi} \vec{V}_{\rm obs}^{\,{\rm inw},i}(\hat{k}) \cdot \vec{V}_{\rm a}^{\,j}(\hat{k}) d\Omega \tag{2.6}$$

where ζ is the free space impedance and $\vec{V}_{\rm a}^{\,j}$ is the angular pattern of the electric field $\vec{e}_{\rm a}^{\,j}(\vec{r})$ radiated by the receiving antenna, when operated in transmission and fed in such a way as to generate the j-th beam, i.e.,

$$\vec{e}_{\rm a}^{\,j}(\vec{r}) = \vec{V}_{\rm a}^{\,j}(\hat{k}) \frac{e^{-jkr}}{r} \tag{2.7}$$

The notation used for the integrals, for a generic function f, is explicitly related to the angular variables by

$$\iint_{4\pi} f(\hat{k}) d\Omega = \int_0^{2\pi} \int_0^{\pi} f(\theta, \phi) \sin\theta d\theta d\phi \,. \tag{2.8}$$

The terms appearing in (2.6) are described in Fig. 2.5, which shows the outward antenna pattern pointing toward $\hat{k}_j$, the inward observable field pattern from the direction $\hat{k}_i$, and the integration variable $\hat{k}$ spanning the entire solid angle for the calculation of the coupling integral. Considering that the observable power and the power radiated by the receiving antenna can be expressed as follows

$$P_{\rm obs}^{i} = \frac{1}{2\zeta} \iint_{4\pi} |\vec{V}_{\rm obs}^{\,{\rm inw},i}(\hat{k})|^2 d\Omega \tag{2.9}$$

$$P_{\mathrm{a}}^{j} = \frac{1}{2\zeta} \iint_{4\pi} |\vec{V}_{\mathrm{a}}^{j}(\hat{k})|^2 d\Omega \tag{2.10}$$

substituting (2.6), (2.9), and (2.10) in (2.5) leads to

$$C_{\mathrm{obs,a}}^{ij} = \frac{\iint_{4\pi} \vec{V}_{\mathrm{obs}}^{\mathrm{inw},i}(\hat{k}) \cdot \vec{V}_{\mathrm{a}}^{j}(\hat{k}) d\Omega}{\sqrt{\iint_{4\pi} |\vec{V}_{\mathrm{obs}}^{\mathrm{inw},i}(\hat{k})|^2 d\Omega \iint_{4\pi} |\vec{V}_{\mathrm{a}}^{j}(\hat{k})|^2 d\Omega}}. \tag{2.11}$$

The above-mentioned coefficients represent the counterpart of Stein's coefficients [90], which are defined for two beams of the same transmitting antenna. It is worth mentioning that the definition of the coupling coefficients in (2.11) is independent of the specific method used to evaluate the observable field and that $|C_{\mathrm{obs,a}}^{ij}| \leq 1$. In the case of $i = j$, the coefficient $C_{\mathrm{obs,a}}^{jj}$ is the coupling with the desired beam. The upper limit $|C_{\mathrm{obs,a}}^{ij}| = 1$ is achieved when the outward pattern of the receiving antenna is chosen to be equal to the inward pattern of the observable field, i.e., $\vec{V}_{\mathrm{a}}^{j}(\hat{k}) = V_{\mathrm{obs}}^{\mathrm{inw},j}(\hat{k})$. Under this condition, the received power is maximized.

2.3.2. Evaluation of the Desired Received Signals

In a multi-link communication scenario, one can assume that the incident field is the superposition of N_l links, where one is desired and the remaining $N_l - 1$ are the interferers. Each link is characterized by a unit vector direction $\hat{e}_i$ for the electric field, an amplitude E_i, and a direction of propagation $\hat{k}_i$. We can assume that the waves incident from different directions are uncorrelated, and they have the same amplitude, i.e., $E_i = E_0, \forall i$. Accordingly, the expected total power received at the j-th antenna can be expressed as follows

$$P_{\mathrm{r}}^{j} = \sum_{i=1}^{N_l} P_{\mathrm{obs}}^{i} |C_{\mathrm{obs,a}}^{ij}|^2 = P_{\mathrm{obs}}^{\mathrm{pw}} \sum_{i=1}^{N_l} |C_{\mathrm{obs,a}}^{ij}|^2 \tag{2.12}$$

It is worth noting that $P_{\mathrm{obs}}^{i} = P_{\mathrm{obs}}^{\mathrm{pw}} \, \forall \, i$ since we have considered the same excitation for all the directions, and since the observable Power does not depend on the direction $\hat{k}_i$. By resorting to the coupling coefficients, the expected power of the desired signal can be expressed as follows

$$S_j = P_{\mathrm{obs}}^{\mathrm{pw}} |C_{\mathrm{obs,a}}^{jj}|^2 \tag{2.13}$$

Using a tapered illumination makes it possible to reduce the interference by lowering the Side Lobe Level (SLL). However, given the antenna dimension, the use of the taper reduces $|C_{\mathrm{obs,a}}^{jj}|$, yielding to a reduction of the received power of the desired signal. While the theory developed until now is valid for generic beams, the examples

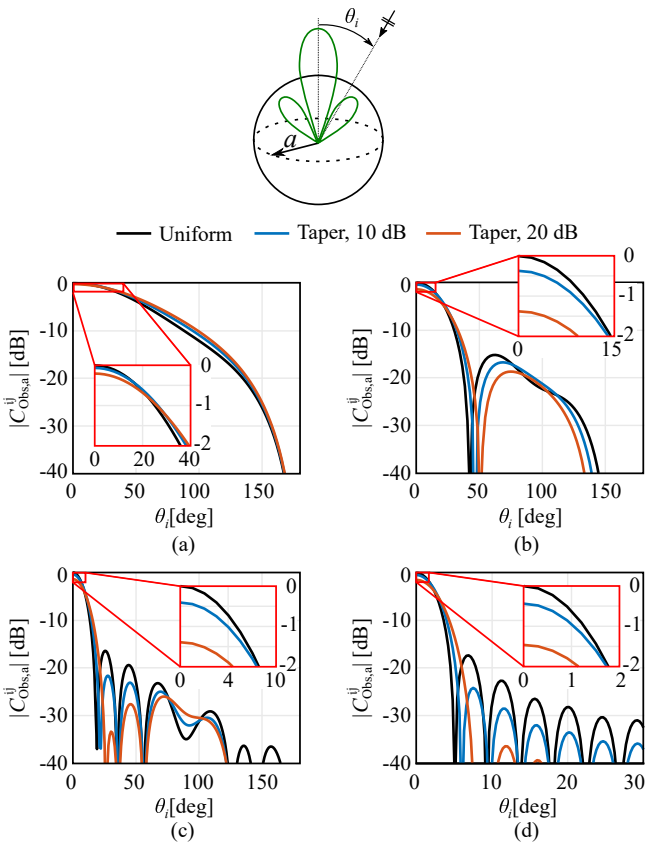

Figure 2.6: Coupling coefficients between the observable field and the antenna pattern $\vec{V}_{\text{a}}$ with different excitations for radii (a) $a = 0.5\lambda_0$ (b) $a = \lambda_0$, (c) $a = 2\lambda_0$, and (d) $a = 7\lambda_0$.

in this contribution are specialized to the case in which the incident beams are plane waves. In the example addressed in Fig. 2.6, the values of $|C^{ij}_{\text{obs,a}}|$ are calculated for a family of antenna patterns $\vec{V}^j_{\text{a}}(\hat{k})$, whose radiation is centered at broadside. The coefficients $|C^{ij}_{\text{obs,a}}|$ are plotted versus θ_i, i.e., the direction of incidence of the i-th signal. The specific antenna patterns $\vec{V}^j_{\text{a}}(\hat{k})$ are derived from $\vec{V}^j_{\text{a}}(\hat{k}) = \vec{V}^{\text{inw},j}_{\text{obs}}(\hat{k})$ or by applying different Gaussian tapers, following the formalism of [99]. For the uniform case, it appears that $|C^{ij}_{\text{obs,a}}(0)| = 1$, as the maximum coupling to the incident plane wave is achieved. The taper has almost negligible effects for small antennas, while, for radii $a > \lambda_0$, the tapering yields a lower coupling from the side lobes and an evident

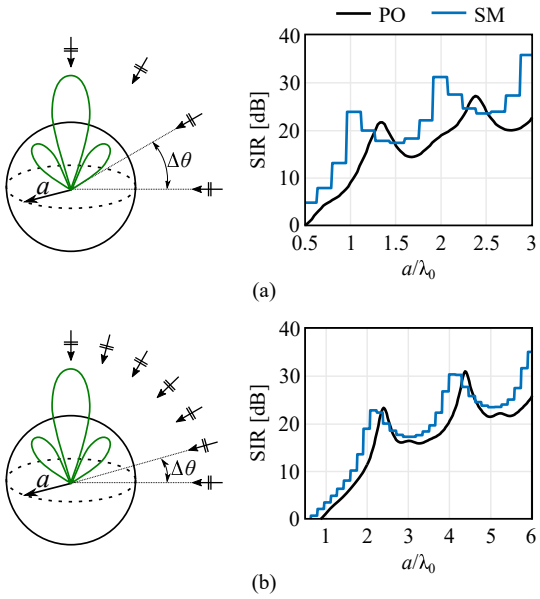

Figure 2.7: SIR versus the radius of the sphere enclosing the antenna for N_l interferers located on the same plane, and spaced by $\Delta\theta$. (a) $\Delta\theta = 30°$, and $N_l = 4$, (b) $\Delta\theta = 15°$, and $N_l = 7$.

reduction of the $|C^{jj}_{\text{obs},a}|$ around $\theta = 0°$. In particular $|C^{ij}_{\text{obs,a}}(0)|^2 \approx 0.92$ and ≈ 0.72, for the 10 dB and the 20 dB taper, respectively.

2.3.3. Evaluation of the SIR

By using the coupling coefficients, the interference at the j-th antenna becomes as follows

$$I_j = P^{\text{pw}}_{\text{obs}} \sum_{\substack{i=1 \\ i\neq j}}^{N_l} |C^{ij}_{\text{obs,a}}|^2 \tag{2.14}$$

and, consequently, the SIR can be expressed as

$$\frac{S_j}{I_j} = \frac{P^{\text{pw}}_{\text{obs}} |C^{jj}_{\text{obs,a}}|^2}{P^{\text{pw}}_{\text{obs}} \sum\limits_{\substack{i=1 \\ i\neq j}}^{N_l} |C^{ij}_{\text{obs,a}}|^2} \tag{2.15}$$

In Fig. 2.7, the SIR for a configuration with N_l users distributed at equispaced fixed directions in the range from 0° to 90° is investigated for $\vec{V}_{\mathrm{a}}^{\,j}(\hat{k}) = \vec{V}_{\mathrm{obs}}^{\mathrm{out},j}(\hat{k})$. The SM and the PO are compared for their prediction of the interference. Between the methodologies, we can note that the PO approach gives lower SIR values. However, both show oscillations around a monotonic increase of the SIR versus the antenna radius. The oscillations indicate that for any given link spacing $\Delta\theta$, specific antenna dimensions can enhance the SIR. The curves show a low SIR for electrically small antenna domains due to the relatively broad beam. When the domain occupied by the antenna becomes larger, the main beam becomes narrower, and the interferers contribute via the antenna side lobes only. Consequently, the SIR increases. It can be noted that the SM method presents a stepped behavior, and its peaks are overestimated if compared with the PO method.

2.4. Properties of the SIR w.r.t. the Minimum Sphere Radius

In this section, a benchmark study is presented in order to estimate the maximum number of independent links supported by a platform of finite dimensions. Since the PO produces systematically more conservative and not quantized SIR values, in the following, we will maintain our attention on the PO only. As before, we assume that the main beam is aligned with the desired signal, while the interferers are located at fixed directions or allowed to be randomly moved within an angular sector. Specifically, the scenario we are considering consists of several users spread around the base station on a 360° field of view (FoV), where the receiving antenna is located. Polarization matching is considered for the interference to analyze the worst case.

2.4.1. Benchmark with the PO Currents

The case $\vec{V}_{\mathrm{a}}^{\,j}(\hat{k}) = \vec{V}_{\mathrm{obs}}^{\mathrm{out},j}(\hat{k})$ is referred to as the "benchmark". Fig. 2.8(a) shows the SIR for fixed interferers uniformly separated by $\Delta\theta$. For larger number of interferers, resulting from smaller $\Delta\theta = 30°, 15°, 7.5°$, the SIR curves shift and stretch to the right. It can be noted that the first peak always corresponds to $a \approx 35\lambda_0/\Delta\theta$, and its value is $\approx$ 18 dB. For such a dimension a the main beam of this benchmark uniform case has its first null at $\theta_{\mathrm{null}} \approx \Delta\theta$. Thus, the first peak occurs when the interferer closest to the signal direction is aligned with the first null of the pattern [see Fig. 2.8(b)].

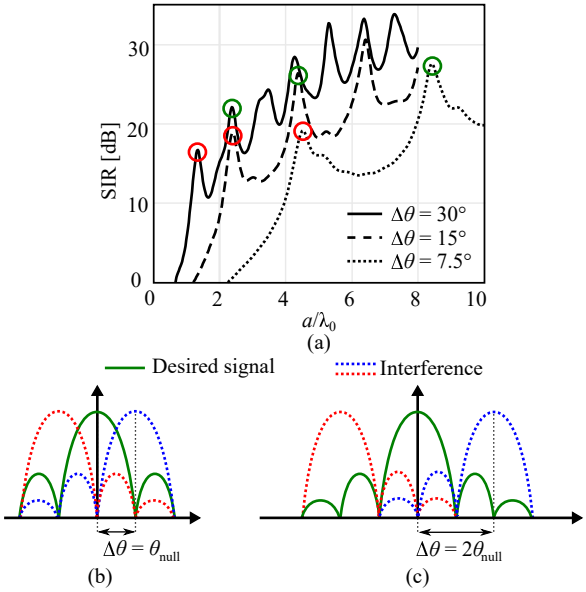

Figure 2.8: (a) SIR in case of uniform aperture distributions, benchmark, for users uniformly distributed on the FoV, where $\Delta\theta$ is the separation angle between the users. The first and second peaks of each curve are highlighted in red and green, respectively. Beams and interferers: (b) first interferer on the first null and (c) first interferer at $2\theta_{\text{null}}$.

From the curves in Fig. 2.8(a), one can easily determine a bandwidth around the peak over which the SIR remains higher than a threshold level. For instance, if the purpose is to serve 24 equispaced users on a 360° FoV with SIR>15 dB, for $\Delta\theta = 15°$ in Fig. 2.8(a), one can select an antenna domain of radius $a = 2.3\lambda_0$, implement a uniform current distribution, and expect that the desired SIR is guaranteed over about 13% bandwidth. An equivalent bandwidth can also be found for the other values of $\Delta\theta$. It may be useful to extend this simple reasoning to all $\Delta\theta$ and assume that the minimum threshold to consider independent links to be SIR>14 dB. A simple rule for the number of equispaced users in a field of view expressed in degrees can then be derived for the benchmark distribution

$$N_{14\text{dB}}^{\text{equi}} = \text{FoV}\frac{a}{35\lambda_0}. \tag{2.16}$$

The second peak of the curves of Fig. 2.8(a) corresponds to the configuration of the non-overlapping beams shown in Fig. 2.8(c), where the first interferer is aligned with the second null of the antenna pattern.

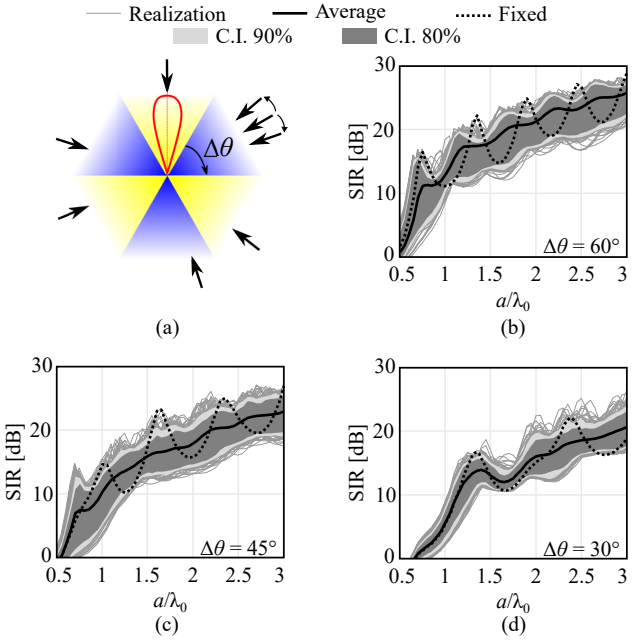

Figure 2.9: (a) Communication scenario with moving interferers and main beam aligned with the desired signal, and its corresponding SIR obtained with the benchmark illumination for (b) $\Delta\theta = 60°$, (c) $\Delta\theta = 45°$, and (d) $\Delta\theta = 30°$ spacing.

In the following, we consider that each interferer is randomly located in an angular sector $\Delta\theta$ wide, as sketched in Fig. 2.9(a). Since each interferer is randomly located in a sector, a Monte Carlo analysis has been performed, considering the interferer uniformly distributed in $\Delta\theta$. Fig. 2.9(b) shows the SIR corresponding to 250 realizations for $\Delta\theta = 60°$, and assuming the benchmark distribution. In the plot are also reported the average SIR, the SIR in case of fixed and equispaced positions of the users, and the 80% (dark grey area) and the 90% (light grey area) confidence intervals. Looking at the confidence intervals in Fig. 2.9, we can notice that they interpolate the maxima and minima of the oscillating fixed-user SIR. Fig. 2.9(c) and (d) present the same analysis for $\Delta\theta = 45°$ and $\Delta\theta = 30°$, respectively. In the last two cases, since the interferers are angularly closer, the SIR is about 3 dB and 6 dB lower, respectively, compared with $\Delta\theta = 60°$. The confidence interval is also narrower since the interferers are distributed randomly within a smaller pertinent sector.

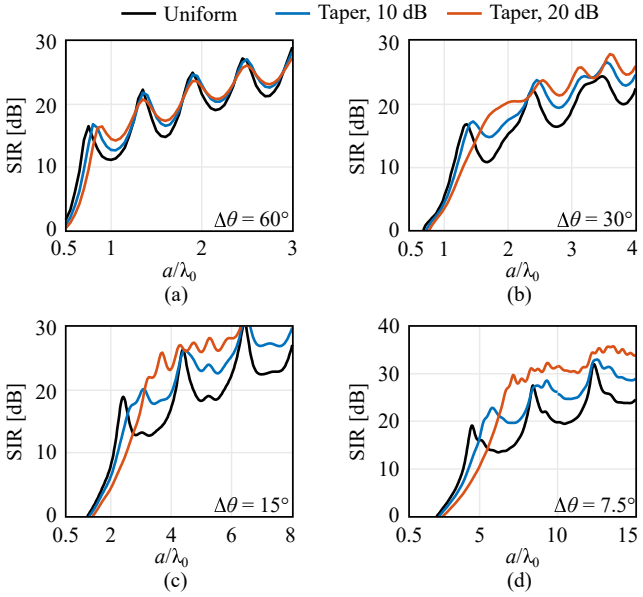

Figure 2.10: SIR comparison between a uniform distribution, a 10 dB Gaussian taper, and a 20 dB Gaussian taper for equispaced beams with (a) $\Delta\theta = 60°$, (b) $\Delta\theta = 30°$, (c) $\Delta\theta = 15°$, and (d) $\Delta\theta = 7.5°$.

2.4.2. Analysis of the Aperture Distribution Taper

Once the benchmark for the SIR has been assessed, one can investigate the potential increases of SIR deriving from the use of a tapered aperture distribution, which for large antenna volumes compromises the main beam efficiency for lower side lobes. Fig. 2.10 shows the SIR for the equispaced fixed users in the case of four different values of $\Delta\theta$: 60°, 30°, 15°, and 7.5°, which correspond to N_l: 6, 12, 24, and 48. In all cases, the taper leads to wider main lobes and to a $|C_{\text{obs,a}}| < 1$. For larger radii, the patterns of the tapered distribution are characterized by lower sidelobes, which result in smaller oscillations of the SIR, compared to the uniform distribution. On the contrary, for small domains, specifically for $a < 35\lambda_0/\Delta\theta$, the taper reduces the SIR.

Fig. 2.11 shows the SIR in the case of randomly distributed interferers for several angular sectors $\Delta\theta$ and different aperture distribution tapers. Compared with the benchmark uniform distribution case, the confidence intervals associated with tapered distributions become significantly narrower for large radii of the minimum sphere enclosing the antenna (see Fig. 2.9). For smaller radii instead, the confidence intervals become broader than in the absence of tapering. That is because the main beam of the

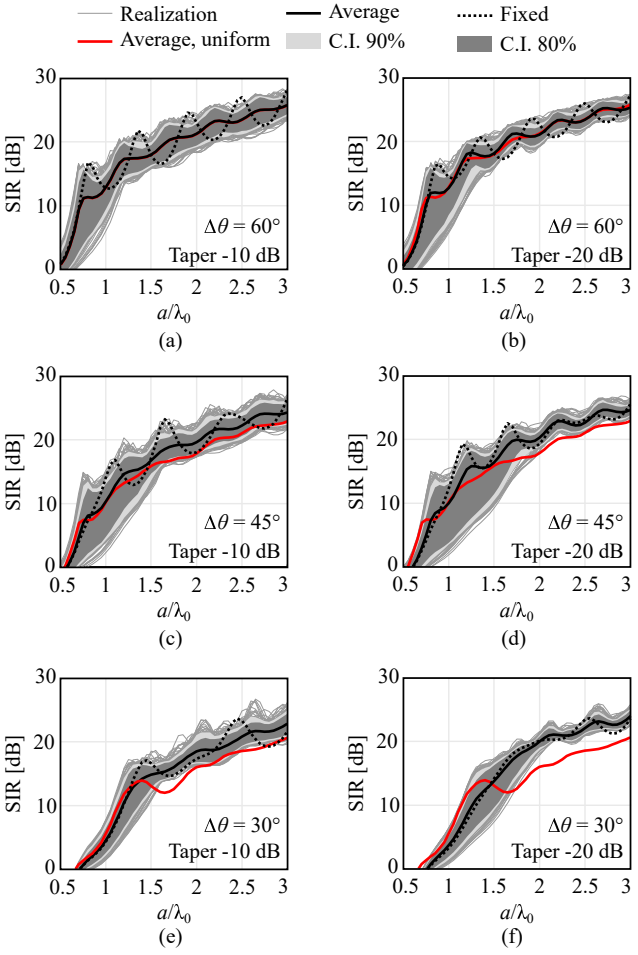

Figure 2.11: SIR with the main beams oriented toward the desired user under the conditions of (a) 10 dB and (b) 20 dB Gaussian taper, both for $\Delta\theta = 60°$, (c) 10 dB and (d) 20 dB Gaussian taper, for $\Delta\theta = 45°$, (e) 10 dB and (f) 20 dB Gaussian taper, for $\Delta\theta = 30°$.

antennas becomes wider, and especially for $\Delta\theta = 45°$, the interferers are associated with beams that can arrive from directions relatively close to the main beam.

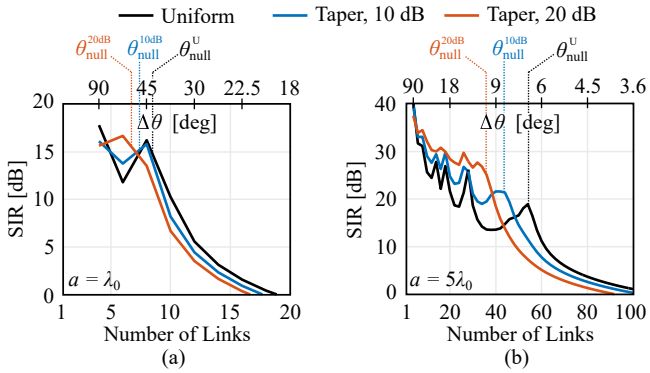

Figure 2.12: SIR versus the number of realized links on the same azimuthal cut with a FoV=360° and fixed interferers, for a radius (a) $a = \lambda_0$ and (b) $a = 5\lambda_0$.

2.5. Number of Links for Fixed Size Platforms

A parameter that can be used to assess the properties of a platform of fixed radius a is the number of links supported with an SIR larger than the desired threshold. Fig. 2.12 shows the SIR versus the number of links, or equivalently the spacing $\Delta\theta$, for platforms of radius $a = \lambda_0$ and $a = 5\lambda_0$. All the interferers lie on the same azimuthal cut and are impinging from deterministic directions, equispaced between $-180°$ and $180°$. As expected, the SIR decreases by increasing the number of links. It is worth noting that the SIR decreases monotonically starting from a certain number of links corresponding to a spacing $\Delta\theta$ equal to the angular position of the first null of the antenna radiation pattern. Beyond this limit, the interferers contribute directly to the main beam of the receiving antenna. For a small number of links, the field generated by the interferers interacts with the side lobes of the receiving antenna mainly, and tapering guarantees higher SIR values.

Fig. 2.13 shows the SIR versus the number of links for the same cases of Fig. 2.12, but for interferers assumed to be impinging from random directions within the predefined sectors. Due to the random positions of the interfering plane waves, a Monte Carlo analysis of the SIR based on 250 realizations has been carried out. The SIR corresponding to the fixed interferers is compared with the average SIR extracted from the statistical analysis and the 90% confidence interval.

From Fig. 2.13(a) and (b), relevant to a one wavelength radius sphere, it is apparent that the differences between the number of beams achievable with the tapered and non-tapered (benchmark) distributions are not significant. However, from Fig. 2.13(c) and (d), where the antenna volume is large (i.e., $a = 5\lambda_0$) it is apparent that for $N_l < 50$ the tapering provides SIR higher than the benchmark (even 5 dB).

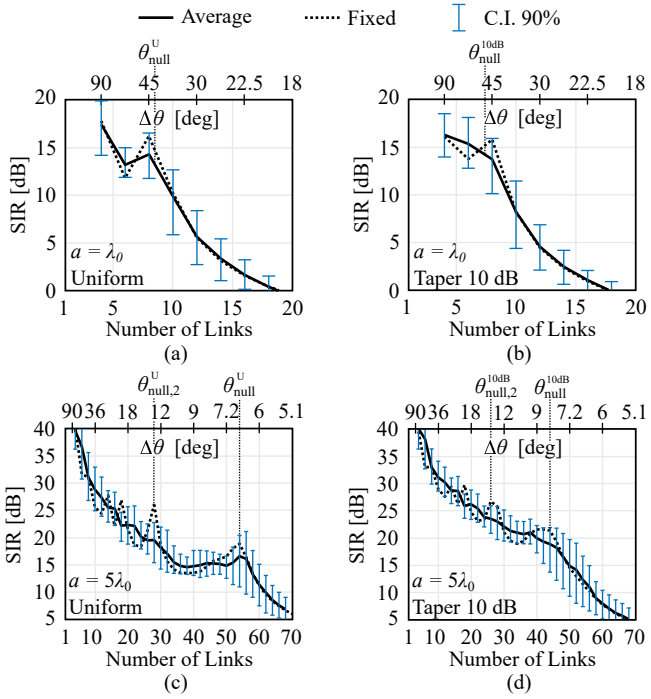

Figure 2.13: SIR versus the number of realized links on the same azimuthal cut with a FoV=360° and moving interferers, for a radius $a = \lambda_0$, and (a) uniform aperture distribution, (b) Gaussian taper of 10 dB, and for a radius $a = 5\lambda_0$ and (c) uniform aperture distribution, (d) Gaussian taper of 10 dB.

The limit is dictated by the position of the first null and can be easily calculated with the approximate formula (2.16).

2.6. Conclusion

An analysis of multi-beam antenna platforms for LoS mobile communications was provided. In particular, a new class of coefficients was introduced. They represent the coupling between the investigated patterns and the one associated with the observable field for the antenna platform of given dimensions. These coefficients can be used to evaluate the signal and the interference between beam-shaped links supported by the platform. Then, for the specific case of plane-wave-like links, a benchmark is established that allows estimating the maximum number of independent links that a

platform can support. This benchmark is taken to be an antenna radiation pattern equal to the inward portion of the observable field. This choice guarantees that the signal from the desired users is maximized. Accordingly, any other solution for the pattern design can be compared to the benchmark to assess its merits. The observable field was calculated using the procedure based on the PO currents to examine the potential advantages of the benchmark. Two cases were investigated. For both, the users were tracked by a dedicated beam. The first case implied links between fixed equispaced interferers, while the second case regarded randomly distributed interferers within predefined angular sectors. The SIRs associated with the Gaussian distributions with 10 and 20 dB edge taper were compared to the benchmark. It resulted that, for fixed equispaced interferers, it is possible to exploit the maximum gain associated with the benchmark cases to achieve the maximum SIR at least over relatively narrow bands (10-15%). However, for randomly distributed interferers, the advantage of the benchmark disappears, even for narrow bandwidths, when the antenna linear dimension is larger than $3\lambda_0$. In these cases, tapered distributions provide higher SIR.

Chapter 3

High Mutual Coupling and Ultrawideband Massive MIMO

In the beginner's mind there are many possibilities, but in the expert's there are few
–Shunryu Suzuki

Wireless communications will heavily rely in the near future on the possibility of transmitting and receiving multiple data streams through directive beams connecting the base station with different users (Fig. 3.1). With the deployment of 5G communications and the planning for the future 6G networks, antennas will focus the radiation in smaller angular sectors with the aim to improve the energy and spectral efficiency, while reducing the interference levels. In such a communication scenario, the base stations will be equipped with phased array antennas serving several distributed users simultaneously by means of multiple and adaptively steered beams. Thus, these multi-beam antennas are regarded as a key technology for enabling massive multiple-input and multiple-output (MIMO) and high speed mobile networks [18, 51, 100].

In the 1960s, [90, 101, 102] discussed the theoretical limitation on the generation of multiple beams from a single radiating aperture. More specifically, Stein in [90] defined the beam coupling factors to quantify the orthogonality between beams. In his derivation, Stein linked the coupling between two beams generated by a radiating aperture to the coupling between the feeding lines (or the beamforming networks) associated with the beams. Later on, these same coupling coefficients were named envelope correlation between antenna patterns and used in MIMO communication scenarios [103–106], as a statistical value indicating the similarity in the voltages received by different antennas in the presence of multipath. In absence of losses, when associating each beam with a feeding structure, the coupling between two antenna

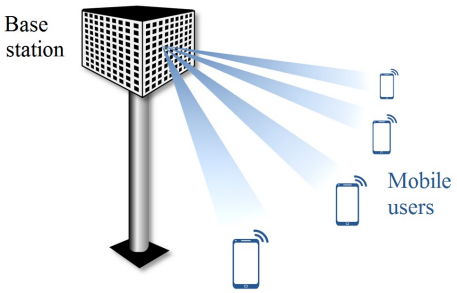

Figure 3.1: Wireless base station simultaneously connecting with several mobile users.

beams can be approximated in terms of the impedance or scattering matrix between the feeds [104].

In MIMO architectures, the mutual coupling between the antennas is typically regarded as a limitation, as it is associated with a reduced system capacity [107–110]. For this reason, several techniques have been employed for the reduction of the mutual coupling [111, 112] or the compensation of its effects [113–115]. However, these works typically refer to configurations in which the beam orthogonality is intended at the level of the radiation patterns from the individual elements of the array. On the contrary, when each beam is collectively generated by all the antennas, the beam coupling is not directly related to the coupling between the individual elements, but to the coupling between the beamforming networks [90]. In these cases, the role of the mutual coupling between the individual elements in the performance of the multibeam systems remains unclear. For example, in [116] it was shown that a nonzero mutual coupling level can maximize the gain in arrays when the elements are simultaneously excited. More recently, MIMO concepts based on high mutual coupling arrays have been proposed in [117].

The main scope of this chapter is to clarify how the inter-element mutual coupling can affect the capability of creating multiple simultaneous beams with a single phased array. To this aim, we evaluate the beam coupling coefficients for arrays of dipoles, comparing two canonical geometries: linear arrays of collinear resonant dipoles, for which the mutual coupling is relatively low, and linear arrays of connected dipoles, characterized by high mutual coupling. Moreover, examples of two dimensional arrays are also presented, namely a narrowband array of patches and a more wideband array of connected slots with dielectric superstrate.

For the investigation, we first express the coupling between two beams in terms of the electric current distributions associated with each beam. The resulting expression

contains a coupling integral between the two currents similar to a mutual impedance, but with a kernel that is a singularity-free Green's function [106]. By expanding the currents in terms of basis functions, the beam coupling can be also written as a weighted sum of coupling contributions between each pair of basis functions. The derived expressions can be applied to the different arrays, to quantify the effect of different levels of mutual coupling on the beam orthogonality. We give a few examples of multibeam arrays for which the coupling between beams can be weakly dependent on the level of mutual coupling between individual elements of the array.

Since the high mutual coupling between the ports is a characterizing feature of all the wideband wide scanning arrays, this finding opens the possibilities to largely increase the bandwidth and scan performance of MIMO arrays. In fact, a wideband capability is an important feature of future wireless communication. When more and more frequency bands will be used for different services, having a single narrowband antenna for each sub-band will become unfeasible for cost and space occupation. For this reason, the use of wideband arrays that can cover simultaneously multiple bands will become increasingly important.

3.1. Beam-Coupling Factor

Let us consider a radiating aperture, as depicted in Fig. 3.2, which radiates N_b beams, with indexes $n \in \{1, \cdots, N_b\}$. Each beam is characterized by an electric field $\vec{e}_n(\vec{r})$, radiated by an associated electric current distribution $\vec{j}_n$, where $\vec{r} \equiv (r, \theta, \phi)$ is a generic point in the far-field with radial distance r, elevation angle θ and azimuthal angle ϕ. The electric field for the n-th beam is given by

$$\vec{e}_n(\vec{r}) = \vec{E}_n(\hat{k}) \frac{e^{-jkr}}{r} \tag{3.1}$$

where k is the free space propagation constant and $\vec{E}_n(\hat{k})$ represents the far field radiation pattern, which is a function of the angular direction $\hat{k} = \sin\theta\cos\phi\hat{x} + \sin\theta\sin\phi\hat{y} + \cos\theta\hat{z}$. The radiation pattern can be related to the electric current distributions by

$$\vec{E}_n(\hat{k}) = -\frac{jk\zeta}{4\pi}\left[\underline{\underline{I}} - \hat{k}\hat{k}\right] \cdot \vec{J}_n(\hat{k})\,. \tag{3.2}$$

In (3.2), $\zeta = 120\pi\,\Omega$ is the free space characteristic impedance, and $\underline{\underline{I}}$ is the identity dyad. The function $\vec{J}_n$ is the spatial Fourier transform of $\vec{j}_n$, given by

$$\vec{J}_n(\hat{k}) = \iint_{S_n} \vec{j}_n(\vec{r}\,')e^{jk\hat{k}\cdot\vec{r}\,'}\, dS' \tag{3.3}$$

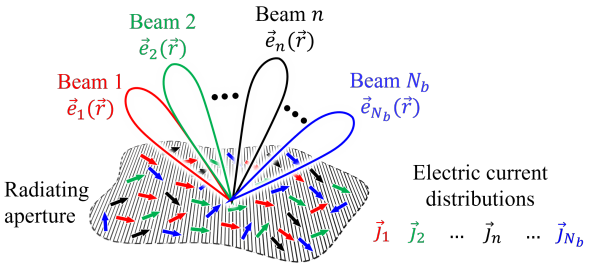

Figure 3.2: Radiating aperture generating N_b beams, characterized by the electric fields $\vec{e}_n$, associated with the electric current distributions $\vec{j}_n$.

where S_n refers to the domain in which the n-th current distribution $\vec{j}_n$ differs from zero.

3.1.1. General Definition of the Beam Coupling

As formalized in [90], the cross coupling between any pair of beams with patterns $\vec{E}_n$ and $\vec{E}_{n'}$ can be expressed as follows

$$c_{nn'} = \frac{\iint_{4\pi} \vec{E}_n^*(\hat{k}) \cdot \vec{E}_{n'}(\hat{k}) d\Omega}{\sqrt{\iint_{4\pi} \left|\vec{E}_n(\hat{k})\right|^2 d\Omega} \sqrt{\iint_{4\pi} \left|\vec{E}_{n'}(\hat{k})\right|^2 d\Omega}} \,. \tag{3.4}$$

The double integral at the numerator of (3.4) represents an inner product between two radiation patterns in the angular domain. The terms at the denominator are normalization factors so that the modulus of the coupling factor satisfies the following condition: $0 \leq |c_{nn'}| \leq 1$.

By substituting (3.2) in (3.4) and following the algebraic steps reported in Appendix B.1, the beam coupling factor can also be expressed in terms of the currents spectral distributions [105]

$$c_{nn'} = \frac{R_{nn'}}{\sqrt{R_{nn}} \sqrt{R_{n'n'}}} \tag{3.5}$$

where

$$R_{nn'} = \frac{k^2 \zeta}{16\pi^2} \iint_{4\pi} \vec{J}_n^*(\hat{k}) \cdot \left[\underline{\underline{I}} - \hat{k}\hat{k}\right] \cdot \vec{J}_{n'}(\hat{k}) d\Omega \,. \tag{3.6}$$

To give an interpretation of the term $R_{nn'}$, it is convenient to express it in the spatial domain by using (3.3), leading to

$$R_{nn'} = -\iint_{S_n}\iint_{S_{n'}} \vec{j}_n^*(\vec{r}) \cdot \underline{\underline{g}}^{\,\mathrm{vis}}(\vec{r}-\vec{r}\,') \cdot \vec{j}_{n'}(\vec{r}\,')dS'\,dS \tag{3.7}$$

where we defined a 'visible' Green's function as

$$\underline{\underline{g}}^{\,\mathrm{vis}}(\vec{r}-\vec{r}\,') = \frac{-k^2\zeta}{16\pi^2}\iint_{4\pi}\left[\underline{\underline{I}} - \hat{k}\hat{k}\right] e^{-jk\hat{k}\cdot(\vec{r}-\vec{r}\,')}d\Omega. \tag{3.8}$$

It is worth noting that the expression (3.7) resembles a mutual impedance between the two current distributions, and defined as follows

$$Z_{nn'} = -\iint_{S_n}\iint_{S_{n'}} \vec{j}_n^*(\vec{r}) \cdot \underline{\underline{g}}\,(\vec{r}-\vec{r}\,') \cdot \vec{j}_{n'}(\vec{r}\,')dS'\,dS\,. \tag{3.9}$$

The function $\underline{\underline{g}}$ is the free-space dyadic Green's function which relates the electric field to the electric current. Comparing (3.9) with (3.7), one can note that, while $\underline{\underline{g}}$ is obtained by integrating the spectral Green's function over the entire spectrum, the visible Green's function $\underline{\underline{g}}^{\,\mathrm{vis}}$ results from an integration only on the visible spectrum as in (3.8). Moreover, the visible Green's function does not exhibit singularities even for co-located sources, since it does not include the term $|\vec{r}-\vec{r}\,'|^{-1}$ of the standard free-space Green's function. This can be observed by realizing that, as proved in B.2, the integral on the visible spectrum in (3.8) can be expressed as follows

$$\underline{\underline{g}}^{\,\mathrm{vis}}(\vec{r}) = -\frac{\zeta}{4\pi}\left[k^2\underline{\underline{I}} + \nabla\nabla\cdot\right]\,\mathrm{sinc}\,(kr)\,. \tag{3.10}$$

The quantity in (3.7) represents a 'visible' mutual impedance that depends only on how the two currents interact with their far-field radiation patterns. It can be demonstrated that, for real-valued current distributions, normalized so that they are equal to one at the port terminals, $R_{nn'}$ coincides with the mutual resistance, i.e., $R_{nn'} = \mathrm{Re}\{Z_{nn'}\}$ [118].

3.1.2. Expansion of Electric Currents with Basis Functions

Often in antenna problems the current distributions are not available beforehand, but they have to be evaluated by means of numerical methods. For instance, one can

expand the n-the current distribution in a sum of basis functions, as typically done in Method of Moments solutions

$$\vec{j}_n(\vec{r}) = \sum_m i_{m,n}\vec{b}_m(\vec{r}) \tag{3.11}$$

where $\vec{b}_m(\vec{r})$ is the m-th sub-domain basis function and $i_{m,n}$ is its corresponding weight. If all the basis functions are equal, (3.11) becomes

$$\vec{j}_n(\vec{r}) = \sum_m i_{m,n}\vec{b}(\vec{r} - \vec{r}_m) \tag{3.12}$$

where $\vec{r}_m$ is the center of the m-th basis function. The Fourier transform of $\vec{j}_n(\vec{r})$ can be written as follows

$$\vec{J}_n(\hat{k}) = \sum_m i_{m,n}\vec{B}(\hat{k})e^{jk\hat{k}\cdot\vec{r}_m} \tag{3.13}$$

where $\vec{B}(\hat{k})$ is the Fourier transform of $\vec{b}(\vec{r})$. By substituting (3.13) in (3.7), one obtains

$$R_{nn'} = \sum_m i^*_{m,n} \sum_{m'} i_{m'n'} R_{mm'}. \tag{3.14}$$

where

$$R_{mm'} = \frac{k^2\zeta}{16\pi^2}\iint_{4\pi}\vec{B}^*(\hat{k})\cdot\left[\underline{\underline{I}} - \hat{k}\hat{k}\right]\cdot\vec{B}(\hat{k})e^{-jk\hat{k}\cdot(\vec{r}_m - \vec{r}_{m'})}d\Omega\,. \tag{3.15}$$

The beam coupling in (3.5) can be then expressed as follows

$$c_{nn'} = \frac{\mathbf{i}_n^{\mathrm{H}}\,\mathbf{R}\,\mathbf{i}_{n'}}{\sqrt{\mathbf{i}_n^{\mathrm{H}}\,\mathbf{R}\,\mathbf{i}_n}\sqrt{\mathbf{i}_{n'}^{\mathrm{H}}\,\mathbf{R}\,\mathbf{i}_{n'}}} \tag{3.16}$$

where $\mathbf{i}_n$ are the weights of n-th current expansion, $\mathbf{R}$ is the matrix whose entries are defined in (3.15) and H indicates the Hermitian transpose. As already pointed out earlier, for real-valued basis functions, the matrix $\mathbf{R}$ is equal to real part of the method of moments impedance matrix. However, $c_{nn'}$ has still complex value, since it depends on the complex amplitudes of the basis functions associated with the two beams, $\mathbf{i}_n$ and $\mathbf{i}_{n'}$.

3.2. Application to Dipole Arrays

To quantify how the mutual coupling in antenna arrays affects the beam orthogonality, we evaluate the expressions given in the previous section for arrays of dipoles. For

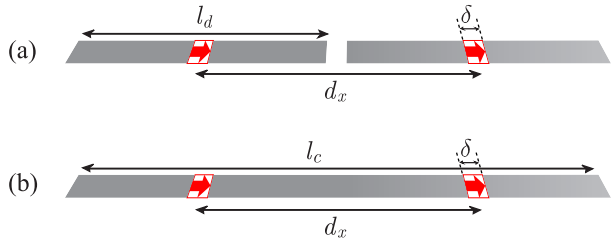

Figure 3.3: Geometry for: (a) two center-fed collinear dipoles, with length l_d, distance between centers d_x, delta-gap size δ and (b) two connected dipoles, with total length l_c and distance between feeds d_x.

the sake of simplicity, we first analyze and compare two simple geometries: an array of two collinear dipoles [see Fig. 3.3(a)], and an array of two connected dipoles [see Fig. 3.3(b)]. This choice is motivated from the fact that two aligned dipoles are typically poorly coupled because of a radiation null along their axis. On the contrary, connected dipoles are characterized by high mutual coupling, since the current can flow from one element to the other through the electrical connection.

A method of moments analysis, similar to the one described in [119] has been implemented to apply the expression of the beam coupling from (3.16). The geometrical parameters are chosen as $d_x = 0.45\lambda$, $w = \delta = 0.1\lambda$, $l_d = 0.4\lambda$ and $l_c = 0.85\lambda$, where λ is the wavelength at 10 GHz.

3.2.1. Comparison Between Two-Element Arrays of Resonant and Connected Dipoles

The reflection coefficient and the mutual coupling between the two elements of the array is shown in Fig. 3.4, for both the resonant and the connected dipoles. The S-parameters are normalized to a load impedance of 70 Ω for the resonant dipole and 150 Ω for the connected one. It can be observed that, for the separated dipoles in Fig. 3.4(a), the $|S_{12}|$ peaks at around 10 GHz with a value of −12 dB. Moreover, the conventional dipoles exhibit a narrow bandwidth due to the typical resonant nature of the radiating element. On the contrary, higher levels of mutual coupling occur for the connected dipoles in Fig. 3.4(b), higher than −8 dB over the large bandwidth of investigation. It is well known that, by electrically connecting the dipoles, the S-parameters become more frequency independent, achieving wideband impedance matching [41].

The beam coupling coefficient c_{12} is also evaluated as a function of frequency in Fig. 3.5. In this section, we assume that the two beams are obtained with one of the two elements active and the other terminated on a resistive load. The frequency

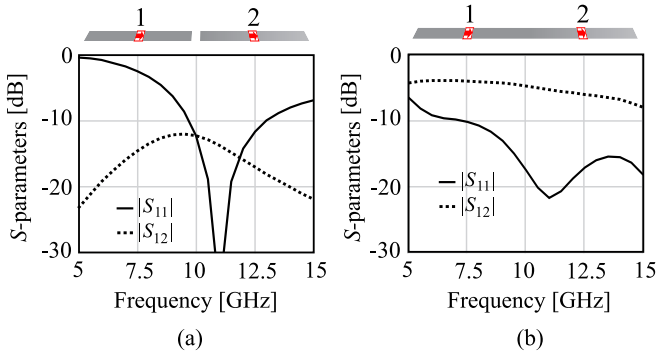

Figure 3.4: S_{11} and S_{12} for 2-element arrays of (a) resonant dipoles and (b) connected dipoles.

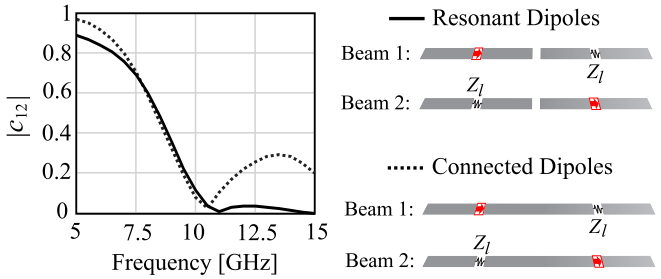

Figure 3.5: c_{12} for 2-element array of resonant and connected dipoles. The beam coupling is intended between beams obtained with one of the two elements in the array active and the other passively terminated and vice versa.

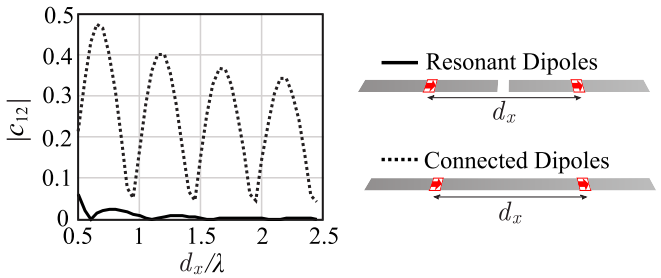

Figure 3.6: c_{12}, calculated at 10 GHz, versus the inter-element distance for 2-element array of resonant and connected dipoles; λ is the wavelength at 10 GHz.

dependence of the beam coupling is similar for the two structures, but the connected array exhibits higher values of c_{12}, due to the higher mutual coupling.

From Fig. 3.5, the values of c_{12} are shown to be close to zero for both cases at around 11 GHz, which corresponds to a distance between feeds of around half wavelength. To better highlight this aspect, we report in Fig. 3.6 the beam coupling for a fixed frequency (10 GHz), but varying the distance of the two elements, for both resonant and connected dipoles. The curves oscillate as a function of the frequency creating a interference pattern that depends on the electrical distance between elements. Much higher levels are obtained for the connected dipole elements, because of the high mutual coupling.

Therefore, in the configuration in which the two elements are to be used independently, i.e.when one beam is associated with one feeding gap, high inter-element mutual coupling yields high beam coupling. Indeed, in this case c_{12} is closely related to the mutual impedance, and thus directly proportional to the levels of mutual coupling. In this configuration, although connected arrays are intended to be used over a wide frequency range, low levels of c_{12} can be achieved only over a narrow frequency band.

3.2.2. Linear Arrays Generating Multiple Directive Beams

Another investigated case is when the array comprises N elements and the beams are generated through the coherent excitation of the entire array. For this study, we assume that such an array generates two beams, one fixed pointing at broadside (beam 1) and the other pointing at a varying angular direction $\Delta\theta$ (beam 2). Thus, the array is fed simultaneously with two voltage distributions $\mathbf{v}_1$ and $\mathbf{v}_2$, given by

$$v_{1,n} = 1 \qquad \text{for } n \in \{1, \ldots, N\} \tag{3.17}$$

$$v_{2,n} = e^{-jknd_x \sin(\Delta\theta)} \qquad \text{for } n \in \{1, \ldots, N\} \tag{3.18}$$

assuming that the elements are located on the x-axis in the reference system. The coupling between the two beams is shown in Fig. 3.8, for both resonant and connected dipoles, as a function of the separation between the beams $\Delta\theta$ and for different number of elements. The geometrical parameters are $d_x = 0.45\lambda$, $l_d = 0.4\lambda$, where λ is the wavelength at the calculation frequency.

The coupling is equal to one for the total overlap between beams ($\Delta\theta = 0°$) and decreases for larger separation of the pointing angles. The oscillations are due to the interference between the sidelobes of the two patterns. The zeros of the coupling occur when the maximum of the main lobe of one beam is aligned with a null of the other. This corresponds to $\Delta\theta$ equal to one half of the first null beamwidth. For the smaller array cases, the beam overlap remains higher for a wider range of $\Delta\theta$, due to the wider beamwidth.

It can be noted from Fig. 3.8 that the coupling curves for the resonant and connected dipoles are very similar, despite the different mutual-coupling levels.

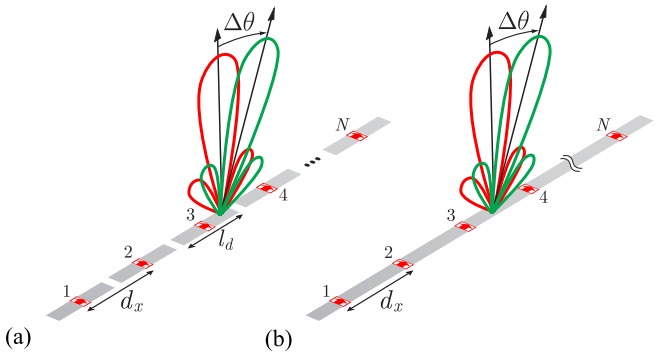

Figure 3.7: N-element linear array of resonant and connected dipoles. The array generates two beams, pointing at broadside and $\Delta\theta$, respectively.

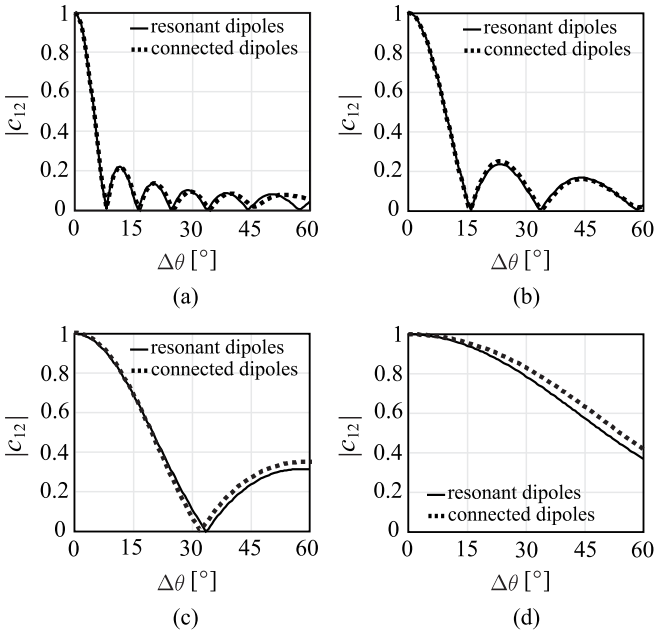

Figure 3.8: Beam coupling between two beams, pointing at broadside and $\Delta\theta$, respectively, for linear array of resonant and connected dipoles with (a) $N = 16$, (b) $N = 8$, (c) $N = 4$ and (d) $N = 2$.

To reduce the beam coupling after the first null, the side lobes of the pattern can be reduced with a tapered illumination of the array. The coupling in Fig. 3.9 refers to arrays of 16 elements with a Gaussian amplitude distribution with edge taper of -10 dB. The coupling remains very low for the low-coupled dipoles for $\Delta\theta > 20°$.

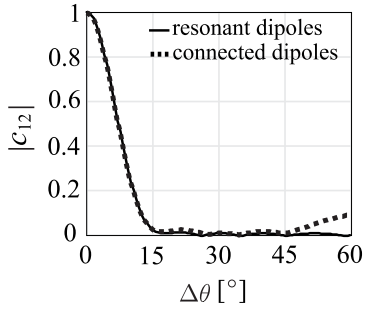

Figure 3.9: Beam coupling between two beams, pointing at broadside and $\Delta\theta$, respectively, for linear array of resonant and connected dipoles with $N = 16$ and Gaussian tapered illumination with edge taper of -10 dB.

On the contrary, the connected array exhibits a similar coupling up to $\Delta\theta > 50°$, but increased values for larger scanning of the beam. The scanning above 50° yields some mismatch and aberrations in the patterns, which causes the raise in coupling, as shown in Fig. 3.9. In fact the impedance of the array is not anymore well matched for large scanning, and the impedance varies for each element of the array due to finite edge effects in connected dipoles [120].

3.3. Examples of Planar Arrays

In this section, we analyze two-dimensional planar arrays, simulated using a full-wave electromagnetic solver. Two different cases are compared: an array of patches and an array of connected slots, both consisting of 8×8 elements. The two arrays have the same unit cell size, defined by $d_x = d_y = 0.5\lambda_0$, where λ_0 is the wavelength at 10 GHz. The unit cells are shown in Fig. 3.10. The patch element in Fig. 3.10(a), $l_p = 8.8$ mm long and $w_p = 7.9$ mm wide, is backed by a metal cavity filled with a dielectric of relative permittivity $\varepsilon_r = 2.33$ and thickness $t_p = 2$ mm. The vertical metal walls of the cavity have been added to prevent the propagation of surface waves. The patch is fed by a vertical pin with diameter of 1.1 mm and the coaxial feed is normalized to a line of 42.5 Ω. The connected slot unit cell is depicted in Fig. 3.10(b) and is characterized by slot width $w_s = 0.2\lambda_0$, fed by a δ-gap generator with size $\delta_s = 0.25\lambda_0$, and backed by a ground plane at a distance $h_d = \lambda_0/4$. Vertical walls have been placed between the ground plane and the array on the E-plane to improve the scanning performance. Moreover the array is loaded with a wide angle impedance matching layer (WAIM), that is a thin dielectric layer of relative permittivity $\varepsilon_r = 5$, $h_{diel} = 1$ mm, and placed at a distance $h_{\text{gap}} = 2.5$ mm from the array. The port impedance is normalized to 150 Ω.

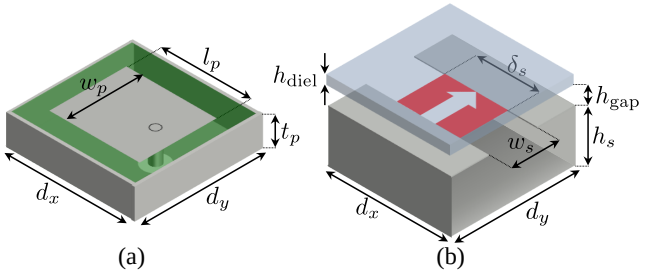

Figure 3.10: Unit cell of (a) patch array and (b) connected slot array, with characteristic geometrical parameters.

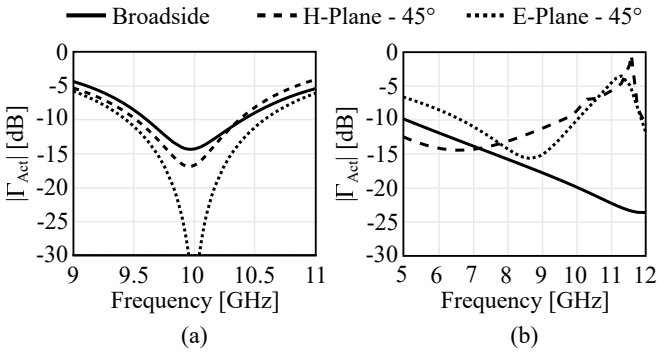

Figure 3.11: Active reflection coefficient of the infinite array of (a) patches, and (b) connected slots for broadside and scanning up to 45° on the main planes.

As shown in Fig. 3.11, the two unit cells are matched when scanning up to 45° on the main planes, but while the array of patches can operate on the band 9.5−10.5 GHz, the connected array is matched over a larger bandwidth, between 7 and 10 GHz. Array simulations for 8×8 arrays for both cases (see Fig. 3.12) have been performed with CST. The mutual coupling levels for the two arrays are shown in Fig. 3.13, between element ports in the center of the array, according to the indexing specified in Fig. 3.12. It can be observed that a higher level of mutual coupling is obtained for the connected slots, which is desired to provide a large operational bandwidth.

The beam coupling between a beam pointing to broadside and a beam pointing to $\Delta\theta$ is presented for the two arrays in Fig. 3.14 as a function of $\Delta\theta$, at 10 GHz for both arrays and at 7 GHz for the connected slots only. It is evident that the beam orthogonality remains comparable, despite the different levels of inter-element mutual coupling, as these are mainly dependent on the beamwidth and the sidelobe level of the radiation patterns.

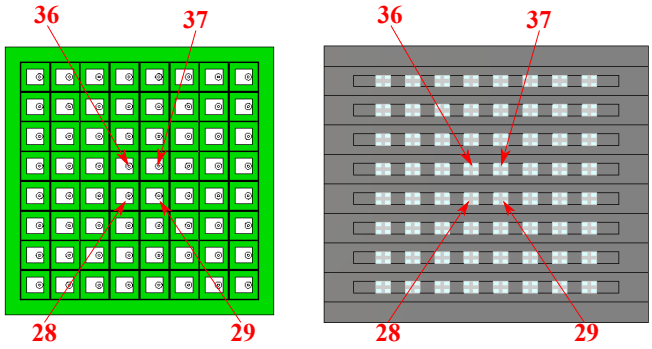

Figure 3.12: Top view of the (a) patch, and (b) connected slot array. The positions of the central elements 28, 29, 36, and 37 is highlighted.

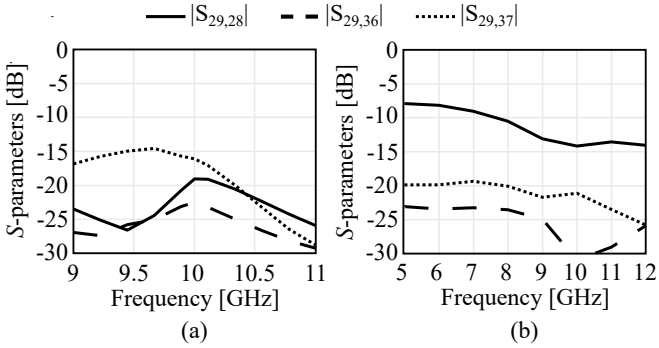

Figure 3.13: S parameters of the 8×8 array of (a) patches and (b) connected slots.

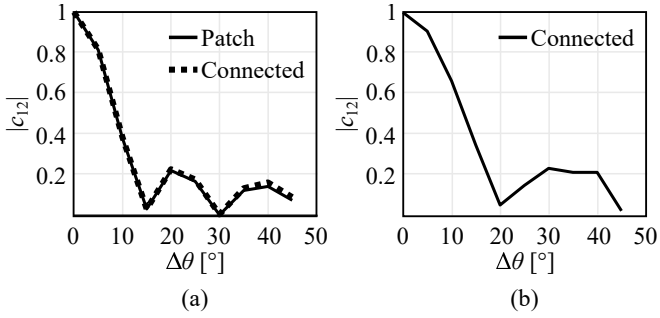

Figure 3.14: Beam coupling between two beams, pointing at broadside and $\Delta\theta$, respectively, for 8×8 planar arrays of resonant patches and connected slots at (a) $f = 10\,\mathrm{GHz}$, and (b) $f = 7\,\mathrm{GHz}$.

3.4. Conclusions

We presented a study on the beam coupling factor in multibeam arrays. The coupling coefficients were expressed in terms of the current distributions, the mutual impedance and the inter-element mutual coupling. The study dealt with arrays of dipoles, more specifically comparing resonant dipoles with connected dipoles. These latter are known to have much higher levels of mutual coupling, which is typically used to enlarge the operation bandwidth.

When using the array in the one-beam-per-feed configuration, the coupling between elements is directly related to beam coupling, thus is not desired. However, when different beams are generated by the entire 'active' array, the beam correlation is mainly determined by the beam overlap and it is weakly dependent on the mutual coupling. We showed that the beams can remain uncoupled even with high inter-element mutual coupling, as long as the beams do not overlap and the active impedance is well behaved. Finally, an example of planar arrays is given to further support the investigation.

The findings of this chapter are relevant for the exploitation of wideband arrays in multi-beam communication, which can enable enhanced capability in future wireless networks.

Chapter 4

A Connected Array Design for Sub-8 GHz Massive MIMO

I have nothing to offer but blood, toil, tears and sweat
–Sir Winston L. S. Churchill

4.1. Introduction

The fifth generation (5G) communication standard exploits massive Multiple Input Multiple Output (MIMO) to achieve high data rate streams [18, 51, 121]. With this paradigm, directive beams are radiated toward the different users and steered over a wide field of view to track the user's movements. This motivates the need for wide-scanning arrays to cover the entire field of view with a limited number of antenna panels (e.g., three panels with a scan range of $\pm 60°$).

Moreover, 5G relies on the possibility of transmitting information over different frequency ranges of the electromagnetic spectrum. Several bands are already in use between 2 and 6 GHz, and one more band located between 6.425 and 7.125 GHz, i.e., the upper 6 GHz (U6G) band [122], will be licensed in a few years. Resonant antennas are currently being employed on base stations. However, due to their narrowband properties, multiple antenna arrays are needed to transmit over all the required bands, leading to several radiators competing for the same space or increasing the overall space occupied by the base station. For this reason, wideband arrays that can operate simultaneously over multiple bands with a single aperture are gaining interest for 5G applications both for the sub-6 GHz band [123, 124], and for the millimeter wave

frequencies [125–127]. Although wideband arrays are characterized by a high inter-element mutual coupling, they can still operate in a MIMO environment by generating independent beams, as discussed in [52, 117] and in Chapter 3.

The past decade has witnessed great advances in the development of phased arrays with wideband and wide-scanning capability. Several solutions have been proposed in the literature, including tapered slot antennas [128–130], metal flared-notch elements [131, 132], long-slot arrays [133, 134] and tightly-coupled or connected dipole arrays [135–139]. Despite the significant advance of wideband phased arrays, the main target applications of these antennas have been defense radars, satellite communications, and radio astronomy. Their use for commercial wireless communications has been hindered by the high complexity and the high cost typically involved in the manufacturing of wideband arrays. Most of these arrays are realized with vertically oriented printed circuit boards (PCBs), which are difficult to assemble and unsuitable for mass production. Planar solutions based on a single multi-layer PCB have been proposed to reduce the complexity for tightly coupled dipoles in [140, 141], and more recently for connected slots in the presence of artificial dielectric layers (ADLs) in [41, 45]. This latter exploits ADL superstrates, consisting of layers made of sub-wavelength square metal patches, which synthesize an equivalent anisotropic medium [49]. The advantages of an ADL superstrate can be summarized as follows:

1. It diverts a large fraction of the power radiated by the slots towards the upper medium, allowing to reduce the distance from the ground plane so that standard through-hole via technology can be used to realize the feeding lines;

2. It acts as a wideband impedance transformer between the free space and the feed impedance of the slots;

3. It increases the scan range by suppressing the surface waves.

In this chapter, we present the design of an array based on the connected slot element with ADL superstrate, as shown in Fig. 4.1(a) for the simplified single-polarized unit cell. The focus of this design is to show the flexibility of the concept by using the same connected array with different ADL radomes to select its operational bandwidth, as shown in Fig. 4.1(b). In this way, a single antenna section can be used for different applications and environments. As the ADL acts as an impedance transformer, the array impedance bandwidth is strongly related to the ADL design and can be enlarged by increasing the number of metal layers and the overall height of the ADL stackup. More specifically, two ADLs designs are presented, one operating from 6 to 8 GHz, referred to as narrowband (NB), and the other operating from 2 to 8 GHz, indicated as wideband (WB). In both cases, the array can scan up to 60° in both main planes within the frequency bands mentioned above. Furthermore, the WB ADL radome presented here improves the bandwidth of this concept with respect to previous designs [41, 45], by targeting two octaves. Finally, an 8×8 dual polarized

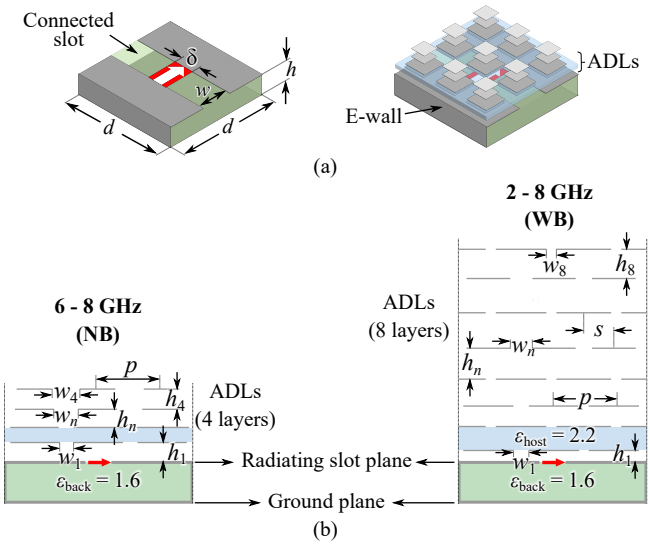

Figure 4.1: (a) Sketch of the single polarized connected unit cell without and with the ADL radome, and (b) side view of the array consisting of the common radiating section and the interchangeable ADLs radomes.

Table 4.1: Geometrical parameters (in mm) of the narrowband (NB) ADL Radome

h_1	h_2	h_3	h_4	w_1	w_2	w_3	w_4
0.64	1.53	2.50	3.48	0.50	0.53	1.31	1.3

prototype array is realized, and the resulting measurements are presented with both NB and WB radomes.

4.2. Unit Cell Design

4.2.1. ADL Synthesis

The first step of the unit cell design involves the synthesis of the ADLs to realize a two- and four-section Chebyshev impedance transformer for the NB and WB, respectively. The impedance transformers, aimed at matching the feeding line of the array element

Table 4.2: Geometrical parameters (in mm) of the wideband (WB) ADL Radome

h_1	h_2	h_3	h_4	h_5	h_6	h_7	h_8
0.5	2.24	2.95	3.40	3.65	4.90	5.79	6.67

w_1	w_2	w_3	w_4	w_5	w_6	w_7	w_8
0.35	0.18	0.33	0.17	0.63	0.63	1.76	1.76

to free space, are initially modeled as the cascade of multiple quarter-wave sections of ideal transmission lines. Each transmission line section can be represented as a homogeneous and isotropic dielectric slab as if a single plane wave were impinging from broadside. Then, each slab is replaced with ADLs having, for normal incidence, the same effective refractive index of the corresponding homogeneous dielectric [42, 43], using the ADL closed-form description derived in [48]. For the case at hand, this results in a transformer made of four and eight layers of patches for the NB and WB case, respectively.

In the ADLs radome design, we introduce a dielectric slab of relative permittivity $\varepsilon_{\text{host}} = 2.2$ between the first two bottom layers. In this way, we obtain a less varying effective permittivity with respect to the scan angle for transverse magnetic (TM) waves and in turn, a more stable active impedance when scanning in the E-plane. The thin dielectric can also be seen as a wide-angle impedance matching layer as originally introduced in [142].

Both of the synthesized ADL radomes have a period $p = 5$ mm, and the other geometrical parameters defined in Fig. 4.1(b) have the values listed in Table 4.1 and Table 4.2 for the NB and the WB ADL, respectively. The parameter s indicates the shift between odd and even layers in the ADL stack. No inter-layer shift is applied in the NB ADL radome, i.e., the gaps between patches in different layers are vertically aligned. On the contrary, the maximum shift $s = p/2$ has been used for all the metal layers of the WB ADL, resulting in a glide symmetric structure that is characterized by a larger effective permittivity [49].

4.2.2. Single-Polarized Unit Cell

The single-polarized (single-pol) connected slot unit cell is sketched in Fig. 4.1(a), and it is designed in the presence of the ADL using the analytical procedure illustrated in [45]. To enhance the bandwidth, the period is set to $d = 0.4\lambda_0^{8\text{GHz}} = 15\,\text{mm}$, and

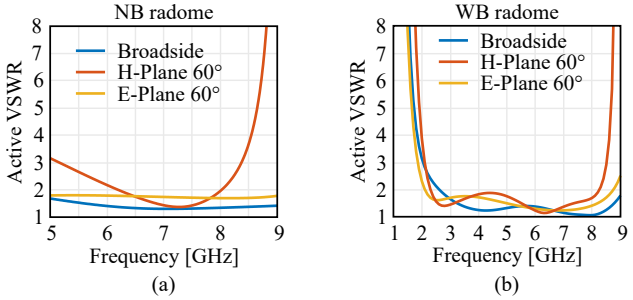

Figure 4.2: Active VSWR of the single polarized unit cell for broadside, H-plane 60° and E-plane 60° scanning for (a) the NB ADL, and (b) the WB ADL radome.

vertical walls have been added between parallel slots (E-walls) to avoid the propagation of guided modes in the substrate below the slots [45]. The slot has a width $w = 0.1\lambda_0^{8\text{GHz}}$, it is fed by a δ-gap generator with length $\delta = 0.24\lambda_0^{8\text{GHz}}$, and it is separated from the ground plane by a dielectric with thickness $h = 3.5\,\text{mm}$ and relative permittivity $\varepsilon_{\text{back}} = 1.6$.

The corresponding active Voltage Standing Wave Ratio (VSWR) is shown in Fig. 4.2. For the NB radome, the active VSWR is <2.2 when scanning up to 60° on the main planes over the frequency bands of interest, i.e., 6-8 GHz. For the WB radome, a VSWR <2 is obtained when scanning up to 60° in the main planes over most of the 2-8 GHz frequency band, with an increase to VSWR=3 at the low end of the band (2 GHz).

4.2.3. Dual-Polarized Unit Cell

By using CST Microwave Studio, the dual-polarized (dual-pol) unit cell sketched in Fig. 4.3 is designed. This comprises two sets of orthogonal 45° tapered slots, each excited by a microstrip below the array plane, as shown in Fig. 4.3(a). The feeding microstrip is terminated with a capacitive plate that compensates for the inductive effect of the ground plane. The microstrip is connected with an integrated coaxial line that goes through the holed ground plane to the outer SMP connector, as shown in Fig. 4.3(b). The integrated coaxial line also has the role of suppressing modes that would otherwise propagate between the ground plane and the slot plane [45]. The specific design for the integrated coaxial feed and for the microstrip transition to the SMP connector is reported in [143]. To avoid the excitation of waves guided by the slot when scanning in the H-plane, the dielectric used to sustain the array plane has been milled into a grid to obtain a lower effective permittivity. The detailed stackups of the array and radomes boards used for the prototyping are shown in Fig. 4.3(c)

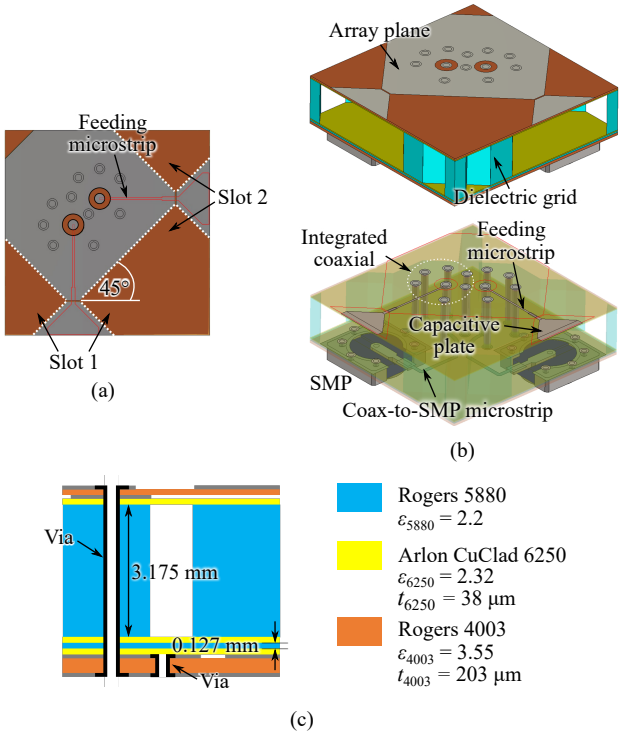

Figure 4.3: Sketch of the dual polarized unit cell: (a) top view, (b) three-dimensional view, highlighting the array plane, the feeding components, and the dielectric grid, and (c) side view of the stackup.

and 4.4, respectively. The ADL geometry has been slightly adjusted to account for the effect of the realistic materials on the layers' reactance.

The simulated active VSWR is shown in Fig. 4.5 for the NB and WB case, respectively. The VSWR of the NB case is lower than 2 for broadside and E-plane scanning to 60° over the 6-8 GHz range, while it increases to 2.3 when scanning in the H-plane to 60° at 8 GHz. For the WB radome, the simulations show a VSWR<3 in the 2-8 GHz band for broadside and E-plane scanning, while the bandwidth is reduced to 2.3-8 GHz when scanning to the maximum angle in the H-plane.

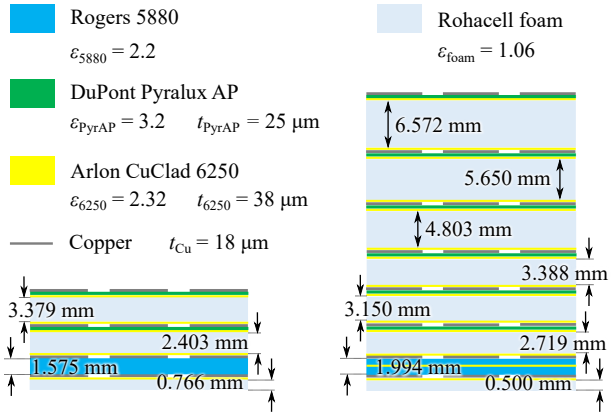

Figure 4.4: Stackup of the prototyped NB and WB ADL radomes.

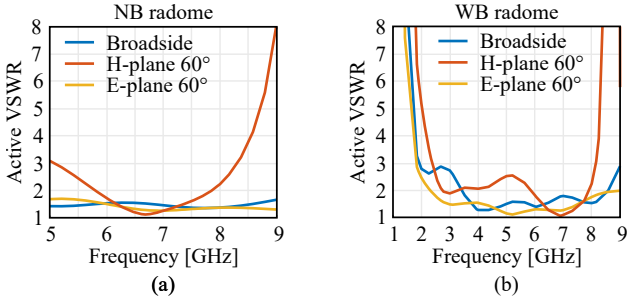

Figure 4.5: Active VSWR of the dual polarized unit cell for broadside, H-plane 60° and E-plane 60° scanning for (a) the NB ADL, and (b) the WB ADL radome.

4.3. Connected Array Prototype

An 8×8 array, based on the dual-polarized unit cell of Fig. 4.3, has been manufactured [see Fig. 4.6(a)-(b)] as a representative prototype. The two manufactured ADL radome boards are shown in Fig. 4.6(c) and have a total thickness of 8.4 mm and 29.5 mm for the NB and WB, respectively. The antenna is mounted in a holder with the NB or the WB ADL radome, as shown in Fig. 4.6(d). The radomes are larger than the slot array, as they are intended to be used also for larger antenna arrays or multiple tiles.

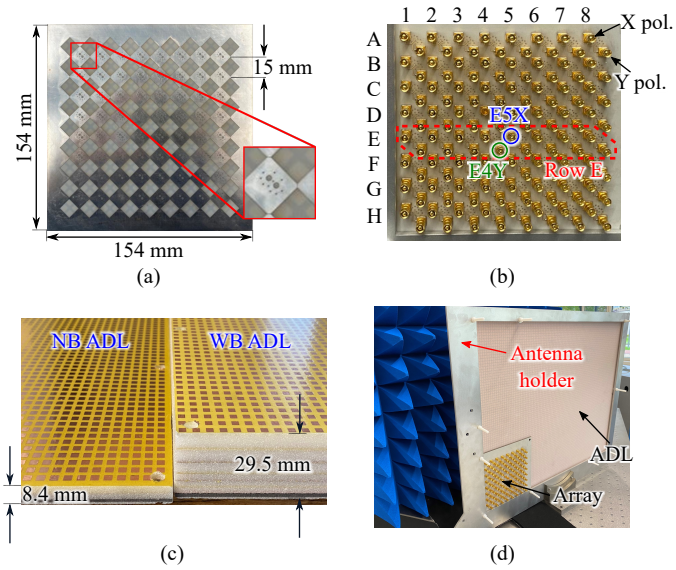

Figure 4.6: (a) Front and (b) back view of the manufactured 8×8 dual polarized connected slot array prototype, (c) photo of the NB and WB ADL radomes, and (d) the full setup with array prototype, the NB ADL radome, and the holder.

4.3.1. Measured Active Matching

All the S-parameters between the elements E5X and E4Y [see Fig. 4.6(b)] and the rest of the array are measured for the NB and WB case, respectively. Then, these are combined with complex weights corresponding to the different scanning and taper conditions, to obtain the active reflection coefficient and VSWR.

The active VSWR of E5X with the NB radome is shown in Fig. 4.7 for broadside, and scanning to 60° in the main planes. As can be noticed, the fully excited array of Fig. 4.7(a) has a good agreement with the simulated unit cell results when scanning in the main planes. The measured active VSWR for broadside is slightly higher than the unit cell simulation for frequencies above 7 GHz. This can be partly attributed to finite edge effects, as an amplitude taper applied to both rows and columns is shown to lower the VSWR below 2.5 on the band of interest, as shown in Fig. 4.7(b).

The measured active VSWR of the element E4Y with the WB radome is shown in Fig. 4.8, for different scanning and illumination conditions. The strong mismatch at 3.5 GHz in Fig. 4.8(a) is due to the resonant size of the full array. In fact, the tapered excitation of Fig. 4.8(b) effectively removes the resonance. Even in the presence of the amplitude taper, some fast oscillations are seen at around 6 GHz and above. These were observed to be caused by a somewhat unstable connection of the coaxial cables

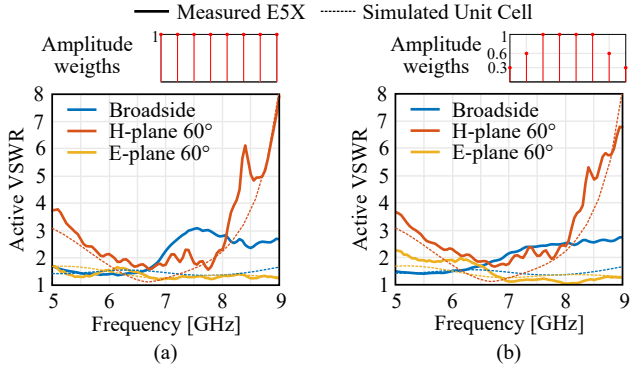

Figure 4.7: Measured active VSWR of E5X, when using the NB ADL radome, for broadside, H-plane 60° and E-plane 60° scanning for (a) the fully excited array and (b) the array with a tapered excitation.

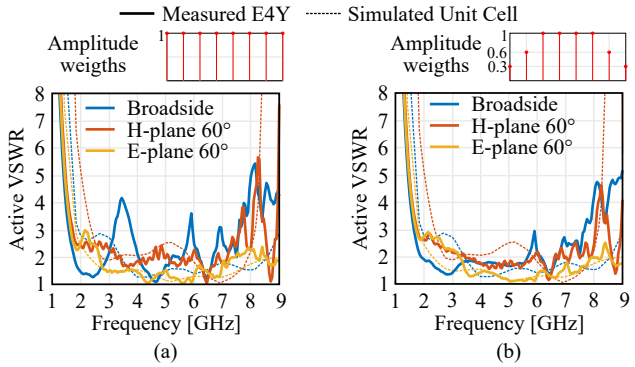

Figure 4.8: Measured active VSWR of E4Y, when using the WB ADL radome, for broadside, H-plane 60° and E-plane 60° scanning for (a) the fully excited array and (b) the array with a tapered excitation.

with the smooth bore SMP connectors that gave some variability of the S-parameters depending on the specific position in which the cables were held. Nevertheless, as shown in Fig. 4.8(b), when applying an amplitude taper, the VSWR of the element E4Y is <3 in the band from 1.7 to 7.6 GHz, corresponding to a 4.5:1 bandwidth.

To verify that the peak at 3.5 GHz is due to the edge effects, an $8 \times \infty$ array simulation has been performed. Fig. 4.9 shows the active VSWR of a central element, exhibiting a resonance around 3 GHz, which is mitigated when introducing an amplitude taper.

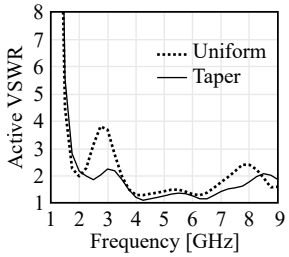

Figure 4.9: Simulated active VSWR of a central element in the $8 \times \infty$ configuration for a uniform illumination and an amplitude taper.

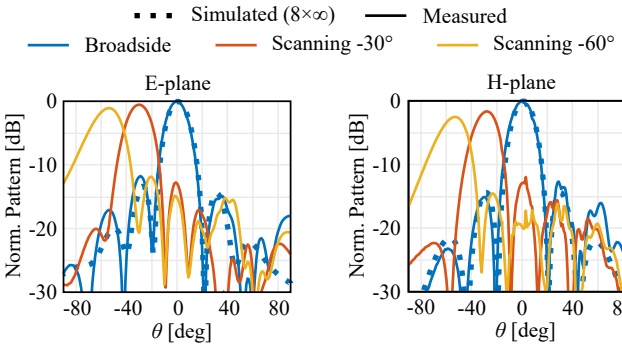

Figure 4.10: Measured and simulated ($8 \times \infty$) array patterns on the E-plane and on the H-plane at 7 GHz in the presence of the NB ADL radome.

4.3.2. Measured Patterns

When operating with either radomes, the E- and H-plane Embedded Element Patterns (EEP) have been measured for all the elements of both polarizations located in row E [see Fig. 4.6(b)]. To compensate for the manufacturing tolerances and errors introduced by the measurement setup, the amplitudes and phases of the EEPs are adjusted to compensate for the variations in the broadside direction (i.e., a broadside calibration). Then, the desired array patterns are calculated and shown in Fig. 4.10 and 4.11 for the NB and WB case, respectively. The patterns of the uniformly illuminated array are shown at 7 GHz for the NB case and at 2, 5, and 7.5 GHz for the WB case and compared with $8 \times \infty$ CST simulations. A good agreement can be recognized for the main lobes and the Side Lobe Level (SLL), while the discrepancies for larger observation angles are credited to the diffraction from the metal frame. The scanning array patterns are normalized with respect to the broadside values. As it can be noticed, the E- and the H-plane have different scan loss. This difference is mainly

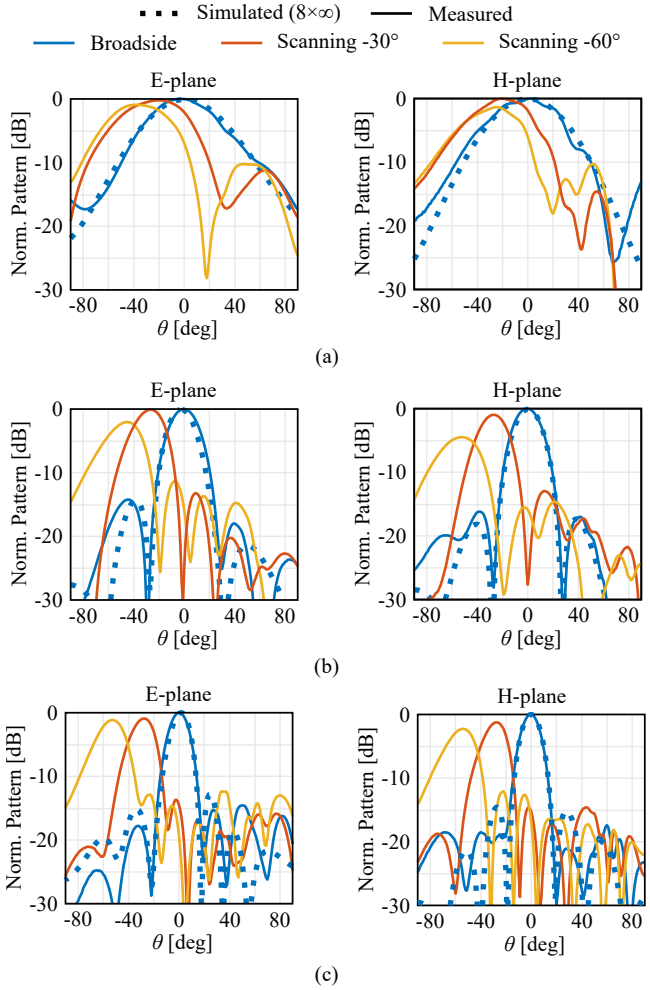

Figure 4.11: Measured and simulated ($8 \times \infty$) array patterns in the E-plane and in the H-plane at (a) 2 GHz, (b) 5 GHz, and (c) 7.5 GHz in the presence of the WB ADL radome.

due to the different shapes of the EEP in the two planes. The EEPs of the elements in the central row are presented in Fig. 4.12, showing a larger decay for the H-plane. Moreover, when scanning in the H-plane, a slightly higher mismatch occurs with respect to the E-plane. Due to edge effects, oscillations are present in the EEPs, larger in the H-plane compared to the E-plane. Nevertheless, these fluctuations average out when the EEPs are combined together, creating smooth array patterns. Moreover,

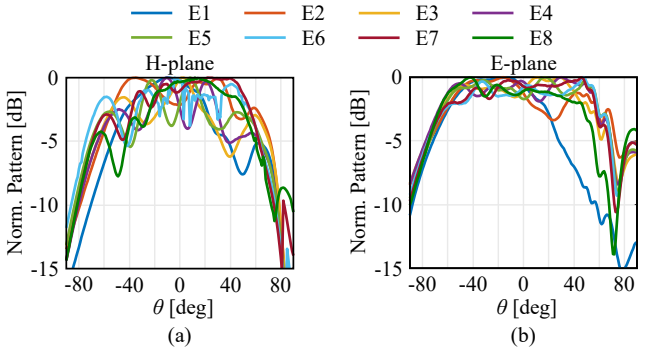

Figure 4.12: Measured embedded element patterns on the (a) H-plane and (b) E-plane at 7 GHz in the presence of the NB ADL radome.

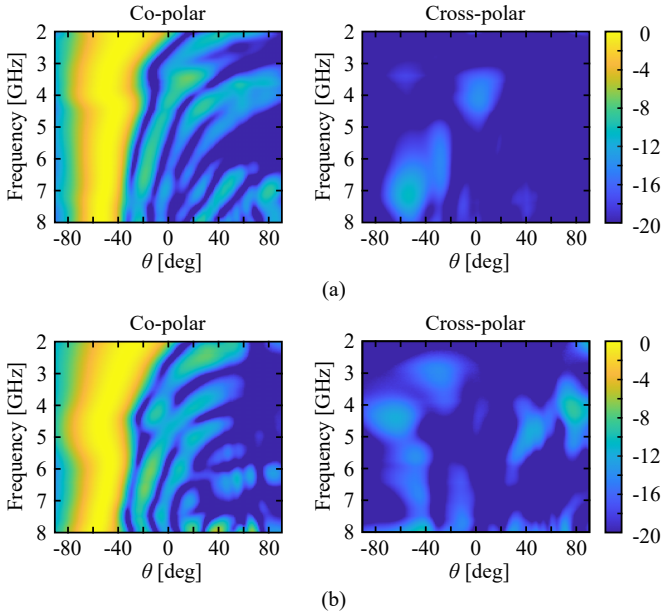

Figure 4.13: Measured co-polar and cross-polar component when scanning towards -60° on the (a) E-plane and (b) H-plane with the WB radome.

the diffraction from the metal frame supporting the antenna is visible, especially in the E-plane for large angles.

Radiators in the presence of ADLs exhibit increased cross-polarization levels, especially in the diagonal plane (D-plane). However, in the desired application the

scanning in azimuth is much larger than in elevation, e.g., ±20° in the urban scenario of [144], reducing the scanning requirements in the D-plane. In Fig. 4.13 the co- and cross-polar are shown when scanning towards 60° on the E- and H-plane, exhibiting between 2 and 7.6 GHz a rejection better than −10 and −12 dB, respectively.

4.4. Conclusion

A dual-polarized planar connected slot array has been designed to target sub-8 GHz 5G applications. The same radiating aperture is used with two interchangeable ADL radomes, one for 6-8 GHz operation and the other for 2-8 GHz.

An 8×8 connected array prototype has been manufactured and tested for its impedance and radiation characteristics. When using a tapered illumination, this shows a VSWR<2.5 when scanning up to 60° with the NB ADL radome over the targeted band and a VSWR<3 when scanning up to 60° with the WB ADL radome between 1.7 to 7.6 GHz.

II

The Modelling of Integrated Antennas

Chapter 5

Full-wave Lens Antenna Analysis with the Proxy Sources Method

Sapere aude! 'Have courage to use your own reason!'- that is the motto of enlightenment
–Immanuel Kant, *An answer to the question: what is enlightenment?*

5.1. Introduction

In the sub-mm wave domain, some of the most successful examples of front-end integration resort to lens antennas [24, 35, 75, 145–150]. The analysis and design of such antennas typically require the accurate modeling of the input impedance, mutual coupling, and radiation patterns. Due to the electrically large size of the lenses, high-frequency techniques, such as the Physical Optics (PO) [75], have played a major role in easing the analysis of quasi-optical systems, allowing to avoid time consuming full wave simulations.

Recently, small-size lens antennas have gained popularity due to their employment flexibility. These have been used as elements for coherent arrays [33] or as the core in the core-shell lens [63, 64]. In these cases, the PO based on ray tracing [65–76] become inaccurate [77] because the curvature of the surfaces is small with respect to the wavelength. These limitations call for developing analysis techniques that allow for efficient analysis without compromising accuracy.

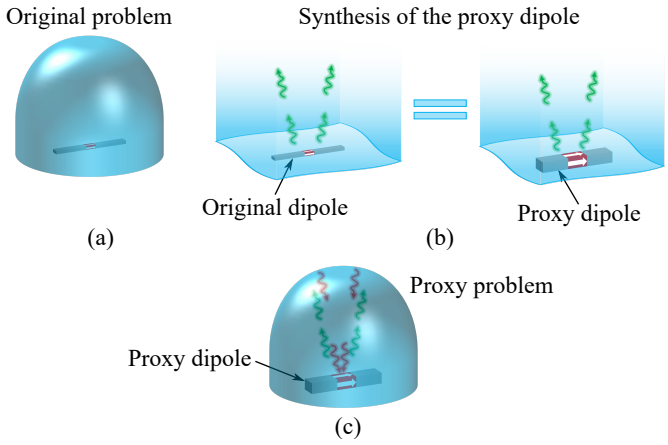

Figure 5.1: Representation of (a) the original problem, (b) the synthesis of the proxy dipole in the absence of the reflections, and (c) the proxy problem.

For these reasons, full-wave solvers can be employed to analyze dielectric lenses, including also their integrated feed [see Fig. 5.1(a)]. However, in the sub-mm wave regime, the thickness of the metal cannot be neglected being it comparable with the other design parameters, and impacting the performance, as shown in Chapter 6 and 7, and this yields challenging multi-scale simulations.

To circumvent this issue, a strategy to decouple the analysis of the feed from the lens is developed. The lens creates the reflections coming from its boundaries, which are wave phenomena generated at a distance from the feed, and therefore, weakly dependent on its specific geometry. A proxy dipole is synthesized with a much coarser discretization such that it radiates equivalently into the dielectric half space having the same permittivity of the lens Fig. 5.1(b). This allows to study the proxy problem Fig. 5.1(c) with a much coarser mesh, and improved solution times.

This concept is independent of the specific numerical technique used. It finds its largest benefit when structured meshes are employed, but it can also be applied for unstructured meshes when a large imbalance between the feed size and its surroundings is present.

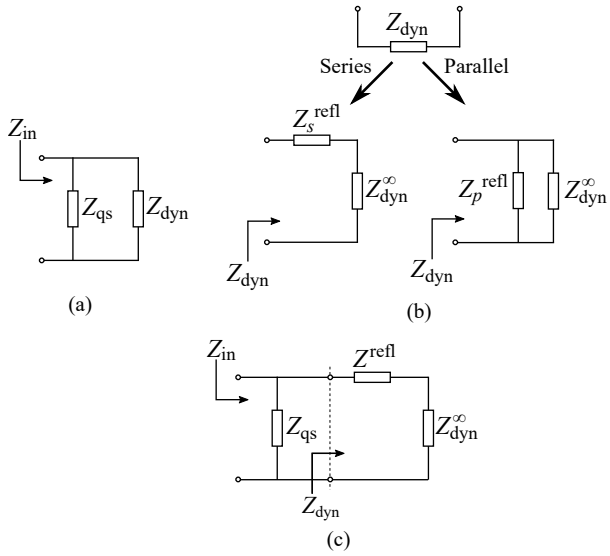

Figure 5.2: Equivalent circuit representation of (a) the parallel of the dynamic and the quasi-static components of the input impedance, (b) the dynamic component of the input impedance with the series and parallel representation of the reflections, and (c) the complete equivalent circuit of an integrated lens antenna.

5.2. Equivalent Circuit of a Dipole Illuminating a Dielectric Lens

5.2.1. The Dynamic and Quasi-Static Component

From the derivation in Chapter 6, the input impedance Z_{in} of a dipole can be approximated, as shown in Fig. 5.2(a), as the parallel between the quasi-static component Z_{qs}, associated with the capacitance of the gap and the dynamic impedance Z_{dyn}, associated with a wave propagating on the dipole and causing the radiation. In the spectral domain, Z_{dyn} corresponds to the low part of the spectrum, which is dominated by a pole, while Z_{qs} is associated with the high part of the plane-wave spectrum.

5.2.2. The Reflection Component of the Input Impedance

The input impedance of any antenna is defined as the ratio between integrals on the input ports of the electric field and the magnetic field when one of the two fields is

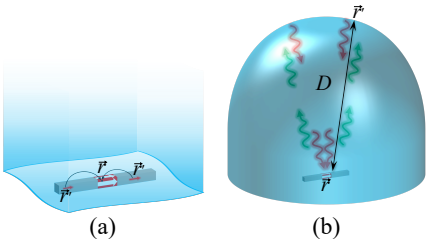

Figure 5.3: Representation of (a) the near field interaction in the feed, and (b) the direct radiation and the reflections from the lens.

assumed to be the excitation and the other is the unknown of the problem. If a dielectric body is present, a fraction of the radiated fields is reflected by the dielectric-air interface back to the feeding ports, changing the impedance (or the admittance) with respect to the case without the reflections [151]. As the reflections are due to radiative phenomena, these are associated with the dynamic component of the impedance (or the admittance). As the antenna input port can be arbitrarily represented with a series or parallel equivalent circuit [see Fig. 5.2(b)], the correction due to the reflections can be added to the dynamic component calculated in the absence of the reflections. Consequently, the dynamic component of the input impedance or admittance can be expressed as follows

$$Z_{\text{dyn}} = Z^{\infty}_{\text{dyn}} + Z^{\text{refl}}_{s} \tag{5.1}$$

$$Y_{\text{dyn}} = Y^{\infty}_{\text{dyn}} + Y^{\text{refl}}_{p} \tag{5.2}$$

where Z^{∞}_{dyn} and Y^{∞}_{dyn} are the dynamic components of the impedance and the admittance, respectively, calculated without the reflections and Z^{refl}_{s} and Y^{refl}_{p} are the impedance and admittance, respectively, associated with the reflections. The values of the impedance added in series or parallel are generally different. As in the following, we intend to work with the impedance, we always refer to the series model (5.1), and to avoid redundancy, the subscript s is, from now on, omitted.

It is important to stress how Z^{∞}_{dyn} and Z^{refl}_{s} depend on the near and the far-field of the feed. The fields required for the evaluation of the impedances of (5.1) are observed in the gap at $\vec{r}$ and are generated by the equivalent currents at $\vec{r}\,'$, induced by the excitation. The field in the absence of the reflections, i.e., the one associated with Z^{∞}, is evaluated in the near field of the dipole, and it has a fast space variability being calculated with a Green's function $\propto |\vec{r} - \vec{r}\,'|^{-3}$ [see Fig. 5.3(a)]. On the contrary, if the boundaries of the dielectric are sufficiently distant from the dipole, the field associated with the reflections varies less rapidly as the field propagates from the dipole to the boundaries and backward, with a path length D, having a length of the same order of the diameter [see Fig. 5.3(b)], and the Green's function

of the reflections is dominated by the $\propto (|\vec{r} - \vec{r}'| + D)^{-1}$ term. Due to its fast space variability, the impedance calculated without the reflections depends on the specific geometry, while the impedance associated with the reflections depends mainly on the dynamic component of the currents and not on the specific shape of the feed.

5.3. Calculation of the Input Impedance with the Proxy Sources Method

As stated in Section 5.1, the modelling includes the introduction of the *proxy* dipole, which allows a convenient simulation together with the lens. This dipole is characterized by a discretization much coarser than the original one, but which radiates equally in the absence of the reflections, as shown in Fig. 5.1(b). This constraint is expressed by the following condition

$$\mathrm{Re}\{Z^{\infty}_{\mathrm{proxy}}\} \approx \mathrm{Re}\{Z^{\infty}_{\mathrm{dyn}}\} \tag{5.3}$$

where $Z^{\infty}_{\mathrm{proxy}}$ is the dynamic component of the proxy dipole in the absence of the reflections. As the discretization of the proxy dipole is much coarser than the original one, it has a larger feeding gap, and consequently a negligible quasi-static component. The condition (5.3) for the synthesis is imposed only on the dynamic part the far-field radiation is independent of the quasi-static part Z_{qs}, which can be added in post-processing. By using the separation of the wave phenomena as in Section 5.2.2 and by using (5.3), the input impedance of the proxy dipole can be approximated as follows

$$Z_{\mathrm{proxy}} \approx \mathrm{Re}\{Z^{\infty}_{\mathrm{dyn}}\} + \mathrm{Im}\{Z^{\infty}_{\mathrm{proxy}}\} + Z^{\mathrm{refl}}_{\mathrm{proxy}}. \tag{5.4}$$

Since the original and the proxy dipoles have been synthesized in (5.3) to radiate equivalently, it is reasonable to assume that

$$Z^{\mathrm{refl}}_{\mathrm{proxy}} \approx Z^{\mathrm{refl}}. \tag{5.5}$$

Therefore, the reflections can be extracted from (5.4) as follows

$$Z^{\mathrm{refl}} \approx Z_{\mathrm{proxy}} - \mathrm{Re}\{Z^{\infty}_{\mathrm{dyn}}\} - \mathrm{Im}\{Z^{\infty}_{\mathrm{proxy}}\}. \tag{5.6}$$

Then, the input admittance of the original dipole in the finite medium can be estimated as follows

$$Z_{\mathrm{in,dyn}} \approx Z^{\infty}_{\mathrm{dyn}} + Z^{\mathrm{refl}}_{\mathrm{proxy}}. \tag{5.7}$$

Finally, the input impedance can be obtained by adding Z_{qs} in parallel

$$Z_{\mathrm{in}} = Z_{\mathrm{in,dyn}} \parallel Z_{\mathrm{qs}}. \tag{5.8}$$

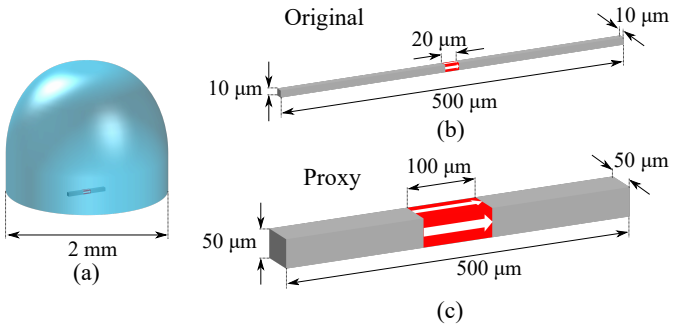

Figure 5.4: Sketch of (a) the lens fed by a dipole, (b) the original dipole, and (c) the proxy one.

$Z^{\infty}_{\mathrm{dyn}}$ is calculated with the extraction of Z_{qs} from the input impedance of the original dipole radiating in the absence of the reflections. There are no constraints on the methods used to derive this latter, which can be evaluated with a commercial solver, a spectral domain representation of Chapter 7, or with the same in-house full-wave solver used to extract the reflections. The final steps (5.7) and (5.8) can be represented by the equivalent circuit in Fig. 5.2(c).

5.4. Results and Applications

5.4.1. Dielectric Lens Fed by a Single Dipole

The first example simulates with the volumetric method of moments based on Appendix C and a structured mesh a dipole long $\ell = 0.5\,\mathrm{mm}$ placed on the focus of an elliptical lens with a diameter 2 mm and dielectric permittivity $\varepsilon_r = 2.34$ [see Fig. 5.4(a) and (b)]. The dipole has a square cross-section with a side $w_y = w_z = 10\,\mu\mathrm{m}$, and it is fed by a Δ-gap generator $\Delta = 20\,\mu\mathrm{m}$ long, as shown in Fig. 5.4(b). A structured mesh would require a discretization of at least 10 µm, i.e., the side of the cross-section, yielding 16×10^6 unknowns. With the proposed method, it is possible to use the volumetric method of moments and a structured mesh and achieve comparable results by using an proxy dipole having a square cross section of 50 µm [see Fig. 5.4(c)], and 141×10^3 unknowns for the entire problem.

The original dipole is first simulated with the method of moments when radiating at the interface between free space and an dielectric half space with permittivity $\varepsilon_r = 2.34$, and its impedance in the absence of reflections is calculated. This condition is realized with the method of moments, by adding a matching layer over the dielectric. The quasi-static impedance Z_{qs} is then isolated, and the dynamic component Z_{dyn} is

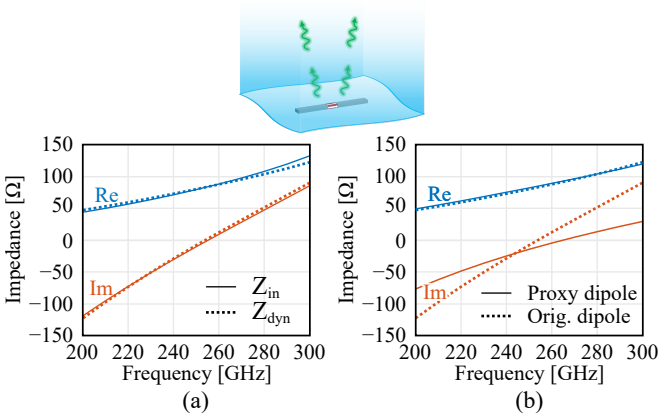

Figure 5.5: (a) Input impedance and its dynamic component, of the original dipole radiating in the semi-infinite medium, and (b) synthesis of the proxy dipole.

shown in Fig. 5.5(a), where it is compared with the total input impedance. The proxy dipole is synthesized with the method of moments, by changing the cross section, the gap length, and the length of a much coarsely discretized dipole until minimizing the difference between the real parts of Z^{∞}_{aux} and Z^{∞}_{dyn}. The input impedance of the proxy dipole is shown in Fig. 5.5(b). Then, the proxy dipole radiating into the lens is efficiently simulated, thanks to the coarse discretization, and its input impedance is shown in Fig. 5.6(a). The reflections are then extracted with (5.6) and are shown in Fig. 5.6(b). Finally, the input impedance of the original dipole is estimated with (5.8), and its values are shown in Fig. 5.6(c), where these are compared with the direct simulation. Note that the direct full wave simulation is possible to perform due to the relatively small size of the problem. In Fig. 5.6(b), the reflections from the lens extracted with the original dipole are compared with those extracted with the proxy one. This successful comparison proves that the specific geometry of the feed does not affect the interaction with the lens if it is equivalently radiating in the far-field.

In Fig. 5.7(a), the directivity patterns of the proxy and original problems are compared in the E- and H-planes. Due to the condition (5.3) and the fact that the details of the feed do not affect the far-field, the original and proxy dipoles share the same pattern. In Fig. 5.7(b), the directivity patterns of the lens fed by the proxy dipole are shown at 250 GHz, and the values obtained with the proposed method are compared with CST and the PO [76]. As the PO fields have been calculated for $\theta \in [0^\circ\ 90^\circ]$, the patterns of the method of moments and CST are normalized to the power radiated in the upper hemisphere only. The patterns obtained by the proposed

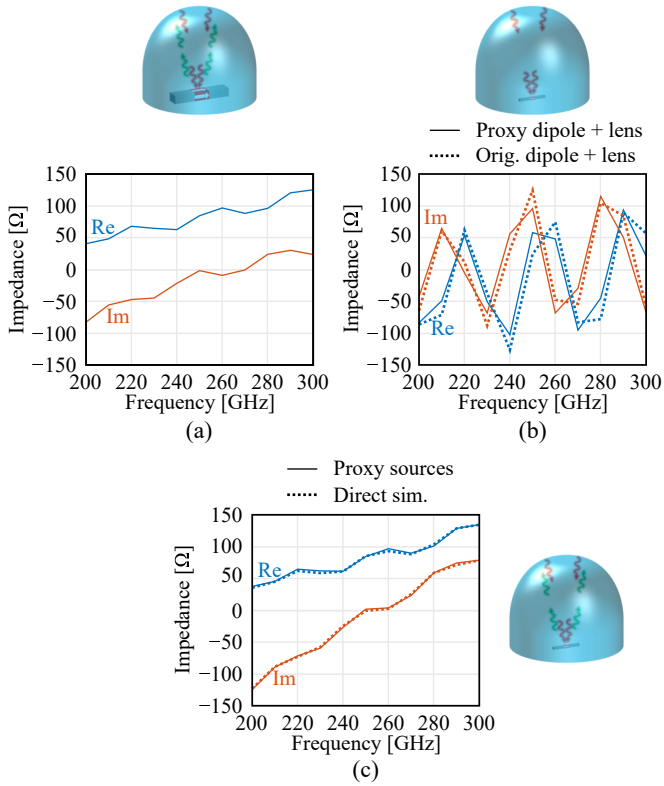

Figure 5.6: (a) Input impedance of the proxy dipole illuminating the lens, (b) the reflection component of the impedance extracted from the proxy and the original dipole, and (c) input impedance of the original dipole illuminating the lens simulated with the proxy sources method and with the direct simulation.

method are in excellent agreement with CST, while the larger error committed by the PO further confirms its inaccuracy for the study of small lens antennas.

To show the validity of this procedure for off-focus dipoles, the feed of the previous geometry is shifted by 750 µm on the H-plane, an extreme configuration, considering that the lens radius is 1 mm. As the synthesis does not depend on the geometry of the surrounding dielectric, the synthesized proxy dipole is still the one of Fig. 5.4(c) and 5.5(b). The input impedance is compared in Fig. 5.8(a) with the standard simulation of the dipole displaced under the lens, showing an excellent agreement. The patterns on the H-plane at 250 GHz are shown in Fig. 5.8(b), where the directivity calculated with this method is compared with CST and the PO. As before, the directivity is

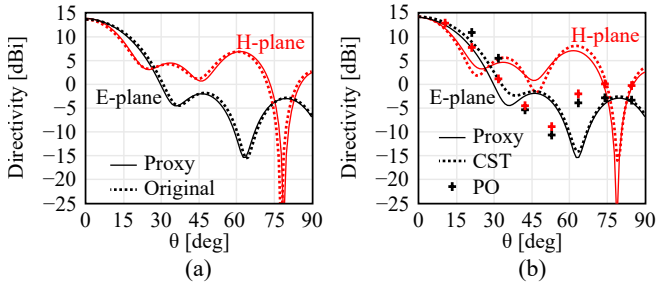

Figure 5.7: Directivity plots of the lens (a) illuminated by the proxy and original dipole, and (b) assessed with the proxy sources method, CST, and the PO.

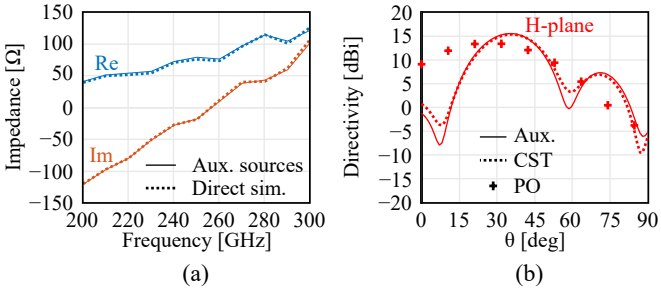

Figure 5.8: (a) Comparison between the input impedance calculated for the shifted dipole with the proxy sources method and the direct simulation, and (b) the directvity in the H-plane calculated at 250 GHz with the method of moments (proxy sources), CST, and the PO.

calculated by considering the power radiated in the upper hemisphere.While the patterns calculated with the proxy sources maintain a good accuracy also in off-focus configurations, the PO commits larger errors.

5.4.2. Dielectric Lens Fed by a Double Dipole

The procedure can be extended to the analysis of a dielectric lens with relative permittivity $\varepsilon_r = 2.34$ fed by the double-dipole shown in Fig. 5.9(a). Due to the presence of the two feeding gaps, the synthesis of the proxy dipoles is carried out on the active impedances, i.e., the impedances when both dipoles are excited. The original double-dipole radiating in the semi-infinite medium is obtained with a CST simulation, as the high level of detail implies a computational burden that is too heavy for the method of moments with a structured mesh. The quasi-static component is extracted from a single dipole as this is only due to the capacitive effects around the gap, and does

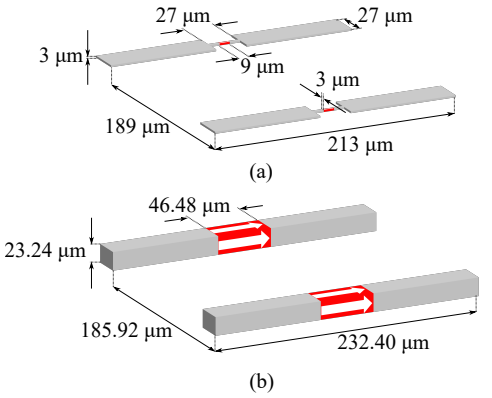

Figure 5.9: Representation of (a) the original, and (b) the proxy double dipole.

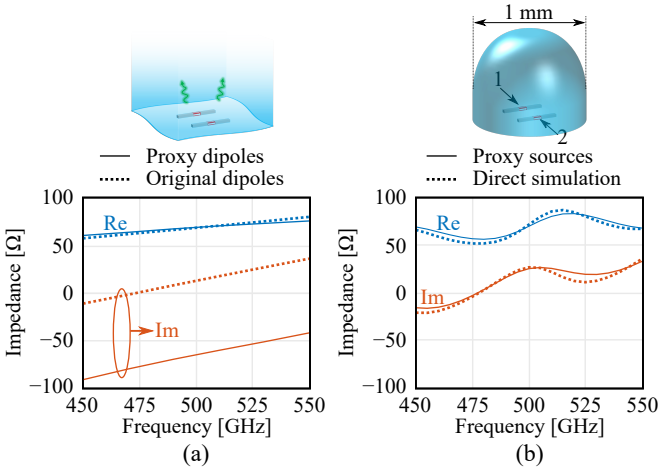

Figure 5.10: (a) Synthesis of the proxy double dipole, and (b) input impedance of the lens fed by the double dipole calculated with the proxy sources method and with the direct simulation.

not impact on the mutual coupling between the dipoles. The two proxy dipoles in an array configuration are synthesized with the method of moments, resulting into the coarser and simpler geometry shown in Fig. 5.9(b). The synthesis results are shown in terms of active input impedance in Fig. 5.10(a). The double-dipole is used to illuminate from its focus a dielectric lens with diameter 1 mm. The input impedance calculated with the proxy sources method is compared with the direct CST simulation in Fig. 5.10(b), and showing a good agreement. This example shows that the proxy sources method can be extended to the analysis of complex realistic feeds. Moreover,

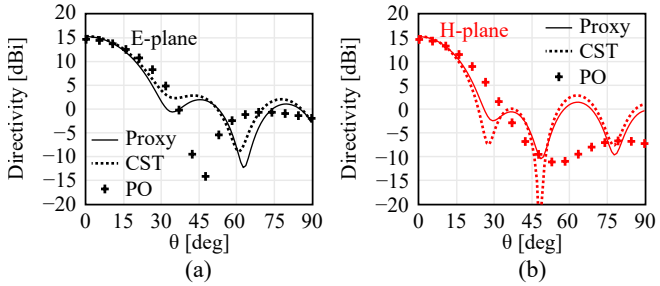

Figure 5.11: Directivity patterns at 500 GHz in (a) the E-, and (b) the H-plane.

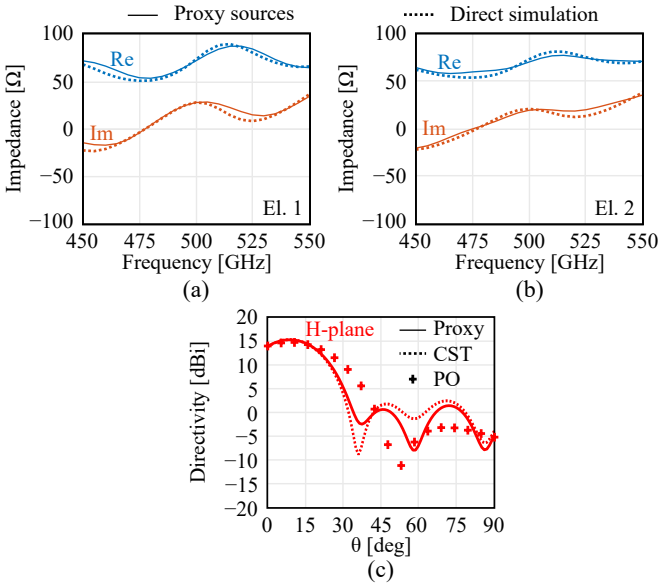

Figure 5.12: Input impedance of (a) element 1 and (b) element 2, calculated with the proxy sources method and the direct simulation, and (c) the directivity patterns at 500 GHz in the H-plane.

this case of study also proves the flexibility of the method, as it shows that the simulation of a radiator close to a dielectric body can be simplified by separating the feed from the interaction with the body, where these two contributions can be simulated with different approaches. Finally, the patterns on the E- and H-plane at 500 GHz are shown in Fig. 5.11 (a) and (b), respectively, showing a better agreement with CST rather than with the PO.

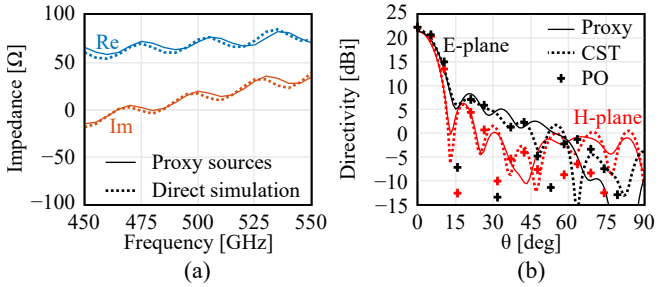

Figure 5.13: (a) Comparison of the input impedance of the lens calculated with the proxy sources method and with the direct simulation and (b) the directivity patterns in the E- and the H-plane at 500 GHz.

The same lens has also been studied in an off-focus configuration, where the feed is displaced by 93 µm in the H-plane. For this analysis the proxy dipole of Fig. 5.9(b) and Fig. 5.10(a) is used. The input impedance of element one and two is shown in Fig. 5.12(a) and (b), respectively. Differently from the previous case, each dipole has a different input impedance, as the off-focus configuration is not symmetric. The patterns are shown in Fig. 5.12(c), with an improved comparison with the PO due to the smaller scanning angle.

To test the potential of this method, the same feed of Fig. 5.9(a) and Fig. 5.10(a) is used to illuminate a larger lens with a diameter of 2.5 mm, i.e., $5\lambda_0$. The results in terms of the input impedance and the patterns are shown in Fig. 5.13 for the double dipole placed in the focus and in Fig. 5.14 for the dipole shifted by 139 µm from the focus.

5.5. Conclusion

The equivalent circuit representation of a feed illuminating a dielectric lens antenna is derived. This separates the capacitance of the feeding gap from the reflections created by the finite dielectric and from the propagation in an unbounded medium. This allows for the formulation of the proxy sources method to ease the full wave simulations of integrated lens antennas. The input impedance can be calculated by combining the impedance in the absence of the reflections with the reflections extracted from the lens fed by the proxy feed. The impedance in the unbounded medium can be obtained with fast full-wave simulations or a semi-analytical solution such as in Chapter 7. The proxy dipole has the same interaction with the lens, but it is coarser than the actual one, therefore allowing efficient full-wave simulations.

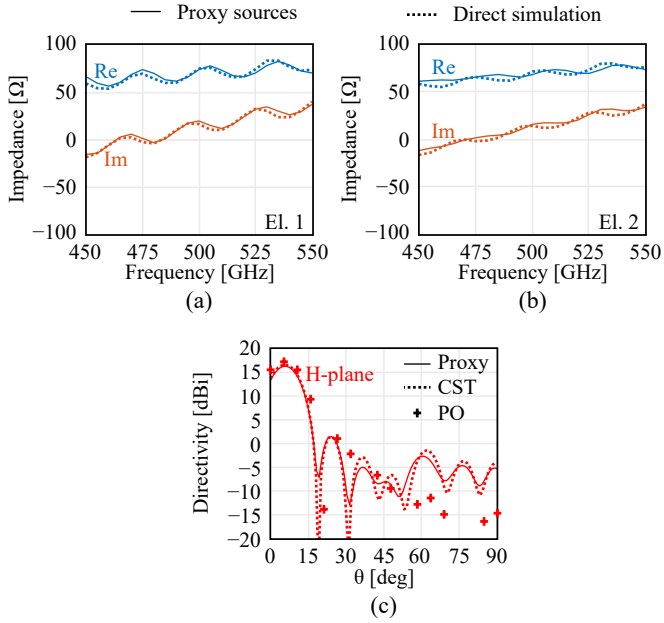

Figure 5.14: Input impedance of (a) element 1 and (b) element 2, calculated with the proxy sources method and the direct simulation, and (c) the directivity patterns at 500 GHz in the H-plane.

The method is validated against the PO and against direct simulations obtained with either commercial solvers or in-house codes. While it shows up-to-par accuracy with respect to full wave solvers, it proves better performance than the PO, especially when dealing with small-size lenses.

Chapter 6

The Green's Function of an Infinitely Long Dipole with Nonzero Metal Thickness

La filosofia è scritta in questo grandissimo libro che continuamente ci sta aperto innanzi a gli occhi (io dico l'universo), ma non si può intendere se prima non s'impara a intender la lingua, e conoscer i caratteri, ne' quali è scritto. Egli è scritto in lingua matematica, e i caratteri son triangoli, cerchi, ed altre figure geometriche, senza i quali mezi è impossibile a intenderne umanamente parola...

Philosophy is written in this all-encompassing book that is constantly open to our eyes, that is the universe; but it cannot be understood unless one first learns to understand the language and knows the characters in which it is written. It is written in mathematical language, and its characters are triangles, circles, and other geometrical figures; without these it is humanly impossible to understand a word of it...

–Galileo Galilei, *Il Saggiatore*

6.1. Introduction

The analysis of printed dipoles and microstrips has been the subject of a large body of scientific literature [152]. Nowadays, there are several commercial tools [153–156] that can easily provide an accurate estimation of the characterizing parameters. Moreover, to increase the speed and accuracy of the analysis, in the last thirty years, transmis-

sion line Green's functions (TL GF) have emerged, [157–162]. These can perform an efficient analysis and provide physical insight into the dispersion properties of open-ended lines. In fact, relying on these transmission line GF, antennas such as leaky wave lenses [163], slots [164], and connected arrays [39] are nowadays routinely designed.

The Terahertz Sensing Group has developed a user-friendly code [165] that implements the TL GF for the most used open line configurations, as described in [166]. These latter lines have become relevant with the advances of sub-mm wave architectures and the corresponding micro-metric sizes. Unfortunately, the TL GF formulation cannot include the metal thickness as a characterizing parameter to date. The metal thickness can be a design parameter if one wishes, for instance, to realize a resistor or, on the contrary, minimize the losses in an integrated transmission line. In this chapter, a TL GF formulation for dipoles of nonzero metal thickness embedded in general stratifications is described. Our formulation models the current in the cross-section with a single basis function, as [157, 159], and [166]; however, the basis function also represents the vertical current profile.

The spectral domain formulation, similarly to [157, 159], allows to derive the current spectrum, and from this the characteristic impedance, the propagation constant, and the losses of the line are extracted. In addition, a transmission line equivalent circuit is introduced to characterize the input impedance of the dipole. The circuit includes a term associated with the characteristic impedance of the line and the reactance associated with the delta-gap excitation, which is dependent on the cross-section and the length of the gap.

6.2. Formulation

Let us consider the infinitely long dipole shown in Fig. 6.1(a) and (b), embedded in an arbitrary stratification, oriented along the x-axis, constituted by a homogeneous material having a conductivity σ (or equivalently a resistivity $\rho = 1/\sigma$), having a rectangular cross-section A, w_y wide and w_z thick, and excited by a feeding port Δ long. If the port is sufficiently small, the fringing of the incident field can be neglected, and it can be considered as a Δ-gap generator, where the field is assumed to be uniform. The current flowing in the dipole is assumed to have only the axial component, i.e., oriented along $\hat{x}$. As the width of the dipole is much smaller than the wavelength, the current distribution can be written as the product of a longitudinal and a transverse distribution. By resorting to the local form of Ohm's law, i.e., $\vec{j} = \sigma\vec{e}$, by expressing the total field as the sum of the incident and the scattered one, the following expression is obtained

$$\rho\, i(x)\, j_t(y,z) = v(x)\, e_t^i(y,z) + e_x^s(x,y,z) \tag{6.1}$$

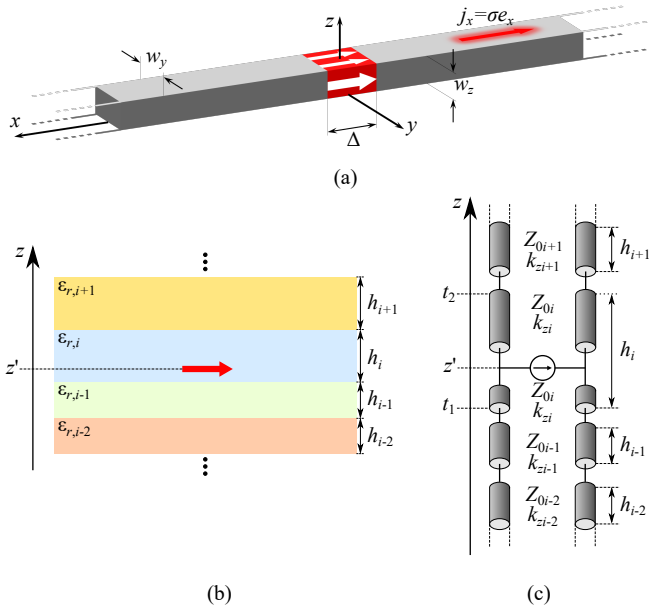

Figure 6.1: (a) Sketch of an infinitely long dipole oriented along x, w_y wide and w_z thick, and excited by a δ-gap generator Δ long, (b) vertical section of the dipole in an arbitrary stratification, and (c) transmission line equivalent representation of the stackup.

where $i(x)$ and $j_t(y,z)$ are the longitudinal and transverse dependencies of the current distribution, respectively, $v(x)$ and $e_t^i(y,z)$ are the longitudinal and transverse expressions of the incident field, and $e_x^s(x,y,z)$ is the x-component of the scattered field. As the excitation is modeled as a Δ-gap generator Δ long, $v(x)$ and $e_t^i(y,z)$ can be written as follows

$$v(x) = \frac{V_0}{\Delta}\,\mathrm{rect}\left(\frac{x}{\Delta}\right) \tag{6.2}$$

$$e_t^i(y,z) = \mathrm{rect}\left(\frac{y}{w_y}\right)\mathrm{rect}\left(\frac{z}{w_z}\right) \tag{6.3}$$

where rect is the rectangular pulse, i.e., $\mathrm{rect}\,(x) \coloneqq 1\ \forall |x| < 1/2$, and V_0/Δ is the magnitude of the incident field on the gap. By isolating the incident field on the left-hand side, and by expressing the scattered field as the radiation from the currents on the dipole, one can write the following expression

$$\frac{V_0}{\Delta}\,\mathrm{rect}\left(\frac{x}{\Delta}\right)\mathrm{rect}\left(\frac{y}{w_y}\right)\mathrm{rect}\left(\frac{z}{w_z}\right) = \rho\, i(x)\, j_t(y,z) - g_{xx}^{EJ}(x,y,z,z') * [i(x)\, j_t(y,z)] \tag{6.4}$$

where $g_{xx}^{EJ}(x,y,z,z')$ is the xx-component of the stratified media Green's function providing the electric field from the electric currents, located at z', and the symbol $*$ is a spatial convolution in x and y which in its extended form has the following expression

$$\int_{-\infty}^{+\infty}\int_{-w_y/2}^{w_y/2}\int_{0}^{w_z} g_{xx}^{EJ}(x-x',y-y',z,z')i(x')j_t(y',z')\,dx'dy'dz'. \tag{6.5}$$

The Green's function g_{xx}^{EJ} in (6.5) can be expressed in the spectral domain as follows

$$g_{xx}^{EJ}(x-x',y-y',z,z') = \frac{1}{4\pi^2}\int_{-\infty}^{+\infty}\int_{-\infty}^{+\infty}\Big[G_{xx}^{EJ}\left(k_x,k_y,z,z'\right) \times e^{-jk_x\left(x-x'\right)}e^{-jk_y\left(y-y'\right)}\Big]dk_xdk_y \tag{6.6}$$

where $G_{xx}^{EJ}\left(k_x,k_y,z,z'\right)$ is the spectral domain stratified media Green's function, with k_x and k_y being the wavenumber domain counterparts of the x and y coordinates, and which is known [167, App. A.3] having the following analytical expression

$$G_{xx}^{EJ}\left(k_x,k_y,z,z'\right) = -\frac{v_{\mathrm{TM}}\left(z,z'\right)k_x^2 + v_{\mathrm{TE}}\left(z,z'\right)k_y^2}{k_x^2+k_y^2} \tag{6.7}$$

where $v_{\mathrm{TM}}\left(z,z'\right)$ and $v_{\mathrm{TE}}\left(z,z'\right)$ are the voltage solutions at z of the TM and TE transmission line equivalent problems, as shown in Fig. 6.1(c), when the sources are placed at z'. Their calculation is carried out as in [167, App. A].

Thanks to the rectangular cross-section, the dependence of the transverse current distribution j_t can be assumed to be as follows

$$j_t\left(y,z\right) = j_{t,y}\left(y\right)j_{t,z}\left(z\right). \tag{6.8}$$

By substituting (6.6) in (6.5), one can calculate the Fourier transforms of i and j_t with respect to x' and y', and obtain the following expression for the scattered field

$$e_x^s\left(x,y,z\right) = \frac{1}{4\pi^2}\int_{-\infty}^{+\infty}\int_{-\infty}^{+\infty}\int_{0}^{w_z}\Big[G_{xx}^{EJ}(k_x,k_y,z,z')I(k_x)J_{t,y}(k_y)\,j_{t,z}\left(z'\right) \times e^{-jk_xx}e^{-jk_yy}\Big]dz'dk_xdk_y. \tag{6.9}$$

where $I(k_x)$ is the Fourier transform of i, performed with respect to x, and $J_{t,y}(k_y)$ is the Fourier transform of $j_{t,y}(y)$. One can more conveniently express (6.4) in the spectral domain, where the spectra in k_x can be equated as for infinitely long dipoles, the equality holds for every x, yielding

$$V_0 \operatorname{sinc}\left(\frac{k_x\Delta}{2}\right) e_t^i(y,z) = I(k_x)\left[\rho j_t(y,z) - \frac{1}{2\pi}\int_{-\infty}^{+\infty}\int_{0}^{w_z} G_{xx}^{EJ}(k_x,k_y,z,z')\, J_{t,y}(k_y) \times j_{t,z}(z') e^{-jk_y y} dz' dk_y\right]. \quad (6.10)$$

One can first define the following inner product

$$\langle f, g\rangle_A = \iint_A f(y,z)\, g^*(y,z)\, dydz \quad (6.11)$$

and can then apply it to the left and the right-hand side of (6.10) on the test function $\tilde{j}_t$, which is expressed as follows

$$\tilde{j}_t(y,z) = \tilde{j}_{t,y}(y)\, \tilde{j}_{t,z}(z)\,. \quad (6.12)$$

This can be defined having a unitary flux on the cross-section, i.e., $\langle \tilde{j}_t, e_t^i\rangle_A = 1$, and therefore the Fourier transform of the current I along the dipole can be calculated as follows

$$I(k_x) = \frac{V_0 \operatorname{sinc}(k_x\Delta/2)}{D(k_x)} \quad (6.13)$$

where $\operatorname{sinc} \coloneqq \sin(x)/x$ is the Fourier transform of the rect function, and D is the transverse Green's function of the dipole, defined in the following manner

$$D(k_x) = \rho\langle j_t, \tilde{j}_t\rangle_A - \frac{1}{2\pi}\int_{-\infty}^{+\infty}\int_{0}^{w_z}\int_{0}^{w_z}\Big[G_{xx}^{EJ}(k_x,k_y,z,z') J_{t,y}(k_y)\tilde{J}_{t,y}(-k_y) \times j_{t,z}(z')\tilde{j}_{t,z}^*(z)\Big] dzdz'dk_y. \quad (6.14)$$

By taking advantage of the formulation in [168, eq. (72)], whose steps are reported for the sake of completeness in Appendix D.1, the integrals in z and z' can be calculated analytically for suitable choices of j_t and $\tilde{j}_t$. For the specific choice of the basis functions used in this chapter, their analytical result of (6.14) is reported in

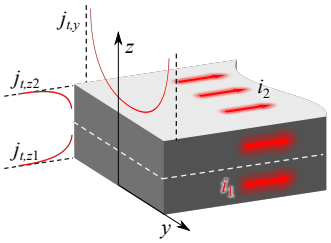

Figure 6.2: Sketch of the current distribution on the dipole, highlighting the y-dependent distribution $j_{t,y}(y)$, the z-dependent distributions $j_{t,z1}(z)$ and $j_{t,z2}(z)$, and the currents on the axis $i_1(x)$ and $i_2(x)$.

Appendix D.2. The current distribution along y in (6.8) can be defined having the following edge singular behavior as in [159]

$$j_{t,y}(y) = \frac{2}{\pi w_y} \frac{1}{\sqrt{1-\left(\frac{2y}{w_y}\right)^2}} \operatorname{rect}\left(\frac{y}{w_y}\right). \tag{6.15}$$

and for (6.12) as follows

$$\tilde{j}_{t,y}(y) = \frac{\operatorname{rect}(y/w_y)}{w_y}. \tag{6.16}$$

to allow for the convergence when calculating the projections in (6.14).

6.2.1. Profile of the Currents Along z

The choice of $j_{t,z}$ in (6.8) and $\tilde{j}_{t,z}$ in (6.12) must take into account the stratification where the dipole is embedded in, as imbalanced currents flow on the top and the bottom part of the metal. To this aim, the current flow is split into two distributions, each representing a wave propagating in a lossy metal [169]. The current distributions on the bottom and on the top part of the metal, respectively, are the following

$$j_{t,1}(y,z) = \frac{(1+j)\, j_{t,y}(y)\, e^{-(1+j)z/\delta_p}}{\delta_p\left(1-e^{-(1+j)w_z/\delta_p}\right)} \operatorname{rect}\left(\frac{z-w_z/4}{w_z/2}\right) \tag{6.17}$$

$$j_{t,2}(y,z) = \frac{(1+j)\, j_{t,y}(y)\, e^{-(1+j)(z-w_z)/\delta_p}}{\delta_p\left(1-e^{(1+j)w_z/\delta_p}\right)} \operatorname{rect}\left(\frac{z-3w_z/4}{w_z/2}\right). \tag{6.18}$$

where δ_p is the penetration depth, and as sketched in Fig. 6.2. When the penetration depth becomes comparable with w_z, the current profile along z has to include also

the multiple reflections at the interfaces, which are not accounted for in the proposed method. In fact, to obtain a semi-analytical solution, the current is approximated with a reduced number of basis functions. In addition to this, to ease the analytical calculations, due to its compact Fourier transform, we have chosen for the current distribution along y the edge singular distribution (6.15), which does not depend on δ_p. Therefore, these assumptions imply approximated results in the low-frequency regime. By performing the projections on the test functions $\tilde{j}_{t,1}$ and on $\tilde{j}_{t,2}$, which are the split-current counterpart of (6.12), the following matrix equation is written

$$\begin{bmatrix} V_1(k_x) \\ V_2(k_x) \end{bmatrix} = \begin{bmatrix} \langle e_t^i, j_{t,1} \rangle_A \\ \langle e_t^i, j_{t,2} \rangle_A \end{bmatrix} \operatorname{sinc}\left(\frac{k_x \Delta}{2}\right) = \begin{bmatrix} D_{11}(k_x) & D_{12}(k_x) \\ D_{21}(k_x) & D_{22}(k_x) \end{bmatrix} \begin{bmatrix} I_1(k_x) \\ I_2(k_x) \end{bmatrix} \tag{6.19}$$

with $I_1(k_x)$ and $I_2(k_x)$ being the spectrum of the currents flowing on the bottom and on the top side, respectively, as shown in Fig. 6.2. The entries $D_{mn}(k_x)$ are defined in the following manner

$$D_{mn}(k_x) = \rho \langle j_{t,m}, \tilde{j}_{t,n} \rangle_A - \frac{1}{2\pi} \int_{-\infty}^{+\infty} \int_0^{w_z} \int_0^{w_z} \Big[G_{xx}^{EJ}(k_x, k_y, z, z') J_{t,y}(k_y) \tilde{J}_{t,y}(-k_y) \times j_{t,zm}(z') \, j_{t,zn}^*(z) \Big] dz dz' dk_y \tag{6.20}$$

and by resorting to [168] to express the stratified media Green's function, thanks to the chosen current distributions, the space-domain integrals of (6.20) can be solved analytically. The solution of (6.19) is given in the following expressions

$$I_1(k_x) = \frac{D_{22}(k_x) V_1(k_x) - D_{12}(k_x) V_2(k_x)}{\det(\mathbf{D}(k_x))} \tag{6.21}$$

$$I_2(k_x) = \frac{D_{11}(k_x) V_2(k_x) - D_{21}(k_x) V_1(k_x)}{\det(\mathbf{D}(k_x))} \tag{6.22}$$

where $\det(\mathbf{D}(k_x))$ is the 2×2 matrix determinant. By solving the dispersion equation $\det(\mathbf{D}(k_x)) = 0$, one can find the two poles $k_{xp,1}$ and $k_{xp,2}$. This allows us to interpret the currents propagating on either the top or bottom part as the superposition of two contributions expressed as follows

$$i_{1,\mathrm{res},h}(x) = -j \frac{D_{22} V_1 - D_{12} V_2}{(\det(\mathbf{D}))'} e^{-jk_x x} \Big|_{k_x = k_{xp,h}} \tag{6.23}$$

$$i_{2,\mathrm{res},h}(x) = -j \frac{D_{11} V_2 - D_{21} V_1}{(\det(\mathbf{D}))'} e^{-jk_x x} \Big|_{k_x = k_{xp,h}} \tag{6.24}$$

where the index h denotes either pole 1 or pole 2. The current on either the bottom (6.23) or the top (6.24) of the dipole is the superposition of the modes associated with pole 1 and pole 2. By calculating the imbalance between the currents as follows

$$R = \left. \frac{i_{1,\mathrm{res},1}(x) + i_{1,\mathrm{res},2}(x)}{i_{2,\mathrm{res},1}(x) + i_{2,\mathrm{res},2}(x)} \right|_{x=0} \tag{6.25}$$

one can write a single asymmetric transverse current distribution as follows

$$j_{t,z}(z) = \frac{(1+j)\left(R\, e^{-(1+j)z/\delta_p} + e^{(1+j)(z-w_z)/\delta_p}\right)}{\delta_p (R+1)\, e^{-(1+j)w_z/\delta_p}\left(e^{(1+j)w_z/\delta_p} - 1\right)} \operatorname{rect}\left(\frac{z - w_z/2}{w_z}\right) \tag{6.26}$$

to be used in (6.8) to calculate the transverse Green's function (6.14), to be used in the current spectrum (6.13). The analytical solution of the integrals of (6.14) involving (6.26), are given in the supplementary material.

6.3. Results

The present section discusses the applications the formulation derived in Section 6.2.

6

6.3.1. Dipole in Free Space

For a dipole in free-space, due to the symmetry of the problem, the parameter R from (6.25) is equal to unity, resulting into the following current profile along z

$$j_{t,z}(z) = \frac{(1+j)\left(e^{-(1+j)z/\delta_p} + e^{(1+j)(z-w_z)/\delta_p}\right)}{2\delta_p e^{-(1+j)w_z/\delta_p}\left(e^{(1+j)w_z/\delta_p} - 1\right)} \operatorname{rect}\left(\frac{z - w_z/2}{w_z}\right) \tag{6.27}$$

and where the following free-space Green's function is used

$$G_{xx}^{EJ} = -\frac{j\zeta}{k} \frac{k^2 - k_x^2}{\sqrt{k^2 - k_x^2 - k_y^2}}. \tag{6.28}$$

The current distribution $i(x)$ can be found by calculating the following inverse Fourier transform

$$i(x) = \frac{1}{2\pi} \int_{-\infty}^{+\infty} \frac{V_0 \operatorname{sinc}(k_x \Delta/2)}{D(k_x)} e^{-jk_x x} dk_x \tag{6.29}$$

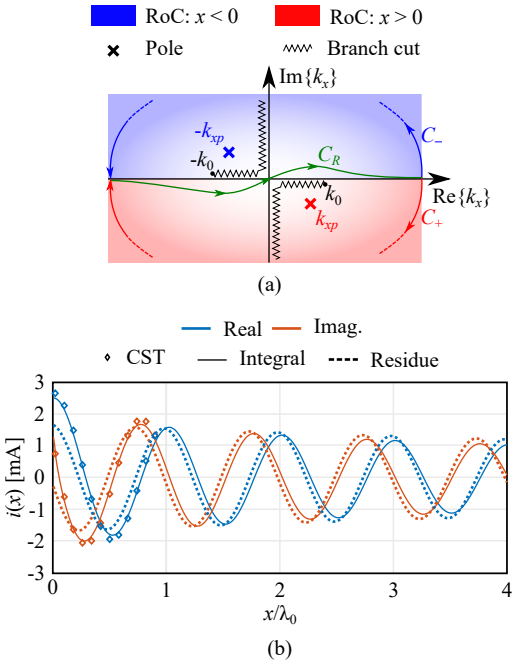

Figure 6.3: (a) The complex plane topology for (6.29), and (b) the current along a dipole in free-space calculated with the inverse Fourier transform of (6.13), with the residue contribution, and CST for $w_y = w_z = 10\,\mu\mathrm{m}$, $\Delta = 20\,\mu\mathrm{m}$, $\sigma = 1 \times 10^6\,\mathrm{S/m}$, and having unitary excitation.

where the integration path C_R has been deformed around the real axis to avoid the square-root branch cuts in the k_x-plane, as shown in Fig. 6.3(a). The region of convergence (RoC) of (6.29) depends on the observation point x. If $x < 0$ the convergence is guaranteed for $\mathrm{Im}\{k_x\} > 0$, otherwise for $x > 0$ in the half plane $\mathrm{Im}\{k_x\} < 0$, therefore the path needed to close the integral at infinity has to be chosen accordingly, as shown in Fig. 6.3(a), and depending on the path either the pole k_{xp} or $-k_{xp}$ results enclosed.

As an example, the current is calculated at f=300 GHz for a dipole excited with 1 V and having $w_y = w_z = 10\,\mu\mathrm{m}$, $\Delta = 20\,\mu\mathrm{m}$, and $\sigma = 10^6\,\mathrm{S/m}$, resulting in a good agreement with CST as reported in Fig. 6.3(b). As shown, the residue contribution alone does not fully represent the current along the dipole at a large distance from the feed. As shown in [170] and [171], an infinite dipole in free space also supports a space wave with logarithmic decay.

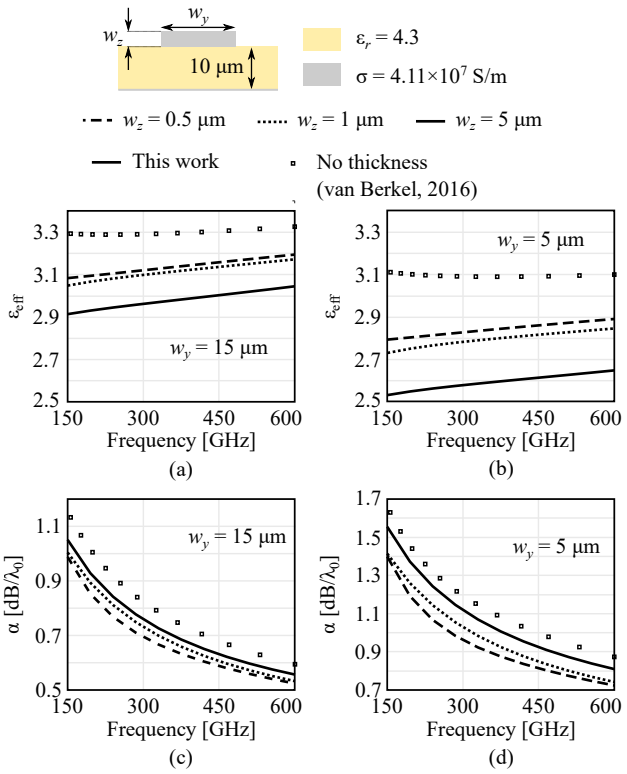

Figure 6.4: Real part of the characteristic impedance for (a) $w_y = 15\,\mu\text{m}$ and (b) $w_y = 5\,\mu\text{m}$ and attenuation constant for (c) $w_y = 15\,\mu\text{m}$ and (d) $w_y = 5\,\mu\text{m}$ of a dipole constituted by a material of conductivity $\sigma = 4.11 \times 10^7$ S/m, printed over a grounded slab thick $d = 10\,\mu\text{m}$ for different values of the metal thickness w_z.

6.3.2. Microstrip

Unlike the dipoles in homogeneous space, some topologies support a dominant residue contribution. For instance, if the dipole is backed by a ground plane, the radiation from the feed is negligible, and thus, the residue contribution provides the dominant propagating wave. The effective permittivity and the losses associated with the propagating mode are shown in Fig. 6.4 for different different metal widths and thicknesses.

For the topologies that support a dominant residue contribution, i.e., dipoles embedded in stratifications that significantly alter the propagation constant with respect to free space, a characteristic impedance Z_0 can be defined for the mode associated

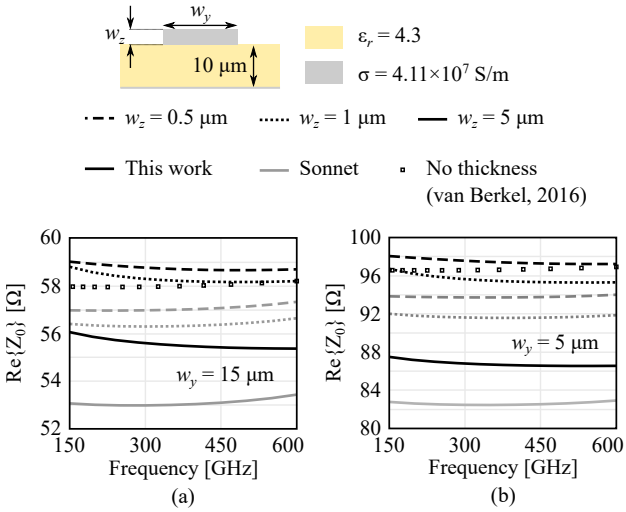

Figure 6.5: Real part of the characteristic impedance for (a) $w_y = 15\,\mu\text{m}$ and (b) $w_y = 5\,\mu\text{m}$ of a dipole constituted by a material of conductivity $\sigma = 4.11 \times 10^7\,\text{S/m}$, printed over a grounded slab thick $d = 10\,\mu\text{m}$ for different values of the metal thickness w_z.

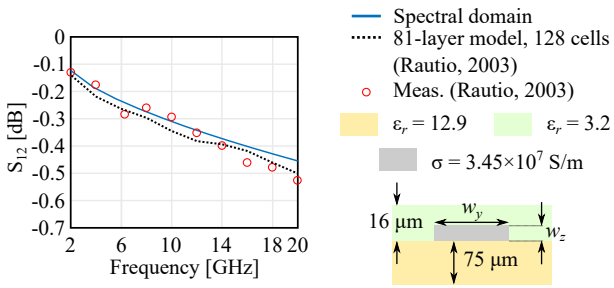

Figure 6.6: S_{12} comparison between the measurements and the simulations of the 81-layers model with 128 cells of [174], and the spectral domain characterization.

with the residue, defined as in [172], [173] as follows

$$Z_0 = j\frac{D'(k_{xp})}{2}. \tag{6.30}$$

The characteristic impedance is instrumental for the definition of an equivalent circuit that can be used to accurately characterize the impact of the dimensions of the feeding gap.

The characteristic impedance Z_0 is evaluated for the dipole shown in Fig. 6.5. It is constituted by a material of conductivity $\sigma = 4.11 \times 10^7\,\text{S/m}$ and it is printed

over a grounded slab thick $d = 10\,\mu\text{m}$ having a relative permittivity $\varepsilon_r = 4.3$. Given the topology, it is a microstrip. Fig. 6.5(a) and (b) show the impact of the metal thickness w_z on the real part of the characteristic impedance for different values of the width w_y. As expected, the values of Z_0 increase by reducing the width w_y and the metal thickness w_z. The impact of w_z on the characteristic impedance is larger when it starts to be comparable with w_y, producing a variation of the 12% for $w_y = 5\,\mu\text{m}$ for the minimum considered thickness. The results produced with the method presented here are compared with the ones obtained with [165], which does not consider the thickness w_z. The results are also compared with the ones obtained using the commercial tool Sonnet [153]. In both cases, there is a fair agreement.

As a further validation of the accuracy of the presented method, we compare in Fig. 6.6 our method with the measurements and the simulations of [174], which presents the state-of-the-art numerical tool [153] for modeling microstrip lines and their losses. The line has a length of 6.888 mm, a width $w_y = 51\,\mu\text{m}$ and a thickness $w_z = 7\,\mu\text{m}$, it is constituted by a material of $\sigma = 3.45 \times 10^7\,\text{S/m}$ printed at the interface between two dielectrics having permittivity 12.9 and 3.2, and thickness 75 µm and 16 µm, respectively. The comparison shows an excellent agreement between the measurements and the two simulations. However, the minor differences between the spectral domain method and the numerical solution of [174] could be attributed to how the currents are modeled over the cross-section. In fact, in [174], the current in the microstrip is divided into 81 layers along z, and 128 cells along y, while for the method here proposed, we resort to (6.15) and (6.26), which allows us to derive a semi-analytical solution.

Our method is also tested with the conductor losses of [175, 176] obtained with the concept of the quasi-transverse electromagnetic surface impedance. In Fig. 6.7(a) we reproduce [175, Fig. 7], which shows the attenuation constant of a microstrip at 9 GHz versus the aspect ratio w_y/w_z for a thickness $w_z = 1.524\,\mu\text{m}$ and conductivity $\sigma = 4 \times 10^7\,\text{S/m}$, when printed on a dielectric having a permittivity $\varepsilon_r = 11$ and thickness $h = 254\,\mu\text{m}$. The results of [175] are in better agreement with the ones obtained with the commercial tools HFSS and ADS. However, the present tool allows for a better agreement with both the reference tools for small aspect ratios, i.e., $w_y/w_z \approx 1$, which is the condition where [175] commits the largest error. In Fig. 6.7(b), we reproduce [175, Fig. 6] by showing the attenuation constant versus the frequency for a microstrip of thickness $w_z = 6\,\mu\text{m}$, width $w_y = 152.4\,\mu\text{m}$, and a conductivity $\sigma = 4 \times 10^7\,\text{S/m}$, when printed on a substrate of thickness $h = w_y/2$ and permittivity $\varepsilon_r = 11$. The results obtained by [175] are in better agreement with the reference tools than the spectral domain, which is superimposed with [176].

The impact of the conductivity σ on the characteristic impedance is investigated in Fig. 6.8, where the characteristic impedance Z_0 and the attenuation constant α are studied at 300 GHz for different widths and thicknesses of the microstrip when it is printed on a dielectric of permittivity $\varepsilon_r = 4.3$ and thickness $h = 10\,\mu\text{m}$. As shown in

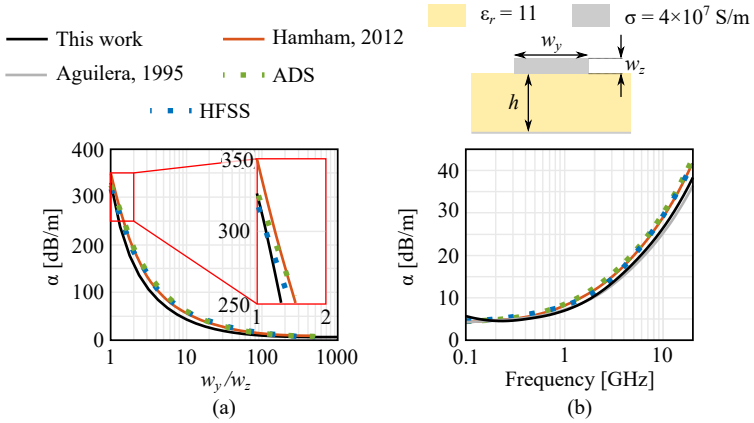

Figure 6.7: (a) Conductor losses versus the aspect ratio of the metal at 9 GHz, for a microstrip of thickness $w_z = 1.524\,\mu\text{m}$, conductivity $\sigma = 4 \times 10^7$ S/m, when printed on a dielectric having a permittivity $\varepsilon_r = 11$ and thickness $h = 254\,\mu\text{m}$, (b) Conductor losses versus the frequency for a microstrip of thickness $w_z = 6\,\mu\text{m}$, width $w_y = 152.4\,\mu\text{m}$, and a conductivity $\sigma = 4 \times 10^7$ S/m, when printed on a substrate of thickness $h = w_y/2$ and permittivity $\varepsilon_r = 11$.

Fig. 6.8(a), the real part of the characteristic impedance depends mainly on the width of the line w_y, and, for smaller values of σ, also this latter and w_z starts to have an impact. The imaginary part of Z_0 is shown in Fig. 6.8(b), exhibiting large negative values, i.e., high losses for smaller values of σ. The attenuation constant α is shown in Fig. 6.8(c). In good conductors α is mainly due to σ and w_y, and weakly dependent on w_z. Instead, for low values of σ, also the metal thickness plays an important role in the attenuation constant. It is worth mentioning that, as previously stated the results are affected by the penetration depth [see Fig. 6.8(d)] becoming comparable with the other dimensions in the geometry.

6.3.3. Printed Leaky Dipoles

As a final example, we consider the case of a dipole printed between free space and a dielectric half-space. In this case, the propagation is much more dispersive with respect to frequency due to the excitation of a dominant leaky wave. The dispersion can be appreciated by looking at the characteristic impedance in Fig. 6.9(a), where the significant imaginary part indicates the radiation losses. The real part of the effective propagation constant is shown in Fig. 6.9(b), where it is noticeable that the predictions of the present tool associate a significant impact to the thickness of the metal, which is disregarded in the tool in [165, 166]. Finally, the attenuation versus

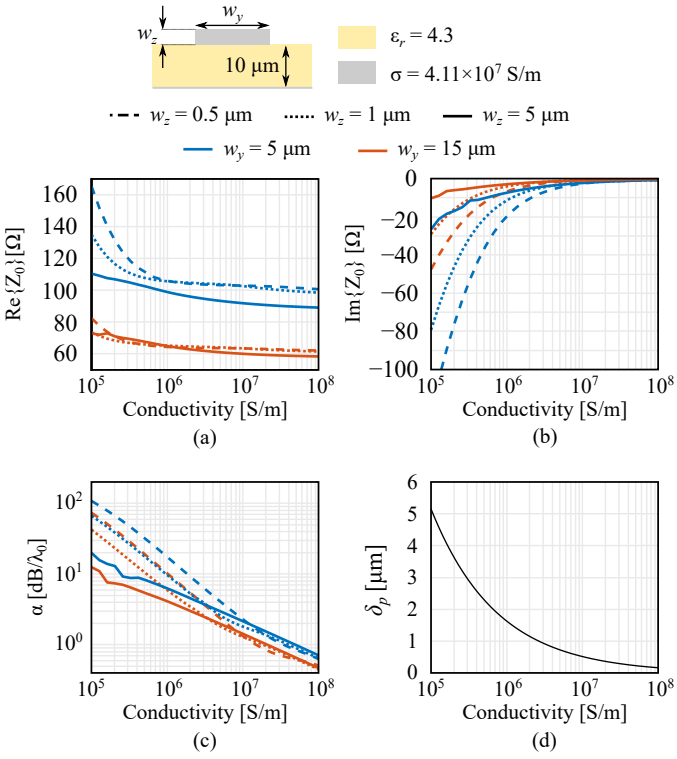

Figure 6.8: (a) Real and (b) imaginary part of the characteristic impedance, and (c) attenuation constant versus the metal conductivity calculated at 300 GHz, for a microstrip of width w_y and w_z thick printed on a dielectric $h = 10\,\mu$m thick and having dielectric permittivity $\varepsilon_r = 4.3$. (d) Penetration depth versus the conductivity calculated at 300 GHz.

the frequency is shown in Fig. 6.9(c) and 6.9(d). The radiation-induced losses are clearly the main cause of the attenuation, as shown in Fig. 6.9(d).

As it can be seen in Fig. 6.9(b), the effective permittivity decreases when increasing the metal thickness, as a larger share of the current is located in free space. However, the effective permittivity depends on the average between the permittivities of the dielectrics above and below the dipole. Therefore, the propagation along a thick metal dipole can be equivalently reproduced on a planar line located between one of the two original dielectrics and a less dense one. As an example, in Fig. 6.10, the permittivity of the dipoles of Fig. 6.9 are synthesized using [165] by decreasing the permittivity of the dielectric from $\varepsilon_r = 4.3$ to $\varepsilon_r = 4.05$, $\varepsilon_r = 3.97$, and $\varepsilon_r = 3.65$ to obtain the same effective permittivity of $w_z = 0.5\,\mu$m, $w_z = 1\,\mu$m, and $w_z = 5\,\mu$m, respectively. The bandwidth in which the synthesis is valid decreases with the metal thickness.

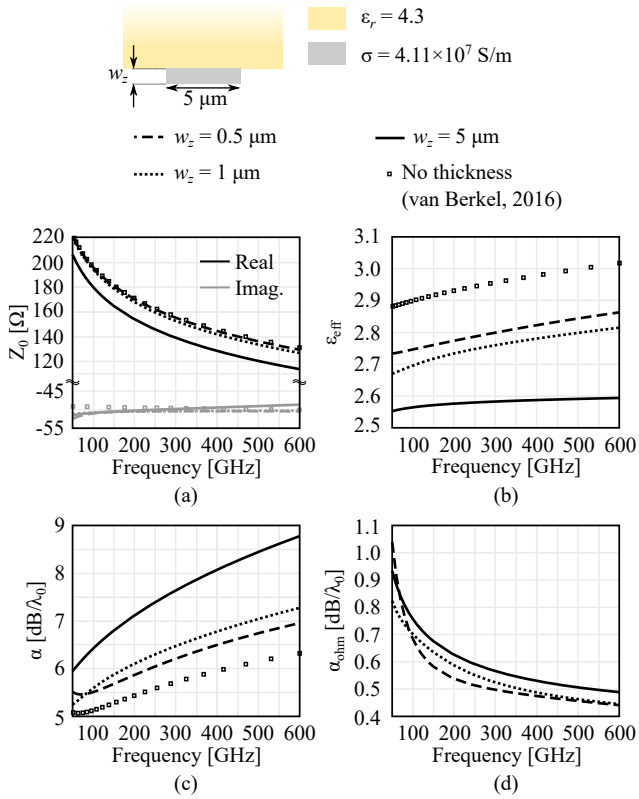

Figure 6.9: (a) Characteristic impedance, (b) effective permittivity, (c) total attenuation constant, and (d) attenuation constant of the ohmic losses associated with a leaky mode supported on a dipole constituted by a metal of conductivity $\sigma = 4.11 \times 10^7$ S/m, width $w_y = 5$ µm and thickness w_z, and printed on a semi-infinite dielectric medium of permittivity $\varepsilon_r = 4.3$.

6.4. Transmission Line Equivalent Circuit

Once the transmission line Green's function is validated, it is useful to look at the dominant spectral components of the current, highlighting the impact of the low and high parts of the spectrum. These are then used to derive an equivalent circuit that represents the input impedance of a Δ-gap fed dipole.

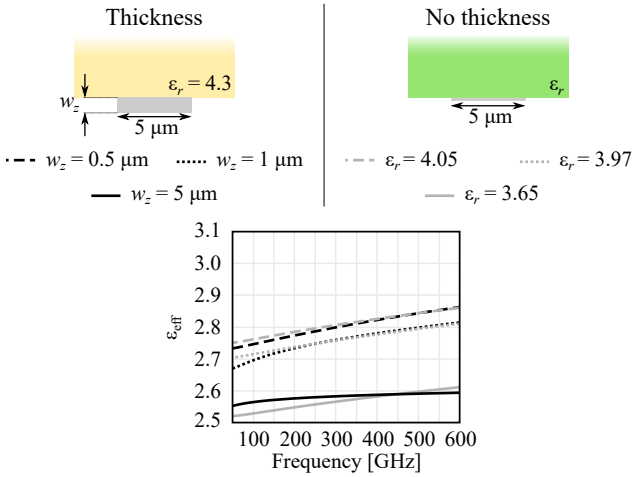

Figure 6.10: Synthesis of the effective permittivity in dipoles with nonzero metal thickness by using planar dipoles printed on a different medium.

6.4.1. Spectral Components of the Current

In the case of a dominant pole, the current spectrum (6.13) can be approximated around the pole k_{xp} with its Laurent expansion. This constitutes the dynamic component of the current I_{dyn}, which is expressed as follows

$$I(k_x) \approx I_{\text{dyn}}(k_x) = \frac{2k_{xp}\,\text{sinc}(k_x\Delta/2)}{D'(k_{xp})\left(k_x^2 - k_{xp}^2\right)} \text{ for } k_x \to k_{xp}. \tag{6.31}$$

By performing analytically the inverse Fourier transform of (6.31), the dynamic current component can be written, outside the feeding gap, as the following travelling wave

$$i_{\text{dyn}}\left(|x| > \Delta/2\right) = -j\frac{\text{sinc}(k_{xp}\Delta/2)}{D'(k_{xp})}e^{-jk_{xp}|x|} \tag{6.32}$$

and inside the gap as the following standing wave

$$i_{\text{dyn}}\left(|x| < \Delta/2\right) = 2\frac{1-\cos(k_{xp}x)e^{-jk_{xp}\Delta/2}}{\Delta k_{xp}D'(k_{xp})}. \tag{6.33}$$

In Fig. 6.11, the dynamic current is compared with the total current at $f = 300\,\text{GHz}$ in a dipole constituted by a metal with conductivity $\sigma = 4.11 \times 10^7\,\text{S/m}$ of width $w_y = 30\,\mu\text{m}$, and printed on a grounded dielectric slab with permittivity $\varepsilon_r = 4.3$ and thickness $d = 10\,\mu\text{m}$ for two values of the gap-size Δ and the metal thickness w_z.

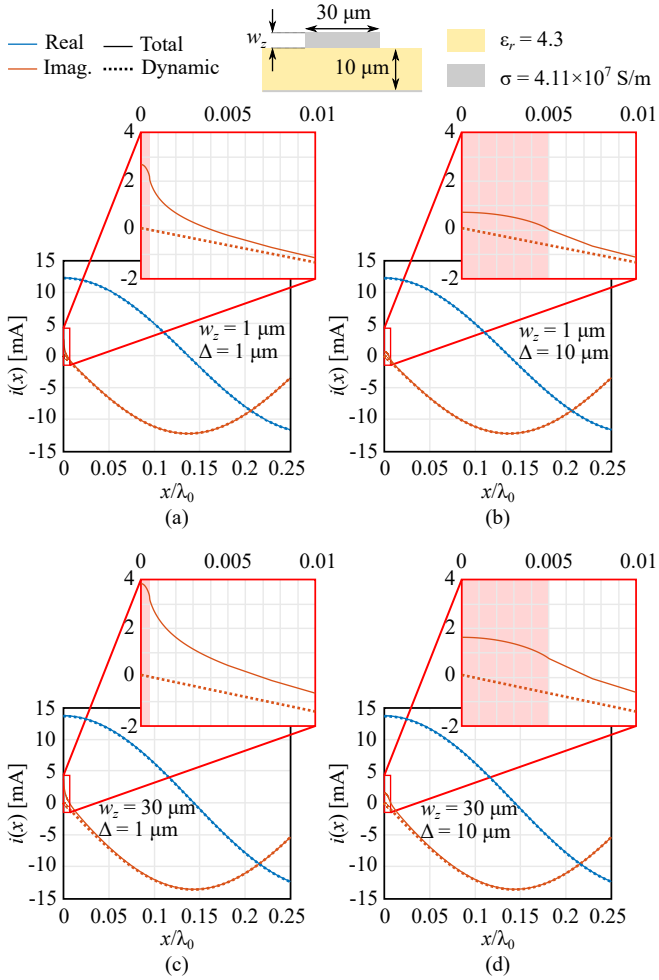

Figure 6.11: Comparison between the total and the dynamic current at $f = 300\,\text{GHz}$ in a dipole constituted by a metal with conductivity $\sigma = 4.11 \times 10^7\,\text{S/m}$ and width $w_y = 30\,\mu\text{m}$, and printed on a grounded dielectric slab with permittivity $\varepsilon_r = 4.3$ and thickness $d = 10\,\mu\text{m}$ for (a) $\Delta = 1\,\mu\text{m}$ and $w_z = 1\,\mu\text{m}$, (b) $\Delta = 10\,\mu\text{m}$ and $w_z = 1\,\mu\text{m}$, (c) $\Delta = 1\,\mu\text{m}$ and $w_z = 30\,\mu\text{m}$, and (d) $\Delta = 10\,\mu\text{m}$ and $w_z = 30\,\mu\text{m}$. The gap is highlighted in the red-shaded areas in the insets.

Inside and outside the gap area, the dynamic current is associated with variations dominated by the wavenumber k_{xp}. If away from the gap, the total and the dynamic currents are superimposed, close to the gap, the imaginary part of the current is significantly different from the dynamic one, especially for smaller gap sizes. This

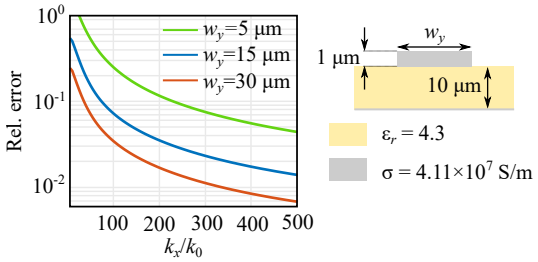

Figure 6.12: Relative error between D and D_∞ versus k_x calculated for different values of w_y for a dipole constituted by a metal with conductivity $\sigma = 4.11 \times 10^7$ S/m of thickness $w_z = 1\,\mu$m, and printed on a grounded dielectric slab with permittivity $\varepsilon_r = 4.3$ and thickness $d = 10\,\mu$m.

has to be imputed to the current's high-spectrum component, which is not taken into account in (6.31) and becomes more important when decreasing the gap size.

The quasi-static component of I, i.e., for $k_x \to \infty$, can be approximated by an asymptotic expression for D, as shown in Appendix E.2, which yields to the following expression

$$D(k_x) \approx D_\infty(k_x) = \rho\langle j_t, \tilde{j}_t\rangle_A - \frac{J_{t,y}(0)}{w_y}\int_0^{w_z}\int_0^{w_z}\left[G_{xx}^{EJ}(k_x,0,z,z')\,j_{t,z}(z')\,j_{t,z}(z)\right]dzdz'$$

$$\text{for } k_x \to \infty. \quad (6.34)$$

In Fig. 6.12, the relative error between D and D_∞, i.e., $|D - D_\infty|/|D|$ is shown versus k_x for different values of the width w_y. The convergence rate increases with w_y, as for smaller values, the decay in (E.13) is slower.

6.4.2. Dynamic Admittance

Once the nature of the current is established, it suggests deriving the equivalent circuit for the input impedance of a delta gap fed dipole. The ideas are similar to those discussed in [44, 164, 171, 177, 178]. With respect to the cited cases, the presentation here allows us to highlight the impact of the metal thickness. The equivalent circuit is shown in Fig. 6.13, and all its components will be discussed in this section.

The admittance associated with the dynamic component of the current can be calculated with the following integral in the k_x complex plane extending to the dipoles

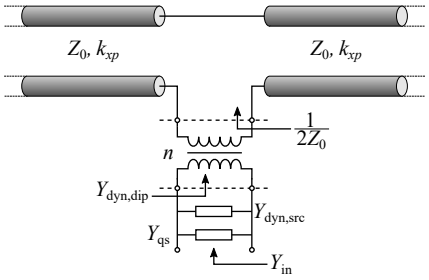

Figure 6.13: Transmission line equivalent circuit of an infinitely long dipole, represented by two transmission line sections placed in series and connected to a transformer, constituting $Y_{\text{dyn,dip}}$, and $Y_{\text{dyn,src}}$ and Y_{qs} placed in parallel.

the procedure presented for the slots in [177]

$$Y_{\text{dyn}} = -\frac{1}{2\pi}\int_{-\infty}^{+\infty} \frac{2k_{xp}\,\text{sinc}^2\left(k_x\Delta/2\right)}{D'(k_{xp})\left(k_x^2 - k_{xp}^2\right)}dk_x \tag{6.35}$$

whose solution is written as follows

$$Y_{\text{dyn}} = Y_{\text{dyn,dip}} + Y_{\text{dyn,src}} \tag{6.36}$$

where $Y_{\text{dyn,dip}}$ is associated with the propagation along the dipole and expressed as

$$Y_{\text{dyn,dip}} = -\frac{j}{D'(k_{xp})}\,\text{sinc}^2\left(\frac{k_{xp}\Delta}{2}\right) = \frac{1}{2Z_0}n^2 \tag{6.37}$$

and $Y_{\text{dyn,src}}$ is associated with the standing wave confined inside the source and calculated with the following analytical expression

$$Y_{\text{dyn,src}} = \frac{2(\text{sinc}\left(k_{xp}\Delta\right) - 1)}{\Delta k_{xp} D'(k_{xp})}. \tag{6.38}$$

Then one can derive the transmission line equivalent circuit shown in Fig. 6.13, where two transmission line sections of characteristic impedance Z_0 are connected in series to a transformer of turn ratio n, and placed in parallel with $Y_{\text{dyn,src}}$. The dynamic admittance Y_{dyn} represents only the admittance associated with modal current waves traveling along the dipole with propagation constant k_{xp}, while the quasi-static effect of the gap has to be separately taken into account. This corresponds to the opportune modeling of the fast-varying current in the gap area, that were highlighted in the insets of Fig. 6.11.

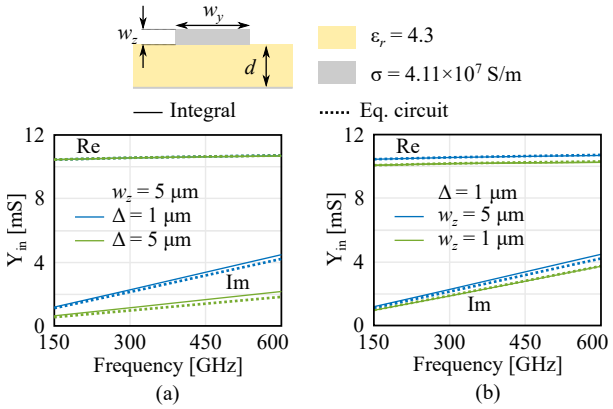

Figure 6.14: Comparison of the input admittance calculated with the full spectral integral and with the equivalent circuit of a dipole constituted by a metal with conductivity $\sigma = 4.11 \times 10^7$ S/m and width $w_y = 20\,\mu$m, and printed on a grounded dielectric slab with permittivity $\varepsilon_r = 4.3$, and thickness $d = 10\,\mu$m for (a) a fixed value of the metal thickness and different gap lengths, and (b) a fixed gap length and different metal thicknesses.

6.4.3. Quasi-Static Admittance

One can define the quasi static admittance by using the following expression

$$Y_{\text{qs}} = \frac{1}{2\pi}\int_{-\infty}^{+\infty} \frac{\text{sinc}^2(k_x\Delta/2) - \text{sinc}^2(k_x\Delta_{\text{large}}/2)}{D_\infty(k_x)}\,dk_x \tag{6.39}$$

where Δ_{large} is a feeding gap much larger than Δ, typically in the order of $\lambda_0/10$. The admittance Y_{qs} represents the reactance associated with the capacitive effect given by the fields fringing around the feeding gap. The numerator of (6.39) isolates the capacitance of the gap of size Δ. In fact, the subtraction operates as a filter that removes the low part of the spectrum, while the quasi-static component is left untouched as this component is negligible for Δ_{large}. As shown in Fig. 6.11, the impact of the quasi-static component of the current increases when decreasing the gap size or increasing the metal thickness, as these two parameters increase the gap capacitance. The definition of the quasi-static admittance Y_{qs} allows us to derive the transmission line equivalent circuit shown in Fig. 6.13, where Y_{qs} is placed in parallel with Y_{dyn}.

While the concept of the dynamic admittance is meaningful only in the presence of a dominant polar contribution (e.g., in a mictrostrip), the quasi-static component can always be defined.

In Fig. 6.14, the input admittance of a dipole obtained by integrating (6.13) on the gap is compared to the one calculated with its transmission line equivalent circuit. The dipole is constituted by a metal having a conductivity $\sigma = 4.11 \times 10^7\,\mathrm{S/m}$ and width $w_y = 20\,\mu\mathrm{m}$, and it is printed on a grounded dielectric slab having permittivity $\varepsilon_r = 4.3$, and thickness $d = 10\,\mu\mathrm{m}$. In Fig. 6.14(a) the input admittance is calculated for a metal thickness $w_z = 5\,\mu\mathrm{m}$ and for the length of the feeding port $\Delta = 1\,\mu\mathrm{m}$ and $\Delta = 5\,\mu\mathrm{m}$. For every value of Δ, there is an excellent agreement between the values obtained with the full integration and those obtained with the equivalent circuit. Moreover, one can recognize the effect of the shunt capacitance associated with the gap, as the imaginary part increases when decreasing Δ, leaving the real part unaffected. In Fig. 6.14(b) in turn, the input admittance is studied for $\Delta = 1\,\mu\mathrm{m}$, for different values of the metal thickness. This latter affects both the real and the imaginary part, as it impacts both the characteristic impedance of the line and the capacitance of the feeding gap.

6.5. Conclusion

In this chapter we have derived a TL GF formalism to model dipoles with nonzero metal thickness. Thanks to the spectral domain formalism, the procedure can be used to efficiently analyse dipoles embedded in an arbitrary stratification, and allowing the analysis of microstrips and dipoles printed at the interface of two media radiating leaky waves. By comparison with state-of-the-art numerical techniques, up-to-par performances are shown. Finally, a transmission line equivalent circuit is derived, allowing for a deep physical insight on the propagation mechanism along the dipole, and on the effect of the feeding gap.

Chapter 7

The Analysis of Nonzero Thickness Dipoles of Finite Length

Interesting occupations are essential to happiness. Indeed, the whole art of being happy consists in the art of finding employment.
–Thomas Jefferson

7.1. Introduction

The study of the radiation from electrical dipoles has laid the foundations of computational electromagnetics [179, 180], but still remains a problem of interest [181–183]. The issue has been investigated both in the spatial [179–184] and in the spectral domain [185–188], often recurring to the *thin* dipole approximation or neglecting the impact of the metal thickness. With the introduction of the transmission line Green's function (TL GF) [157, 159, 189], such analysis can be performed semi-analytically in the spectral domain with a reduced set of unknowns as in [164, 171]. However, these do not account for the metal thickness, which in the sub-millimeter wave regime can be comparable with the other dimensions in play. In [190] and [191], for the dual problem of the slots, the impact of the thickness of the metal screen is investigated, and showing an impact even for metallizations in the order of one-thirtieth of the wavelength. In Chapter 6, the TL GF, including for the metal thickness, was derived for an infinitely long dipole. This chapter aims to extend the formulation of Chapter 6 with techniques similar to [164, 171] to analyze finite dipoles with nonzero metal thickness and to study their input impedance and radiation patterns.

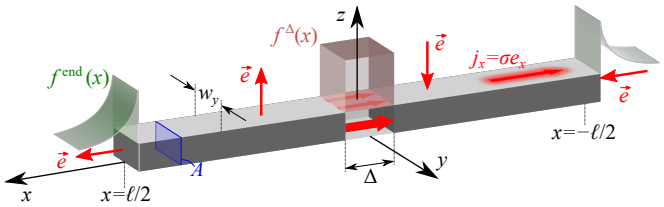

Figure 7.1: Sketch of a dipole of length ℓ, width w_y, and thickness w_z, and the representation of the longitudinal distributions on the gap and after the end points.

7.2. Formulation

7.2.1. The Integral Equation and the Current Spectrum

Let us consider a dipole oriented along the x-axis, embedded in arbitrary stratified media, and constituted by a material of conductivity σ (or equivalently resistivity $\rho = 1/\sigma$), as shown in Fig. 6.1. It is fed with a voltage V_0 by a Δ-gap generator Δ long located at its center. The dipole has a cross section A, it is w_y wide and w_z thick, and it is located between $x = -\ell/2$ and $x = \ell/2$. Due to its elongated geometry and the rectangular cross-section, only the x-component of the electric field is considered, and this can be written as the product of a longitudinal and a transverse function. The x-component of the incident field e_x^i can be written as follows

$$e_x^i(x, y, z) = V_0 f^{\Delta}(x)\, e_t(y, z) \tag{7.1}$$

where f^{Δ} and e_t are the excitation's longitudinal and transverse distributions. The x-component of the total electric field e_x can be expressed, for every x, and for $(y, z) \in A$, by resorting to the local form of Ohm's law as follows

$$e_x(x, y, z) = \rho i(x)\, j_t(y, z)\, \chi_{\text{dip}}(x) + V_{\text{end}} f^{\text{end}}(x)\, e_t(y, z) \tag{7.2}$$

where i is the longitudinal current distribution along the dipole, j_t is the transverse current distribution, and χ_{dip} is the characteristic function of the dipole (i.e., $\chi_{\text{dip}} = 1$ for x located in the dipole, and $\chi_{\text{dip}} = 0$ elsewhere). While the first term in (7.2) models the field in the dipole by means of the local form of Ohm's law, the second one models the field beyond the endpoints. As sketched in Fig. 6.1, this latter uses the decaying function f^{end}, as in [164, 171], having amplitude V_{end} at $x = \pm\ell/2$ due to the symmetrical excitation.

$$e_x^s(x, y, z) = g_{xx}^{EJ}(x, y, z, z') * [i(x)\, \chi_{\text{dip}}(x)\, j_t(y, z)] \tag{7.3}$$

where g_{xx}^{EJ} is the xx-component of the Green's function providing the electric field from the electric sources located at z', and $*$ denotes the convolution operator in x

and y. Finally, by imposing $e_x = e_x^i + e_x^s$, one can set the following integral equation for every x

$$V_0 f^{\Delta}(x)\, e_t(y,z) - V_{\text{end}} f^{\text{end}}(x)\, e_t(y,z) = \big(\rho\,\delta(x,y,z) - g_{xx}^{EJ}\,(x,y,z,z')\big) * [i(x)\,\chi_{\text{dip}}(x)\,j_t(y,z)] \quad (7.4)$$

where δ is the Dirac delta. By applying the inner product (6.11) to (7.4) and $\tilde{j}_t(y,z)$, the following expression is obtained

$$V_0 f^{\Delta}(x)\,\langle e_t, \tilde{j}_t\rangle_A - V_{\text{end}} f^{\text{end}}(x)\,\langle e_t, \tilde{j}_t\rangle_A = \langle \big(\rho\,\delta(x,y,z) - g_{xx}^{EJ}\,(x,y,z,z')\big) * [i(x)\,\chi_{\text{dip}}(x)\,j_t(y,z)], \tilde{j}_t\rangle_A. \quad (7.5)$$

where e_t can be assumed to be normalized such that $\langle e_t, \tilde{j}_t\rangle_A = 1$. The right-hand side of (7.5) can be written as follows

$$\iint_A \big(\rho\,\delta(x,y,z) - g_{xx}^{EJ}(x,y,z,z')\big) * [i(x)\,\chi_{\text{dip}}(x)\,j_t(y,z)] \times \tilde{j}_t^*(y,z)\,dydz. \quad (7.6)$$

By explicating the convolution integrals of (7.6), the following expression is obtained

$$\iint_A \Big[\int_{-\infty}^{+\infty} \iint_A \big(\rho\,\delta(x-x', y-y', z-z') - g_{xx}^{EJ}(x-x', y-y', z, z')\big)\, i(x')\,\chi_{\text{dip}}(x') \times j_t(y', z')\,dy'dz'dx'\Big] \tilde{j}_t^*(y,z)\,dydz \quad (7.7)$$

where in the square brackets the single integral from $-\infty$ to $+\infty$ is performed over dx', and the integrals on the cross section A are performed over dy' and dz'. By interchanging the integration order of dx' and $dydz$, and by calculating the integrals for the Dirac delta, the following expression is found

$$\int_{-\infty}^{+\infty} \Big\{ \rho\,\delta(x-x')\,\langle j_t, \tilde{j}_t\rangle_A - \iint_A \Big[\iint_A g_{xx}^{EJ}(x-x', y-y', z, z')\, j_t(y', z')\,dy'dz'\Big] \times \tilde{j}_t(y,z)\,dydz \Big\} i\,(x')\,\chi_{\text{dip}}(x')\,dx' \quad (7.8)$$

The terms in curly brackets in (7.8) allow us to define the transverse Green's function of the dipole $d\,(x)$ as follows

$$d\,(x) = \rho\,\delta(x)\,\langle j_t, \tilde{j}_t\rangle_A - \iint_A \Big[\iint_A g_{xx}^{EJ}(x, y-y', z, z')\, j_t(y', z')\,dy'dz'\Big] \times \tilde{j}_t(y,z)\,dydz. \quad (7.9)$$

With the introduction of the transverse Green's function (7.9), (7.5) is written as follows

$$V_0 f^{\Delta}(x)\,\langle e_t, \tilde{j}_t\rangle_A - V_{\text{end}} f^{\text{end}}(x)\,\langle e_t, \tilde{j}_t\rangle_A = \int_{-\infty}^{+\infty} d(x-x')\,i(x')\,\chi_{\text{dip}}(x')\,dx'. \quad (7.10)$$

By performing the Fourier transform of (7.10) with respect to x, one can write the following expression

$$V_0 F^{\Delta}(k_x)\,\langle e_t, \tilde{j}_t\rangle_A - V_{\text{end}} F^{\text{end}}(k_x)\,\langle e_t, \tilde{j}_t\rangle_A = D(k_x)\,X_{\text{dip}}(k_x) * I(k_x) \quad (7.11)$$

where F^{Δ}, I, X_{dip}, F^{end}, and D are the Fourier transforms of f^{Δ}, i, χ_{dip}, f^{end}, and d, respectively. By assuming that e_t has a unitary integral on the cross-section, i.e., $\langle e_t, \tilde{j}_t\rangle_A = 1$, the spectrum of the current can be finally written as follows

$$X_{\text{dip}}(k_x) * I(k_x) = \frac{V_0 F^{\Delta}(k_x) - V_{\text{end}} F^{\text{end}}(k_x)}{D(k_x)}. \quad (7.12)$$

7.2.2. Field Representation

The modeling of the incident field and of the transverse current distribution are congruent with those of (6.2), (6.3), (6.15), and (6.26), allowing to calculate the transverse Green's function with the procedures of (6.14). These use the spectral domain Green's function, which allows the efficient handling of dipoles in layered media.

For the sake of simplicity, field distribution f^{Δ} outside the dipole is assumed to have the following exponential behavior

$$f^{\text{end}}(x) = \frac{1}{2c}\left(e^{-\frac{x-\ell/2}{c}}\,u\,(x-\ell/2) + e^{\frac{x+\ell/2}{c}}\,u\,(-x-\ell/2)\right) \quad (7.13)$$

with u being the unitary step function and c the decay rate, whose value has been determined empirically from CST simulations. For dipoles in free space or located between free space and a low permittivity dielectric, $c = \lambda_0/40$ (where λ_0 is the free-space wavelength at each operating frequency) provides accurate results regardless of the specific geometry. In the case of an high permittivity dielectric, f^{end} requires a faster decay rate than $\lambda_0/40$, due to the smaller confinement of the field. The use of CST has been limited to find empirically the best value of c. Once the value has been determined, it is used in the spectral domain model, independently of CST. The sensitivity of the results with respect to c and the geometry is discussed in Section 7.3.1.

$$F^{\text{end}}(k_x) = \frac{1}{2}\left(\frac{e^{-jk_x\ell/2}}{1+jk_xc} + \frac{e^{jk_x\ell/2}}{1-jk_xc}\right). \quad (7.14)$$

which is used to calculate the current spectrum with (7.12).

7.2.3. The Method of Moments Solution

The spectrum (7.12) has only been formally defined, as the weight V_{end}, given the excitation V_0, has still to be determined to calculate the current spectrum of each specific problem. The current distribution i can be obtained from (7.12) with the following inverse Fourier transform

$$i(x)\,\chi_{\text{dip}}(x) = \frac{1}{2\pi}\int_{-\infty}^{+\infty} [X_{\text{dip}}(k_x) * I(k_x)]\, e^{-jk_x x} dk_x = \frac{1}{2\pi}\int_{-\infty}^{+\infty} \frac{V_0 F^{\Delta}(k_x) - V_{\text{end}} F^{\text{end}}(k_x)}{D(k_x)} e^{-jk_x x} dk_x. \quad (7.15)$$

By calculating the inner product between (7.15) and a test function $t(x)$, the following expression is derived

$$\int_{-\infty}^{+\infty} \frac{1}{2\pi}\int_{-\infty}^{+\infty} [X_{\text{dip}}(k_x) * I(k_x)] e^{-jk_x x} dk_x t^*(x)\, dx = \int_{-\infty}^{+\infty} \frac{1}{2\pi}\int_{-\infty}^{+\infty} \frac{V_0 F^{\Delta}(k_x) - V_{\text{end}} F^{\text{end}}(k_x)}{D(k_x)} e^{-jk_x x} dk_x t^*(x) dx. \quad (7.16)$$

By interchanging the integration order in (7.16), the Fourier transform of t^* can be calculated as follows

$$\frac{1}{2\pi}\int_{-\infty}^{+\infty} [X_{\text{dip}}(k_x) * I(k_x)]\, T(-k_x)\, dk_x = V_0 \left[\frac{1}{2\pi}\int_{-\infty}^{+\infty} \frac{F^{\Delta}(k_x)\, T(-k_x)}{D(k_x)} dk_x\right] - V_{\text{end}} \left[\frac{1}{2\pi}\int_{-\infty}^{+\infty} \frac{F^{\text{end}}(k_x)\, T(-k_x)}{D(k_x)} dk_x\right] \quad (7.17)$$

where T is the Fourier transform of t. By considering t either f^{Δ} or f^{end}, the following two-unknown linear system can be obtained

$$\begin{cases} V_0\, Y_{\Delta,\Delta} - V_{\text{end}}\, Y_{\Delta,\text{end}} = I_0 \\ V_0\, Y_{\Delta,\text{end}} - V_{\text{end}}\, Y_{\text{end,end}} = I_{\text{end}} \end{cases} \quad (7.18)$$

where I_0 and I_{end} are the average currents on the gap and on the space after the dipole terminations. The admittances are defined as follows

$$Y_{m,n} = \frac{1}{2\pi}\int_{-\infty}^{+\infty} \frac{F^m(k_x)\, F^n(-k_x)}{D(k_x)} dk_x \quad (7.19)$$

with m and n being either 'Δ' or 'end'. After having imposed an open-circuit condition outside the dipole, i.e., $I_{\text{end}} = 0$, I_0 and V_{end} can be calculated analytically as follows

$$V_{\text{end}} = V_0 \frac{Y_{\Delta\text{end}}}{Y_{\text{end,end}}} \tag{7.20}$$

$$I_0 = V_0 \left(Y_{\Delta\Delta} - \frac{Y_{\Delta,\text{end}}^2}{Y_{\text{end,end}}} \right). \tag{7.21}$$

The expression of V_{end} can be used to calculate the current spectrum (7.12), and I_0 can be used to calculate the input impedance from its definition as follows

$$Z_{\text{in}} = \frac{V_0}{I_0} = \frac{Y_{\text{end,end}}}{Y_{\Delta\Delta} Y_{\text{end,end}} - Y_{\Delta,\text{end}}^2}. \tag{7.22}$$

7.3. Validation and Results

The spectral domain formulation allows the efficient analysis of dipoles with cross-sections and feeding gaps that are small in terms of the dimensions of the surrounding dielectrics. Within this work, we present the validation and the results, in terms of the input impedance, the current distribution, and the far-field patterns.

7.3.1. Input Impedance

The input impedance is calculated using (7.22), and an example is shown in Fig. 7.2(a) and (b), where a good agreement with CST is obtained. However, when the capacitance of the gap becomes significant, i.e., the cross-section is much larger than the feeding gap, the present method starts to be inaccurate at high frequencies. In fact, the capacitance of the gap is underestimated in $Y_{\Delta,\Delta}$ as the transverse current distribution $j_t(y, z)$, instead of being uniform, is significant only on the top and bottom part of the two faces of the feeding gap, as shown in Fig. 7.3. Therefore, an additional parallel capacitance is used to compensate for this effect. This can be approximated with $C = \varepsilon_0 \varepsilon_{\text{eff}} w_y w_z / \Delta$. This compensation is significant in Fig. 7.2(c), where it improves the comparison with CST.

The low frequency reactance depends on the endpoints located at $x = \pm \ell/2$, and it is associated with the electric field going from one arm of the dipole to the other. This behavior is known to be asymptotic to the open circuit approximation $-jZ_0 \cot(k_{xp}\ell/2)$, where Z_0 and k_{xp} are the characteristic impedance and the propagation constant, respectively, of the line 6. As it can be seen in Fig. 7.2, for either the

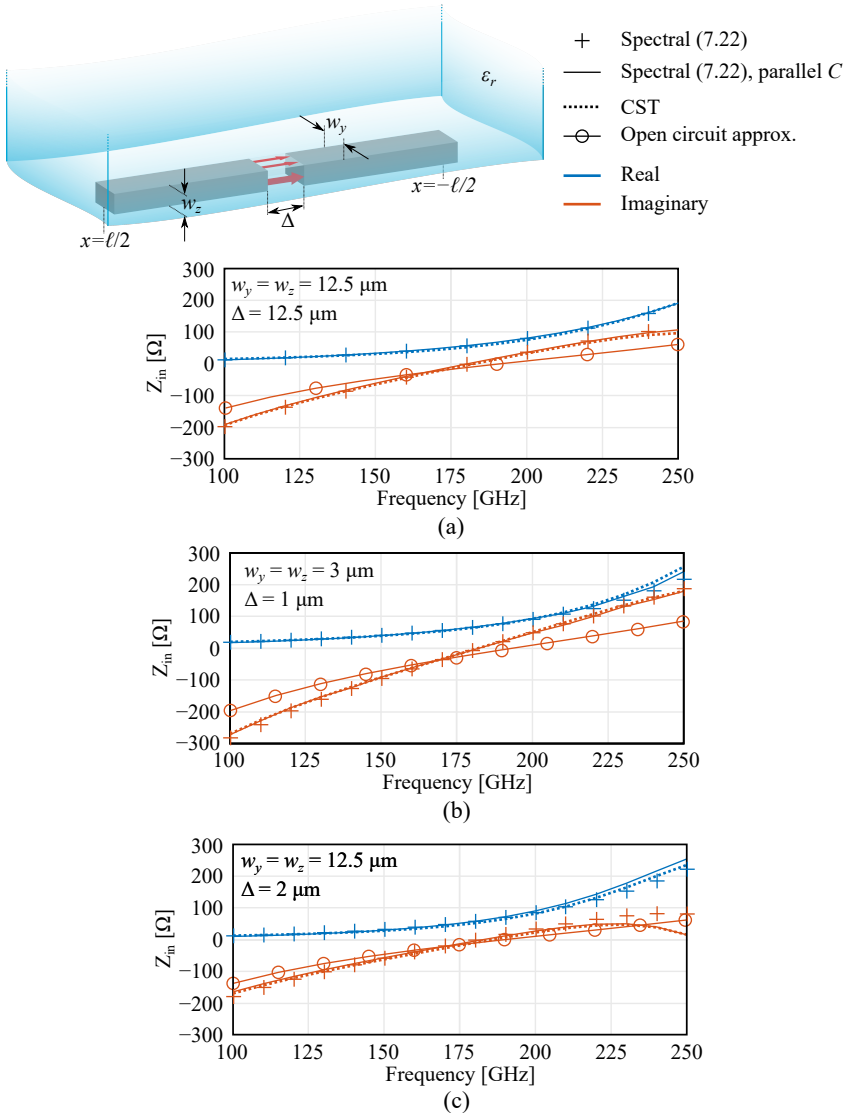

Figure 7.2: Input impedance of a dipole having length $\ell = 500\,\mu\text{m}$, constituted by a metal having conductivity $\sigma = 10^7$ S/m and printed between free space an a semi-infinite dielectric with relative permittivity $\varepsilon_r = 4$ calculated for (a) $w_y = w_z = \Delta = 12.5\,\mu\text{m}$, (b) $w_y = w_z = 3\,\mu\text{m}$ and $\Delta = 1\,\mu\text{m}$, and (c) $w_y = w_z = 12.5\,\mu\text{m}$ and $\Delta = 2\,\mu\text{m}$. The decay rate $c = \lambda_0/40$ has been used.

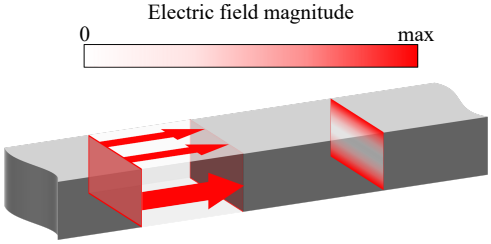

Figure 7.3: Sketch of the magnitude of the electric field distribution along the dipole and in the feeding gap.

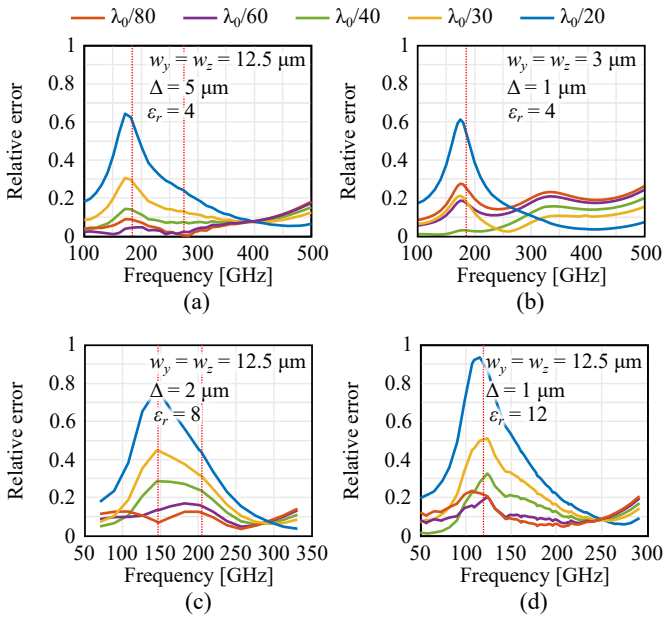

Figure 7.4: The relative error of the input impedance calculated with respect to CST for different values of the decay rate c for a dipole $\ell = 500\,\mu\text{m}$ long, having a feeding gap Δ long, w_y wide and w_z thick, and printed between free space and dielectric half space with permittivity ε_r. (a) $w_y = w_z = 12.5\,\mu\text{m}$, $\Delta = 5\,\mu\text{m}$, $\varepsilon_r = 4$, (b) $w_y = w_z = 3\,\mu\text{m}$, $\Delta = 1\,\mu\text{m}$, $\varepsilon_r = 4$,(c) $w_y = w_z = 12.5\,\mu\text{m}$, $\Delta = 2\,\mu\text{m}$, $\varepsilon_r = 8$, and (d) $w_y = w_z = 12.5\,\mu\text{m}$, $\Delta = 1\,\mu\text{m}$, $\varepsilon_r = 12$. The red dashed lines highlight the frequencies for which the imaginary part of the input impedance is null.

complete solution and the open circuit approximation, the slope of the imaginary part depends on the size of the cross section, as the characteristic impedance Z_0 increases for decreasing values of the cross section, 6.

Table 7.1: Solution time for the input impedance of Fig. 7.2 calculated over 16 frequency points. @Intel(R) Xeon(R) W-2265 CPU @3.5 GHz, 12 cores, RAM 256 GB

	Case (a)	Case (b)	Case (c)
Spectral	42 s	31 s	51 s
CST (FD solver)[1]	449 s	2023 s	450 s

[1] Finite dielectric of size $1\,\text{mm} \times 0.66\,\text{mm} \times 0.33\,\text{mm}$ and *open* boundary on five faces.

In Fig. 7.4, the relative error of the input impedance has been calculated with respect to CST, for different geometries and for different values of the decay rate c. The decay rate is shown to be poorly sensitive with respect to the geometry of the dipole, as shown in Fig. 7.4(a) and (b), while its optimal value decreases with respect to the use of denser dielectrics, as shown in Fig. 7.4(c) and (d).

Thanks to the Green's function formulation of Chapter 6, the proposed spectral domain technique allows for time-efficient dipole simulations accounting for lossy and non zero thickness metal. Due to the layered media formulation and the semi-analytical Green's function, the number of unknowns of (7.18) does not scale with the ratio between the maximum and minimum dimension of the problem. In Table 7.1, the solution times for the cases of Fig. 7.2 are reported. The spectral domain approach exhibits improvements in the solution time of at least a factor ten with respect to CST. Additionally, the layered media Green's function [45] can also include frequency selective surfaces [192–194] or artificially engineered materials [49] without increasing the number of unknowns.

7.3.2. Current Distribution

As the capacitor has an impact in the current distribution and its spectrum, (7.15) has to be corrected with an additional term as follows

$$X_{\text{dip}}(k_x) * I(k_x) = \frac{V_0 F^{\Delta}(k_x) - V_{\text{end}} F^{\text{end}}(k_x)}{D(k_x)} + j\frac{\omega C V_0 F^{\Delta}(k_x)}{\Delta}. \tag{7.23}$$

where $j\omega C V_0$ models the current flowing in the capacitor given the excitation V_0. The function F^{Δ} models the confinement of the displacement currents within the source region, assuming them to be uniformly distributed. An example of the spectrum is given in Fig. 7.5(a), where the spectra (7.12) and (7.23) are compared at 180 GHz for dipoles $\ell = 500\,\mu\text{m}$, having cross section $w_y = w_z = 12.5\,\mu\text{m}$, printed between free-space and a semi-infinite material with relative permittivity $\varepsilon_r = 4$, and excited

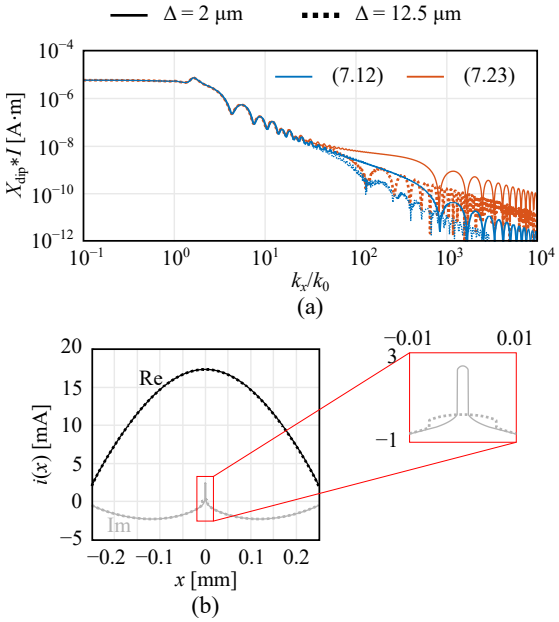

Figure 7.5: (a) Spectrum of and (b) Spatial distribution of the current at 180 GHz of a dipole having length $\ell = 500\,\mu$m, width and thickness $w_y = w_z = 12.5\,\mu$m, printed between free-space and a semi-infinite dielectric with relative permittivity $\varepsilon_r = 4$, and excited with $V_0 = 1\,$V by a Δ-gap generator.

7

with $V_0 = 1\,$V. The effect of the capacitance C of (7.23) is to place a high-frequency component, depending on Δ, while leaving untouched the spectrum around k_0. The space current distribution is calculated by performing the inverse Fourier transform of (7.23), and an example related to the previous study case is shown in Fig. 7.5(b). While the real part is unaffected by the different sizes of the feeding gap, the imaginary part peaks in correspondence with the source region when reducing Δ.

The knowledge of the current spectrum allows for the evaluation of the antenna patterns at $\vec{r} = (r_{\rm obs}, \theta_{\rm obs}, \phi_{\rm obs})$ with the following asymptotic evaluation

$$\vec{e}^{\,\rm far}\,(\vec{r}_{\rm obs}) \approx jk_{z\rm obs}\tilde{I}(k_{x\rm obs})\,J_{t,y}(k_{y\rm obs})\,\frac{e^{-jkr_{\rm obs}}}{2\pi r_{\rm obs}}\int_0^{w_z}\Big[\bar{\bar{G}}^{\rm EJ}(k_{x\rm obs}, k_{y\rm obs}, z_{\rm obs}, z')\cdot\hat{x} \times j_{t,z}\,(z')\Big]dz' \quad (7.24)$$

where $k_{x\rm obs} = k\sin\theta_{\rm obs}\cos\phi_{\rm obs}$, $k_{y\rm obs} = k\sin\theta_{\rm obs}\sin\phi_{\rm obs}$, $k_{z\rm obs} = k\cos\theta_{\rm obs}$, $J_{t,y}$ is the spectrum of the current distribution along y, $j_{t,z}$ is the current profile along z', and $\bar{\bar{G}}^{\rm EJ}$ is the spectral domain Green's function. The k_x-current spectrum $\tilde{I}$ is the

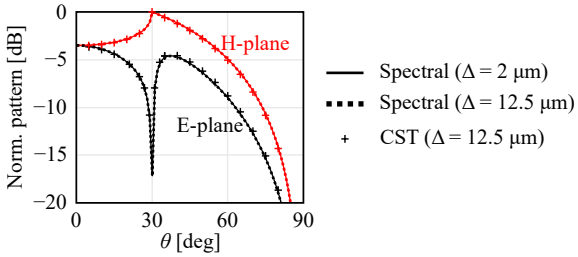

Figure 7.6: Far-field patterns at 180 GHz of a dipole having length $\ell = 500\,\mu\text{m}$, width and thickness $w_y = w_z = 12.5\,\mu\text{m}$, printed between free-space and a semi-infinite dielectric with relative permittivity $\varepsilon_r = 4$, and excited with $V_0 = 1\,\text{V}$ by a Δ-gap generator.

current spectrum windowed on the dipole, as similarly done in [195, eq. (21)], and calculated as follows

$$\tilde{I}(k_x) = \mathcal{F}\left\{\mathcal{F}^{-1}\left\{I(k_x)\right\}\chi_{\text{dip}}(x)\right\} \tag{7.25}$$

where $\mathcal{F}$ and $\mathcal{F}^{-1}$ denote the Fourier and the inverse Fourier transform operator, respectively. The radiation patterns of Fig. 7.6 refer to cases (a) and (c) of Fig. 7.2 at 180 GHz. These show the leaky radiation peaks as in [196, Fig. 5] and exhibit an excellent agreement with CST. The different sizes of the feeding gap of (a) and (b) yield a different capacitive effect on the source region, impacting the current distribution and the input impedance. Despite these differences, the two antennas share the same far-field pattern. In fact, the Green's function, for observation points sufficiently far from the sources, filters out the components of the current spectrum above the wavenumber in the domain of observation. As shown in Fig. 7.5(a), the size of the gap and its capacitive loading affect the high part of the spectrum only, and therefore, the farfields are the same.

7.3.3. Equivalent Circuit

The finite dipole solution allows for the equivalent circuit representation of Fig. 7.7, which is an extension of Fig. 6.13. The dipole can be represented by two series transmission line sections of having length $\ell/2$, characteristic impedance Z_0, and propagation constant k_{xp},where Z_0 and k_{xp} have been calculated as in Chapter 6. On either sides, these are loaded with the resistance R_{end} and the capacitance C_{end}, which represent the endpoint radiation and the low frequency capacitance, respectively, and are defined analogously as in [164, eq. (19)]. The gap is finally modelled by a transformer with turn ratio n and the gap capacitance C. The expression of the former is defined in Chapter 6 and is $n = \sin(k_{xp}\Delta/2)$, while the latter can be modelled as a parallel plate capacitor as in Section 7.3.1.

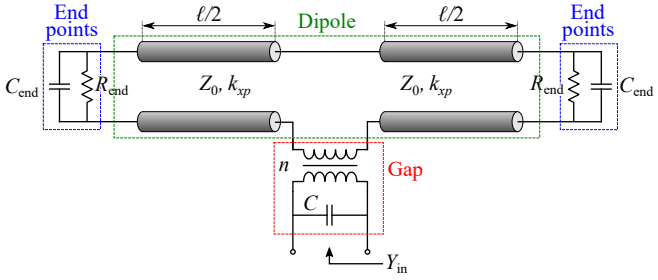

Figure 7.7: Transmission line equivalent circuit of a finite dipole, where the contributions of the feeding gap, the dipole, and the end points are highlighted.

7.4. Conclusion

A spectral domain-based representation of finite dipoles accounting for the nonzero metal thickness was developed. Based on the TL GF of Chapter 6, the method allows for an efficient semi-analytical analysis of the input impedance and the radiation patterns, whose accuracy is up to par with commercial solvers. The developed semi-analytical method can provide physical insights into the dipole's current distribution, which is linked to the input impedance and farfield radiation.

Chapter 8

Conclusion and Future Work

We, that is, all the work we have done
As waves in ether shall forever run
In ever widening spheres through heaven
Beyond the sun
–J. C. Maxwell

This dissertation presents the scientific output produced between May 2020 and April 2024 at the THz Sensing Group of the Delft University of Technology, and supported by Huawei Technologies Sweden AB under the contract YBN2020045031.

The project concerned the development of modeling techniques for different aspects of the next-generation communication systems.

On the one hand, the ultrawideband massive MIMO is modeled. With analytical techniques, the maximum number of space channels by a finite-size domain is estimated. Numerical and analytical techniques are used to clear the way to ultrawideband massive MIMO. Finally, with the aid of spectral domain representations, previously developed in [41, 45, 48], a connected array prototype is designed.

On the other hand, the modeling of high-frequency integrated antennas is presented. Spectral domain representations and the equivalent circuits derived from these allow us to simplify the full-wave simulations of integrated lens antennas for sub-THz applications.

8.1. The Modelling and Design of Wideband Massive MIMO Phased Arrays

The Number of Beams from a Given Volume Platform The maximum number of beams which can be generated from a given volume platform is assessed by means of the observable field [91, 92]. This concept is associated with the component of an impinging wave, which a finite volume platform can effectively receive. The ideal antenna, which can perform a field-matching with the observable field, has the maximum gain constrained by the volume. Consequently, one can use the field correlation between the antenna pattern $\vec{V}_{\mathrm{a}}$ and the observable field associated with the impinging wave to assess the quantity of the received power. This has a twofold purpose. Firstly, it serves as a new definition of the aperture efficiency, which is always bounded by unity regardless of antenna size. It can also be used to assess a design's effectiveness, also for small antennas. Secondly, it is used to assess an ideal, designed, or measured pattern in a massive MIMO scenario by evaluating the received signal and the interference.

High Mutual Coupling and Ultrawideband Massive MIMO The misconception that high mutual element coupling precludes ultrawideband arrays from MIMO system usage is dispelled for the first time, and later on also used by other authors [52, 53]. First, a singularity-free kernel is derived and used to assess the mutual coupling of the far-field patterns in a multi-beam configuration. Then, with a matrix formalism, the beam orthogonality is assessed for different array topologies with different levels of inter-element mutual coupling. It is shown that, for a coherent array excitation, it is possible to achieve orthogonal beams regardless of the inter-element mutual coupling. The orthogonality depends only on the beam overlap and the side lobe level. These findings pave the way to ultrawideband massive MIMO, which can achieve unprecedented data rates by enlarging the bandwidth.

A Connected Array Design for Sub-8 GHz Massive MIMO A connected array with two interchangeable ADL radomes is designed. The two radomes allow a matching between $6-8\,\mathrm{GHz}$ and $2-8\,\mathrm{GHz}$ when scanning up to $60°$ in all the azimuthal cuts. The array presents an extended bandwidth, i.e., 4:1, with respect to previous designs. The interchangeable radome solution allows to switch the operating bandwidth and the cost by keeping a single radiating section, making this design appealing for commercial applications. Finally, an 8×8 prototype is manufactured and tested.

8.2. The Modelling of Integrated Antennas

The Proxy Sources Method The proxy sources method is formulated to simplify full-wave simulations of dielectric lens antennas, for all the cases for which the Physical Optics yields inaccuracies, i.e., small-size lenses. Three phenomena contribute to the input impedance: the reactance of the feed, the radiation in a semi-infinite medium, and the reflections of the lens. While the former two can be assessed semi-analytically or with efficient full-wave simulations, the latter can be estimated by the simulation of the lens and its feed, which presents a remarkable computational burden. However, the reflections can be extracted from simplified simulations. A feed that radiates equivalently into the far-field but has a coarser discretization is synthesized. This allows for the assessment of the reflection without compromising the simulation speed. Finally, the different contributions are combined, and the original input impedance is reconstructed.

More specifically, this method was formulated to ease the simulations of the in-house volumetric method of moments of Appendix C. This can easily treat inhomogeneous bodies, e.g., complex antenna systems, including their matching layers and multiple stratifications, but due to its structured mesh, it is challenging to represent the fine details of the feed. Therefore, it becomes essential to use the proxy sources method to carry out such simulations effectively. Despite its larger benefit for structured meshes, the proxy sources method is independent of the specific type of mesh and numerical solver. Therefore, every multi-scale problem, where an integrated feed radiates close to a dielectric body, can benefit from such an approach.

Despite in Chapter 5, the proxy sources method has been applied only to a volumetric method of moments using structured mesh; it should be noted that the method is independent on the specific numerical solver, as it is based on a physical interpretation of the fields inside the lens. Therefore, surface integral solvers using unstructured meshes can also benefit from this method.

Dipole with Nonzero Metal Thickness in Layered Media A formulation used to characterize printed dipoles in nonzero metal thickness in layered media is derived. This allows for an efficient spectral domain modeling of radiating elements and printed transmission lines, which would be difficult to treat with conventional solvers. More importantly, a transmission line equivalent circuit is derived, allowing for a physical interpretation of the feed's reactance, the propagation on the dipole, and the radiation. This allows us to separate the different contributions, and it enables the application of the proxy sources method.

8.3. Future Work

The research lines of the present dissertation can be developed as follows

- The assessment of realistic prototypes using the observable field. This study aims at characterizing the prototype of Chapter 4 in a massive MIMO scenario, allowing us to assess the achieved SIR with respect to the ideal one obtained with the observable field. This investigation is currently ongoing;

- The observable field is related to the maximum antenna gain in the absence of losses. However, the maximum antenna gain is usually associated with the quality factor Q, which is closely associated with losses, as in [197]. Therefore, a extended formulation would be required to give a more complete description of the phenomena;

- The development of an alternative unit-cell design for the array of Chapter 4, based on [198]. This allows for an easier feed design, the reduction of the number of metal layers, and a more favorable vias aspect ratio, ensuring an easier manufacturing process. This investigation is currently ongoing;

- The improvement of the current V-MoM code. This should include a preconditioner, allowing the stabilization of the number of iterations for larger-size lenses and denser dielectrics. The combination of volume and surface currents would yield the easy handling of slots and ground planes;

- Due to its formulation, the V-MoM can be efficiently used in an optimization loop, as the matrix accounting for the radiation and which requires the calculation of the integrals does not depend on the geometry. For instance, it can be combined with the lens-shaping techniques [199];

- The application of the V-MoM to the estimation of the thermal radiation from ohmic materials. This aspect is used to assess the thermal noise in complex high frequency front-ends;

- The extension of the transmission line characterization of Chapter 6 and 7 to slots and coplanar waveguides. Moreover, the modeling of discontinuities in the lines, e.g., bends and different widths, would allow us to extract their lumped element equivalent to be placed in the circuit of Fig. 5.2. This would further simplify the simulation of complex geometries with the aid of the proxy sources method.

8.4. Impact of the Research

The work described in this dissertation has led to six journal papers, one paper in preparation, and sixteen conference contributions. The complete publication list is given from page 175.

The conference contributions numbered C.3 and C.14 in the above mentioned publication list were shortlisted for the *Best Electromagnetics Paper Award* at EuCAP 2021 and EuCAP 2024, respectively.

III

Appendices

Appendix A

Relations Regarding Receiving Antennas

A.1. An Alternate Expression for the Received Power

The power received by the j-th antenna, under impedance matching conditions, due to the i-th impinging wave can be written as follows

$$P_{\mathrm{r}}^{ij} = \frac{1}{8}\frac{|V_{\mathrm{oc}}^{ij}|^2}{R_L^j} \tag{A.1}$$

where V_{oc}^{ij} is the open circuit voltage induced by the i-th incident field, and R_L^j the antenna load resistance. As suggested in [95], by multiplying the numerator and the denominator of (A.1) by the power P_{a}^j radiated by j-th antenna, when fed by the current I_{a}^j, one obtains

$$P_{\mathrm{r}}^{ij} = \frac{P_{\mathrm{r}}^{ij} P_{\mathrm{a}}^j}{P_{\mathrm{a}}^j} = \frac{1}{8}\frac{|V_{oc}^{ij}|^2}{R_L^j}\frac{1}{2}\frac{R_L^j |I_{\mathrm{a}}^j|^2}{P_{\mathrm{a}}^j} = \frac{1}{16}\frac{|V_{oc}^{ij} I_{\mathrm{a}}^j|}{P_{\mathrm{a}}^j} \tag{A.2}$$

A.2. An Application of the Reciprocity Theorem

This Appendix is intended to prove (2.6), which relates $V_{oc}^{ij} I_{\mathrm{a}}^j$ with the reaction integral between the pattern of the inward observable field and the one that the receiving antenna would radiate, when used in transmission. The starting point is the applica-

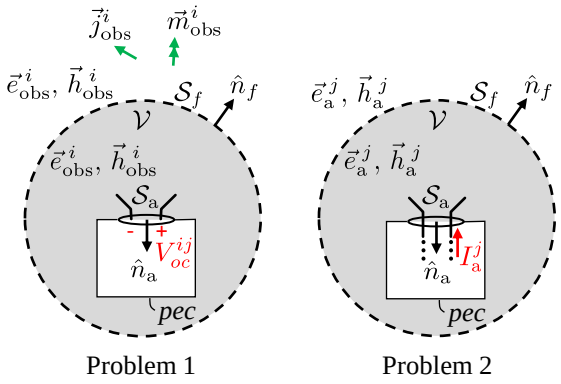

Figure A.1: The representation of Problem 1 and Problem 2 used in the reciprocity theorem.

tion of Lorentz's reciprocity theorem [97, 98], which gives

$$V^{ij}_{oc} I^{j}_{\rm a} = \oiint_{\mathcal{S}_f} \left(\vec{e}^{\,i}_{\rm obs} \times \vec{h}^{\,j}_{\rm a} - \vec{e}^{\,j}_{\rm a} \times \vec{h}^{\,i}_{\rm obs} \right) \cdot \hat{n}_f dS \tag{A.3}$$

Although the steps leading to (A.3) are described in [97, Ch. 8.7.2], and [98], we briefly report them here, revised to adapt to the notation of this dissertation. Please note that the formula of (A.3) is rigorously valid for any arbitrary incident field, however, here we assume that the only portion of the incident field that can interact with the receiving antenna is the observable field. Fig. A.1 shows an antenna enveloped by a surface $\mathcal{S}_f$, located in its far-field, and having the outer normal unit vector $\hat{n}_f$. The antenna is fed by a waveguide having the cross section $\mathcal{S}_{\rm a}$, whose normal unit vector is $\hat{n}_{\rm a}$. We define $\mathcal{V}$ as the volume comprised between $\mathcal{S}_f$, $\mathcal{S}_{\rm a}$, and the perfect electric conductor (*pec*) box, assumed to enclose the circuit connected to the antenna. Problem 1 refers to the receiving antenna, where the antenna terminals are open circuited, while Problem 2 considers the same antenna when transmitting. In Problem 1, the observable field $\vec{e}^{\,i}_{\rm obs}$ and $\vec{h}^{\,i}_{\rm obs}$ is generated by the sources $j^{i}_{\rm obs}$ and $m^{i}_{\rm obs}$ located outside $\mathcal{V}$, inducing the open-circuit voltage V^{ij}_{oc} at the antenna terminals. Problem 2, where the antenna is assumed to be fed by the current $I^{j}_{\rm a}$ and radiates the fields $\vec{e}^{\,j}_{\rm a}$ and $\vec{h}^{\,j}_{\rm a}$, is a fictitious problem formulated to apply the reciprocity theorem. By applying Lorentz's reciprocity theorem to the volume $\mathcal{V}$, since no currents are contained within, one can write

$$\iint_{\mathcal{S}_{\rm a}} \left(\vec{e}^{\,i}_{\rm obs} \times \vec{h}^{\,j}_{\rm a} - \vec{e}^{\,j}_{\rm a} \times \vec{h}^{\,i}_{\rm obs} \right) \cdot \hat{n}_{\rm a}\, dS + \oiint_{\mathcal{S}_f} \left(\vec{e}^{\,i}_{\rm obs} \times \vec{h}^{\,j}_{\rm a} - \vec{e}^{\,j}_{\rm a} \times \vec{h}^{\,i}_{\rm obs} \right) \cdot \hat{n}_f\, dS = 0. \tag{A.4}$$

Being the antenna of Problem 1 open-circuited, the magnetic field $\vec{h}^i_{\rm obs}$ on $\mathcal{S}_{\rm a}$ has nonzero normal component solely, making the triple product $\vec{e}^j_{\rm a} \times \vec{h}^i_{\rm obs} \cdot \hat{n}_{\rm a}|_{\mathcal{S}_{\rm a}}$ vanish. Then, by assuming that in the waveguide only a single mode is supported, $\vec{e}^i_{\rm obs}$ and $\vec{h}^j_{\rm a}$ can be decomposed as

$$\vec{e}^i_{\rm obs} = V^{ij}_{oc}\vec{\mathfrak{e}}_0 \tag{A.5}$$

$$\vec{h}^j_{\rm a} = I^j_{\rm a}\vec{\mathfrak{h}}_0 \tag{A.6}$$

where $\vec{\mathfrak{e}}_0$, $\vec{\mathfrak{h}}_0$ are the modal eigenvectors, and V^{ij}_{oc} and $I^j_{\rm a}$ their associated amplitudes. By substituting (A.5) and (A.6) in (A.4), one obtains

$$V^{ij}_{oc} I^j_{\rm a} \iint_{\mathcal{S}_{\rm a}} \vec{\mathfrak{e}}_0 \times \vec{\mathfrak{h}}_0 \cdot (-\hat{n}_{\rm a})\, dS = \oiint_{\mathcal{S}_f} \left(\vec{e}^i_{\rm obs} \times \vec{h}^j_{\rm a} - \vec{e}^j_{\rm a} \times \vec{h}^i_{\rm obs}\right) \cdot \hat{n}_f\, dS. \tag{A.7}$$

According to the orthonormality property of the eigenvectors $\vec{\mathfrak{e}}_0$, $\vec{\mathfrak{h}}_0$, the integral in the left hand of (A.7) is equal to one, thus proving (A.3).

Since $\mathcal{S}_f$ is in the far-field, the fields $\vec{e}^j_{\rm a}(\vec{r})$, $\vec{h}^j_{\rm a}(\vec{r})$ radiated by the antenna can be rewritten as follows

$$\vec{e}^j_{\rm a}(\vec{r}) = \vec{V}^j_{\rm a}(\hat{k})\frac{e^{-jkr}}{r} \tag{A.8}$$

$$\vec{h}^j_{\rm a}(\vec{r}) = \frac{1}{\zeta}\hat{r} \times \vec{V}^j_{\rm a}(\hat{k})\frac{e^{-jkr}}{r} \tag{A.9}$$

where ζ is the free space impedance, and the observable field can be written in the following form

$$\vec{e}^i_{\rm obs}(\vec{r}) = \vec{V}^{i,\rm inw}_{\rm obs}(\hat{k})\frac{e^{jkr}}{r} + \vec{V}^{i,\rm out}_{\rm obs}(\hat{k})\frac{e^{-jkr}}{r} \tag{A.10}$$

$$\vec{h}^j_{\rm obs}(\vec{r}) = \frac{1}{\zeta}\hat{r} \times \left(-\vec{V}^{i,\rm inw}_{\rm obs}(\hat{k})\frac{e^{jkr}}{r} + \vec{V}^{i,\rm out}_{\rm obs}(\hat{k})\frac{e^{-jkr}}{r}\right). \tag{A.11}$$

By substituting (A.8), (A.9), (A.10), and (A.11) into (A.7), and omitting the $\hat{k}$ dependence of the patterns for compactness, one obtains

$$V^{ij}_{oc} I^j_{\rm a} = \frac{1}{\zeta}\oiint_{\mathcal{S}_f}\frac{1}{r^2}\Bigg[\left(\vec{V}^{i,\rm inw}_{\rm obs} + \vec{V}^{i,\rm out}_{\rm obs}e^{-2jkr}\right) \times \left(\hat{r} \times \vec{V}^j_{\rm a}\right) - \vec{V}^j_{\rm a} \times \left(\hat{r} \times \left(-\vec{V}^{i,\rm inw}_{\rm obs}\right) + \vec{V}^{i,\rm out}_{\rm obs}e^{-2jkr}\right)\Bigg] \cdot \hat{n}_f dS \tag{A.12}$$

By expanding the vector triple products in (A.12), we can notice that the terms containing $\vec{V}_{\text{obs}}^{i,\text{out}}$ cancel out, while the ones containing $\vec{V}_{\text{obs}}^{i,\text{inw}}$ sum up. Thus, the expression simplifies as follows

$$V_{oc}^{ij} I_{\text{a}}^{j} = \frac{2}{\zeta} \oiint_{\mathcal{S}_f} \frac{1}{r^2} \left(\vec{V}_{\text{obs}}^{i,\text{inw}} \cdot \vec{V}_{\text{a}}^{j} \right) \hat{r} \cdot \hat{n}_f dS \tag{A.13}$$

By assuming that $\mathcal{S}_f$ is a sphere centered at the antenna reference system, $(\hat{r} \cdot \hat{n} dS)/r^2 = d\Omega$, leading the integration on the solid angle (i.e., (2.6))

$$V_{oc}^{ij} I_{\text{a}}^{j} = \frac{2}{\zeta} \iint_{4\pi} \vec{V}_{\text{obs}}^{i,\text{inw}}(\hat{k}) \cdot \vec{V}_{\text{a}}^{j}(\hat{k}) d\Omega. \tag{A.14}$$

Note that on the left hand side of (A.14), neither V_{oc}^{ij} nor I_{a}^{j} is conjugated, as it derives from Lorentz's reciprocity theorem. Despite the product $V_{\text{oc}}^{ij} I_{\text{a}}^{j}$ being dimensionally a power, it configures itself as a reaction [95] and relates quantities (V_{oc}^{ij} and I_{a}^{j}), associated with different sources of two separate problems.

Appendix B

Far-Field Relations and the Visible Green's Function

B.1. Vector and Dyadic Relationships for the Far-Field Patterns

In the present Section, we intend to prove that the product between two radiation patterns satisfies the following identity

$$\left[\underline{\underline{I}} - \hat{k}\hat{k}\right] \cdot \vec{J}_{n'} \cdot \left[\underline{\underline{I}} - \hat{k}\hat{k}\right] \cdot \vec{J}_n^* = \vec{J}_{n'} \cdot [\underline{\underline{I}} - \hat{k}\hat{k}] \cdot \vec{J}_n^* \tag{B.1}$$

where we omitted the dependence of the spectral current distributions $\vec{J}_n$ and $\vec{J}_{n'}$ on $\hat{k}$ to maintain a compact notation. By expanding the dyadic products on the left hand side, one obtains

$$\vec{J}_{n'} \cdot \vec{J}_n^* - \vec{J}_{n'} \cdot \hat{k}\hat{k} \cdot \vec{J}_n^* - \hat{k}\hat{k} \cdot \vec{J}_{n'} \cdot (\vec{J}_n^* - \hat{k}\hat{k} \cdot \vec{J}_n^*) \,. \tag{B.2}$$

Since the term $(\vec{J}_n^* - \hat{k}\hat{k} \cdot \vec{J}_n^*)$ only selects the transverse components of $\vec{J}_n^*$ that are not aligned with $\hat{k}$, whereas the term $(\hat{k}\hat{k} \cdot \vec{J}_{n'})$ is parallel to $\hat{k}$, one can note that

$$\hat{k}\hat{k} \cdot \vec{J}_{n'} \cdot (\vec{J}_n^* - \hat{k}\hat{k} \cdot \vec{J}_n^*) = 0. \tag{B.3}$$

By using (B.3) in (B.2) and by rearranging the dyadic products, one obtains

$$\vec{J}_{n'} \cdot [\underline{\underline{I}} - \hat{k}\hat{k}] \cdot \vec{J}_n^* \,. \tag{B.4}$$

B.2. Expression of the Visible Green's Function

In this Section, we derive a convenient analytical expression of the visible Green's function, which was defined in (3.8) as

$$\underline{\underline{g}}^{\text{vis}}(\vec{r}) = \frac{-k^2\zeta}{16\pi^2} \iint\limits_{4\pi} \left[\underline{\underline{I}} - \hat{k}\hat{k}\right] e^{-jk\hat{k}\cdot\vec{r}} d\Omega \,. \tag{B.5}$$

Recalling the following property for the plane-wave spectral representation

$$\hat{k}\hat{k}e^{-jk\hat{k}\cdot\vec{r}} = -\frac{\nabla\nabla\cdot}{k^2} e^{-jk\hat{k}\cdot\vec{r}} \tag{B.6}$$

and exchanging the order of the differential and integral operators, we can express the visible Green's function as

$$\underline{\underline{g}}^{\text{vis}}(\vec{r}) = \frac{-k^2\zeta}{16\pi^2} \left[\underline{\underline{I}} + \frac{\nabla\nabla\cdot}{k^2}\right] \iint\limits_{4\pi} e^{-jk\hat{k}\cdot\vec{r}} d\Omega \,. \tag{B.7}$$

The integral figuring in (B.7) can be closed according to what is proved in Appendix B.3, thus $\underline{\underline{g}}^{\text{vis}}$ can be written as follows

$$\underline{\underline{g}}^{\text{vis}}(\vec{r}) = -\frac{\zeta}{4\pi} \left[k^2\underline{\underline{I}} + \nabla\nabla\cdot\right] \text{sinc}(kr) \,. \tag{B.8}$$

B.3. Integration of a Complex Exponential over the Solid Angle

In the present Section we would like to prove the following integral asymptotic approximation

$$\int\limits_0^{2\pi} \int\limits_0^{\pi} e^{-jk\hat{k}\cdot\vec{r}} \sin\theta d\theta d\phi = 4\pi \,\text{sinc}(kr). \tag{B.9}$$

Since $\vec{r}$ and $\hat{k}$ can be written as

$$\vec{r} = r(\sin\theta\cos\phi\hat{x} + \sin\theta\sin\phi\hat{y} + \cos\theta\hat{z}) \tag{B.10}$$

$$\hat{k} = \sin\beta\cos\alpha\hat{x} + \sin\beta\sin\alpha\hat{y} + \cos\beta\hat{z} \tag{B.11}$$

the left hand side of equation (B.9) can be rewritten as follows

$$\int_0^{\pi} e^{jrk\cos\beta\cos\theta}\sin\theta\left[\int_0^{2\pi} e^{jrk\sin\beta\sin\theta\cos(\alpha-\phi)}d\phi\right]d\theta. \tag{B.12}$$

The integral in brackets has a closed form solution [200], yielding (B.12) to become as follows

$$2\pi\int_0^{\pi} e^{jrk\cos\beta\cos\theta}J_0(kr\sin\beta\sin\theta)\sin\theta d\theta \tag{B.13}$$

where J_0 is the zeroth order Bessel function of first kind. By using the asymptotic expansion of J_0 given in [200] and by using trigonometric identities, (B.13) becomes

$$\pi e^{-j\frac{\pi}{4}}\int_0^{\pi}\sqrt{\frac{2}{\pi kr\sin\beta\sin\theta}}e^{jkr\cos(\beta-\theta)\sin\theta}d\theta + \pi e^{j\frac{\pi}{4}}\int_0^{\pi}\sqrt{\frac{2}{\pi kr\sin\beta\sin\theta}}e^{-jkr\cos(\beta+\theta)\sin\theta}d\theta. \tag{B.14}$$

By applying the stationary phase point method, (B.14) can be rewritten as

$$\pi e^{-j\frac{\pi}{4}}\sqrt{\frac{2}{\pi kr\sin\beta\sin\theta'_s}}\sin\theta'_s\int_0^{\pi} e^{jkr\cos(\beta-\theta)}d\theta + \pi e^{j\frac{\pi}{4}}\sqrt{\frac{2}{\pi kr\sin\beta\sin\theta''_s}}\sin\theta''_s\int_0^{\pi} e^{-jkr\cos(\beta+\theta)}d\theta \tag{B.15}$$

where θ'_s and θ''_s are the saddle points of the phase functions figuring in the first and in the second integral respectively. By forcing the derivatives of these phase functions to be null, the stationary phase points can be found

$$\theta'_s = \pm\beta, \qquad \theta''_s = \mp\beta \tag{B.16}$$

Since for both saddle points the solution must be an element in the integration domain $[0, 2\pi]$, it follows that

$$\theta'_s = \theta''_s = \beta. \tag{B.17}$$

By substituting (B.17) in (B.15), one obtains:

$$\pi e^{-j\frac{\pi}{4}}\sqrt{\frac{2}{\pi kr}}\int_0^{\pi} e^{jkr\cos(\beta-\theta)}d\theta + \pi e^{j\frac{\pi}{4}}\sqrt{\frac{2}{\pi kr}}\int_0^{\pi} e^{-jkr\cos(\beta+\theta)}d\theta \tag{B.18}$$

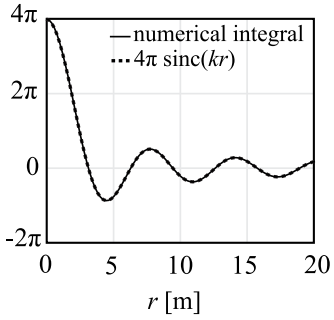

Figure B.1: Comparison between (B.9) evaluated numerically and its analytical asymptotic solution (i.e., $4\pi\,\mathrm{sinc}(kr)$), for $k = 1\,\mathrm{m}^{-1}$.

As reported in [200], both integrals can be closed into zeroth order Bessel functions of the first kind, by using their asymptotic expansion (B.18) becomes

$$\pi e^{-j\frac{\pi}{4}}\sqrt{\frac{2}{\pi kr}}e^{-j\frac{\pi}{4}}\sqrt{\frac{2\pi}{kr}}e^{jkr} + \pi e^{j\frac{\pi}{4}}\sqrt{\frac{2}{\pi kr}}e^{j\frac{\pi}{4}}\sqrt{\frac{2\pi}{kr}}e^{-jkr}. \tag{B.19}$$

Calculating the products of (B.19) and then using Euler's identities leads to:

$$4\pi\frac{\sin(kr)}{kr} = 4\pi\,\mathrm{sinc}(kr) \tag{B.20}$$

which proves the identity (B.9). In Fig. B.1, the numerical integral in (B.9) is compared with its closed-form solution.

Appendix C

The Volumetric Method of Moments

A Volumetric Method of Moments (V-MoM) has been developed to study small-size dielectric lenses effectively, allowing for the easy handling of inhomogeneous bodies.

Thanks to its formulation, the linear system governing the problem comprises a matrix, which depends on the material and whose entries are analytical, and a second matrix, whose entries are calculated regardless of the specific arrangement of the materials. Therefore, this latter can be precomputed and be used for all the geometries sharing the same discretization, making it an efficient numerical solver to be used in a design loop.

C.1. The Volume Equivalent Current Integral Equation

The solver relies on the volume equivalent current formulation [201, 202] of the volume integral equation. In the case of a scatterer having permittivity $\varepsilon_r(\vec{r})$ distributed on a domain $\mathcal{V}$ located in free-space, the equivalent currents $\vec{J}_{\text{eq}}(\vec{r})$ are defined as follows

$$\vec{J}_{\text{eq}}(\vec{r}) = j\omega\varepsilon_0 (\varepsilon_r(\vec{r}) - 1)\, \vec{E}(\vec{r}) \tag{C.1}$$

where $\vec{E}$ is the total field in $\mathcal{V}$. The integral equation can be, therefore, written as follows

$$\vec{E}^i(\vec{r}) = \frac{\vec{J}_{\text{eq}}(\vec{r})}{j\omega\varepsilon_0 (\varepsilon_r(\vec{r}) - 1)} - \frac{1}{j\omega\varepsilon_0} \left(k_0^2 + \nabla\nabla\cdot\right) \iiint_{\mathcal{V}} g(\vec{r} - \vec{r}')\, \vec{J}_{\text{eq}}(\vec{r}')\, dV' \tag{C.2}$$

where $\vec{E}^i$ is the forcing term and $g(\vec{r})$ is the scalar Green's function defined as $\exp(-jk_0|\vec{r}|)/(4\pi|\vec{r}|)$. The second term of the right-hand side of (C.2) represents the field radiated in free space by the equivalent currents $\vec{J}_{\text{eq}}$ located in $\mathcal{V}$. In (C.2), $\vec{J}_{\text{eq}}(\vec{r})$ represents the unknown as it depends on the total field $\vec{E}(\vec{r})$, and it figures both outside and inside an integral operator defined over a volume.

As the volume equivalent currents do not necessarily have to hold any continuity condition, cubic piece-wise constant basis functions are employed together with Galerkin testing. In addition to this, as discussed in [201–203], this solution allows for an improved convergence of the solution.

We divide $\mathcal{V}$ into $N = N_x \times N_y \times N_z$ cubes of edge Δ. Each voxel hosts three different basis functions oriented along $\hat{x}$, $\hat{y}$, or $\hat{z}$. In the n-th voxel, the current can be represented as follows

$$\vec{b}_n(\vec{r}) = \frac{1}{\Delta^2}\,\text{rect}\left(\frac{x-x_n}{\Delta}\right)\text{rect}\left(\frac{y-y_n}{\Delta}\right)\text{rect}\left(\frac{z-z_n}{\Delta}\right)\hat{p}_n \tag{C.3}$$

with $\hat{p}_n \in \{\hat{x}, \hat{y}, \hat{z}\}$. The numbering is devised in such a way that the total number of the basis functions is $3N$, with the x-oriented currents numbered between 1 and N, the y-oriented currents numbered between $N+1$ and $2N$, and the z-oriented currents numbered between $2N+1$ and $3N$.

The inner product $\langle \vec{a}, \vec{b} \rangle_{\mathcal{V}}$ is defined as the volume integral over $\mathcal{V}$ of the scalar product between $\vec{a}$ and $\vec{b}$. By performing the inner products of the left and the right-hand side of (C.2) on $\vec{b}_m$, one obtains the following equation

$$\begin{aligned}\langle \vec{E}^i(\vec{r}), \vec{b}_m \rangle_{\mathcal{V}_m} = \sum_{n=1}^{3N} i_n \Bigg[&\langle \frac{\vec{b}_n}{j\omega\varepsilon_0(\varepsilon_r(\vec{r})-1)}, \vec{b}_m \rangle_{\mathcal{V}_m} \\ &- \frac{1}{j\omega\varepsilon_0}\langle \left(k_0^2 + \nabla\nabla\cdot\right) \iiint_{\mathcal{V}_n} g(\vec{r}-\vec{r}')\,\vec{b}_n(\vec{r}')\,dV', \vec{b}_m \rangle_{\mathcal{V}_m} \Bigg].\end{aligned} \tag{C.4}$$

C.2. The Matrix Equation

From (C.4) the following matrix equation can be derived

$$\mathbf{v} = \left(\mathbf{Z}^{\text{mat}} + \mathbf{Z}^{\text{rad}}\right)\mathbf{i} \tag{C.5}$$

where the forcing term $\mathbf{v}$ depends on the incident field, $\mathbf{Z}^{\text{mat}}$ on the different materials of the scatterer, and $\mathbf{Z}^{\text{rad}}$ on the radiative interaction between the source and the testing points.

The n-th entry of the forcing vector can be calculated as follows

$$v_n = \langle \vec{E}^i(\vec{r}), \vec{b}_m \rangle_{\mathcal{V}_m} = \Delta \vec{E}^i(\vec{r}_m) \cdot \hat{p}_m \tag{C.6}$$

The mn-th entry of $\mathbf{Z}^{\text{mat}}$ can be obtained with the following inner product

$$Z^{\text{mat}}_{mn} = \langle \frac{\vec{b}_n}{j\omega\varepsilon_0(\varepsilon_r(\vec{r})-1)}, \vec{b}_m \rangle_{\mathcal{V}_m} = \frac{1}{j\omega\varepsilon_0(\varepsilon_r(\vec{r}_m)-1)\Delta}\delta_{mn} \tag{C.7}$$

where δ_{mn} is the Kronecker delta, yielding to a diagonal form for the matrix $\mathbf{Z}^{\text{mat}}$.

In turn, $\mathbf{Z}^{\text{rad}}$ is obtained from the second inner product in the right-hand side of (C.4). This is calculated in free space and therefore it does not depend on the materials or the geometry. Therefore, this matrix can be stored and then used for all the problem studied with the same grid, regardless of the specific geometry.

However, its calculation, involving the radiation integrals, is not straightforward. Moreover, in the case of co-located or adjacent source and test voxels, the $1/r^3$ singularity arises, and requiring a careful treatment of the computation. To ease the calculation, the same procedure of [202] is used. This allows to transform the double volume integral to a double surface integral, and reducing the singularity from $1/r^3$ to the more traditional form of $1/r$.

First, the differential operator is transformed in an alternative form, by resorting to Maxwell's equations and properties of the radiation integrals. The Ampere-Maxwell's law, for the field associated with the n-th basis function, can be written as follows

$$\begin{aligned} \nabla \times \vec{H}^s_n(\vec{r}) &= \vec{b}_n(\vec{r}) + j\omega\varepsilon_0 \vec{E}^s_n(\vec{r}) \\ &= \vec{b}_n(\vec{r}) + \left(k_0^2 + \nabla\nabla\cdot\right) \iiint_{\mathcal{V}} g(\vec{r}-\vec{r}\,')\, \vec{b}_n(\vec{r})\, dV'. \end{aligned} \tag{C.8}$$

According to the auxiliary potentials [204, Ch. 3] the magnetic field $\vec{H}^s_n(\vec{r})$ can be expressed as follows

$$\vec{H}^s_n(\vec{r}) = \nabla \times \iiint_{\mathcal{V}} g(\vec{r}-\vec{r}\,')\, \vec{b}_n(\vec{r})\, dV'. \tag{C.9}$$

By substituting (C.9) into (C.8), one obtains the following indentity

$$\nabla \times \nabla \times \iiint_{\mathcal{V}} g(\vec{r}-\vec{r}\,')\, \vec{b}_n(\vec{r})\, dV' = \vec{b}_n(\vec{r}) + \left(k_0^2 + \nabla\nabla\cdot\right) \iiint_{\mathcal{V}} g(\vec{r}-\vec{r}\,')\, \vec{b}_n(\vec{r})\, dV'. \tag{C.10}$$

By using (C.10), the entire inner product becomes as follows

$$\begin{aligned} Z^{\text{rad}}_{mn} &= \frac{1}{j\omega\varepsilon_0}\left(\langle \vec{b}_n, \vec{b}_m \rangle_{\mathcal{V}_m} - \langle \nabla \times \nabla \times \iiint_{\mathcal{V}_n} g(\vec{r}-\vec{r}\,')\, \vec{b}_n(\vec{r})\, dV', \vec{b}_m \rangle_{\mathcal{V}_m}\right) \\ &= \frac{1}{j\omega\varepsilon_0}\left(\frac{\delta_{mn}}{\Delta} - \langle \nabla \times \nabla \times \iiint_{\mathcal{V}_n} g(\vec{r}-\vec{r}\,')\, \vec{b}_n(\vec{r})\, dV', \vec{b}_m \rangle_{\mathcal{V}_m}\right). \end{aligned} \tag{C.11}$$

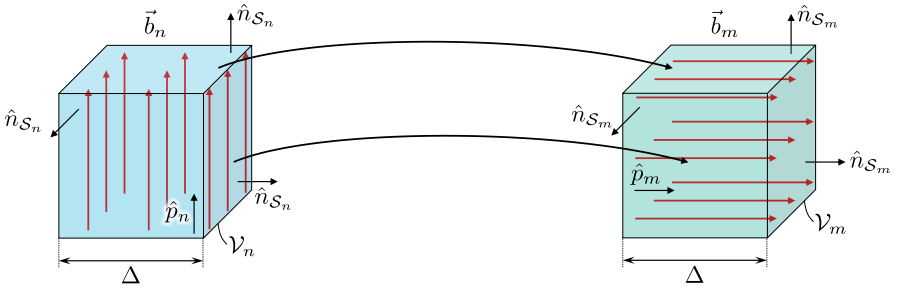

Figure C.1: Sketch of the projection expressed in terms of the volume integrals of (C.12)

The inner product between the double curl of the scalar potential generated by the n-th basis function and the m-th test function can be written as

$$\iiint_{\mathcal{V}_m} \vec{b}_m(\vec{r}) \cdot \left(\nabla \times \nabla \times \iiint_{\mathcal{V}_n} g(\vec{r}-\vec{r}\,') \, \vec{b}_n(\vec{r}\,') \, dV' \right) dV \tag{C.12}$$

where $\mathcal{V}_m$ and $\mathcal{V}_n$ are the supports of the test and basis functions, and the operation is sketched in Fig. C.1. By applying one of the differential relations[1], (C.12) becomes

$$-\iiint_{\mathcal{V}_m} \nabla \cdot \left(\vec{b}_m(\vec{r}) \times \nabla \times \iiint_{\mathcal{V}_n} g(\vec{r}-\vec{r}\,') \, \vec{b}_n(\vec{r}\,') \, dV' \right) dV \tag{C.13}$$

where the term $\nabla \times \vec{b}_m$ vanishes, being $\vec{b}_m$ a constant function in $\mathcal{L}^2$. By applying the divergence theorem[2] to (C.13), one can transform the volume integral on $\mathcal{V}_m$ into the flux through $\mathcal{S}_m$, i.e., the surface enclosing $\mathcal{V}_m$, as

$$-\oiint_{\mathcal{S}_m} \left[\vec{b}_m(\vec{r}) \times \left(\nabla \times \iiint_{\mathcal{V}_n} g(\vec{r}-\vec{r}\,') \, \vec{b}_n(\vec{r}\,') \, dV' \right) \right] \cdot \hat{n}_{\mathcal{S}_m} dS \tag{C.14}$$

where $\hat{n}_{\mathcal{S}_m}$ is the outwardly oriented normal unit vector of $\mathcal{S}_m$. By permuting the vectors in the triple product, one obtains the following expression

$$-\oiint_{\mathcal{S}_m} \left(\hat{n}_{\mathcal{S}_m} \times \vec{b}_m(\vec{r}) \right) \cdot \nabla \times \iiint_{\mathcal{V}_n} g(\vec{r}-\vec{r}\,') \, \vec{b}_n(\vec{r}\,') \, dV' dS. \tag{C.15}$$

1
$$\nabla \cdot \left(\vec{a} \times \vec{b} \right) = \vec{b} \cdot \nabla \times \vec{a} - \vec{a} \cdot \nabla \times \vec{b}$$

2
$$\iiint_{\mathcal{V}} \nabla \cdot \vec{F} dV = \oiint_{\mathcal{S}} \vec{F} \cdot \hat{n}_{\mathcal{S}} dS$$
where $\mathcal{S}$ is the surface enclosing the volume $\mathcal{V}$, and $\hat{n}_{\mathcal{S}}$ is the outwardly oriented normal unit vector

Since the curl operates with respect to $\vec{r}$, it can be taken inside the volume integral, that is calculated with respect to $\vec{r}\,'$

$$-\oiint_{\mathcal{S}_m}\left(\hat{n}_{\mathcal{S}_m}\times\vec{b}_m\left(\vec{r}\right)\right)\cdot\iiint_{\mathcal{V}_n}\nabla\times\left(g(\vec{r}-\vec{r}\,')\,\vec{b}_n\left(\vec{r}\,'\right)\right)dV'dS. \tag{C.16}$$

By resorting to the well-known differential relations, one can calculate the curl as

$$\begin{aligned}\nabla\times\left(g\left(\vec{r},\vec{r}\right)\vec{b}_n\left(\vec{r}\,'\right)\right) &= g(\vec{r}-\vec{r}\,')\,\nabla\times\vec{b}_n\left(\vec{r}\,'\right)+\nabla g(\vec{r}-\vec{r}\,')\times\vec{b}_n\left(\vec{r}\,'\right)\\ &= \nabla g(\vec{r}-\vec{r}\,')\times\vec{b}_n\left(\vec{r}\,'\right)\end{aligned} \tag{C.17}$$

with $\nabla\times\vec{b}_n\left(\vec{r}\,'\right)=0$, since the differential operation is performed with respect to $\vec{r}$, and (C.16) becomes as follows

$$-\oiint_{\mathcal{S}_m}\left(\hat{n}_{\mathcal{S}_m}\times\vec{b}_m\left(\vec{r}\right)\right)\cdot\iiint_{\mathcal{V}_n}\nabla g(\vec{r}-\vec{r}\,')\times\vec{b}_n\left(\vec{r}\,'\right)dV'dS. \tag{C.18}$$

Since $\vec{b}_n$ and $\vec{b}_m$ are constant functions in $\mathcal{L}^2$, (C.18) becomes

$$-\frac{1}{\Delta^4}\oiint_{\mathcal{S}_m}\left(\hat{n}_{\mathcal{S}_m}\times\hat{p}_m\right)\cdot\left(\hat{p}_n\times\iiint_{\mathcal{V}_n}-\nabla g(\vec{r}-\vec{r}\,')\,dV'\right)dS. \tag{C.19}$$

By making use of the relation $\nabla g(\vec{r}-\vec{r}\,')=-\nabla' g(\vec{r}-\vec{r}\,')$, where ∇' is the differentiation with respect to $\vec{r}\,'$, (C.19) becomes as follows

$$-\frac{1}{\Delta^4}\oiint_{\mathcal{S}_m}\left(\hat{n}_{\mathcal{S}_m}\times\hat{p}_m\right)\cdot\left(\hat{p}_n\times\iiint_{\mathcal{V}_n}\nabla' g(\vec{r}-\vec{r}\,')\,dV'\right)dS. \tag{C.20}$$

By applying to (C.20) one of the corollaries[3] of the divergence theorem

$$-\frac{1}{\Delta^4}\oiint_{\mathcal{S}_m}\left(\hat{n}_{\mathcal{S}_m}\times\hat{p}_m\right)\cdot\left(\hat{p}_n\times\oiint_{\mathcal{S}_n}\hat{n}_{\mathcal{S}_n}g(\vec{r}-\vec{r}\,')\,dS'\right)dS. \tag{C.21}$$

The cubic surfaces $\mathcal{S}_n$ and $\mathcal{S}_m$ can be written as the union of their six square faces as follows

$$\mathcal{S}_m=\bigcup_{k=1}^{6}\mathcal{S}_{m,k},\quad \mathcal{S}_n=\bigcup_{l=1}^{6}\mathcal{S}_{n,l}. \tag{C.22}$$

[3]By applying the divergence theorem to one of the differential identities one obtains

$$\iiint_{\mathcal{V}}\vec{c}\cdot\nabla f dV=\oiint_{\mathcal{S}}\vec{c}f\cdot\hat{n}dS-\iiint_{\mathcal{V}}f\,\nabla\cdot\vec{c}\,dV.$$

If $\vec{c}$ is a constant

$$\iiint_{\mathcal{V}}\nabla f dV=\oiint_{\mathcal{S}}f\cdot\hat{n}dS.$$

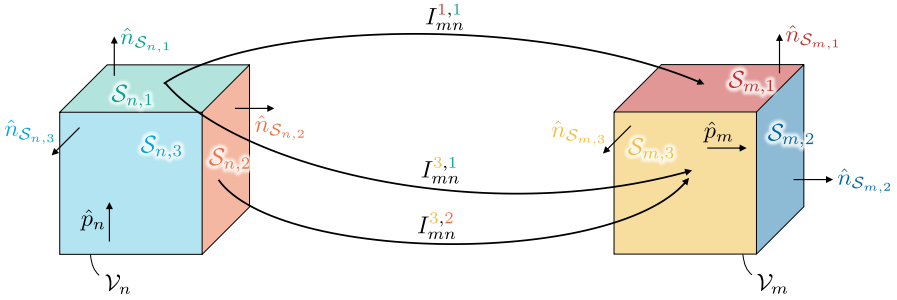

Figure C.2: Sketch of the projection (C.24), expressed as surface integrals.

Therefore, for linearity, (C.21) becomes as follows

$$-\sum_{k=1}^{6}\iint_{\mathcal{S}_{m,k}}\left(\hat{n}_{\mathcal{S}_{m,k}}\times\hat{p}_m\right)\cdot\left(\sum_{l=1}^{6}\hat{p}_n\times\iint_{\mathcal{S}_{n,l}}\hat{n}_{\mathcal{S}_{n,l}}g(\vec{r}-\vec{r}\,')\,dS'\right)dS. \tag{C.23}$$

As the unit vectors are constants with respect to the integration variables, (C.23) can be transformed as follows

$$\sum_{k=1}^{6}\sum_{l=1}^{6}\left(\hat{n}_{\mathcal{S}_{m,k}}\times\hat{p}_m\right)\cdot\left(\hat{n}_{\mathcal{S}_{n,l}}\times\hat{p}_n\right)I^{kl}_{mn} \tag{C.24}$$

where I^{kl}_{mn} is defined as follows

$$I^{kl}_{mn}=\iint_{\mathcal{S}_{m,k}}\iint_{\mathcal{S}_{n,l}}g(\vec{r}-\vec{r}\,')\,dS'dS \tag{C.25}$$

and it represents the interaction between sources located on $\mathcal{S}_{n,l}$ with the observation located on $\mathcal{S}_{m,k}$. An example of this operation is sketched in Fig. C.2. The relation (C.24) is derived from (C.12), and thanks to the divergence theorem, the volume integrals of differentiated functions are transformed into surface integrals. This reduces the $1/r^3$ singularity to the easier form of $1/r$. The integration of (C.25) can be efficiently treated with the quadrature of [205]. Finally, the entries of $\mathbf{Z}^{\text{rad}}$ can be written as follows

$$Z^{\text{rad}}_{mn}=\frac{1}{j\omega\varepsilon_0}\left(\frac{\delta_{mn}}{\Delta}-\sum_{k=1}^{6}\sum_{l=1}^{6}\left(\hat{n}_{\mathcal{S}_{m,k}}\times\hat{p}_m\right)\cdot\left(\hat{n}_{\mathcal{S}_{n,l}}\times\hat{p}_n\right)I^{kl}_{mn}\right) \tag{C.26}$$

C.3. The Numerical Solution

Due to the discretization of the volume with uniform steps, the linear system (C.5) can easily gain prohibitive memory requirements and computational complexity. However, these issues can be overcome with the Conjugate Gradient-Fast Fourier Transform (CG-FFT) [206], which allows us to reduce the computational complexity to $\mathcal{O}(n_{\text{steps}} \log_2 N)$, assuming n_{steps} for the convergence, and the memory requirements to $\mathcal{O}(n_{\text{steps}} N)$.

C.3.1. The Storage of the Entries

The linear system (C.5) requires the handling of the matrices $\mathbf{Z}^{\text{mat}}$ and $\mathbf{Z}^{\text{rad}}$, which both have $9N^2$ entries. Due to the large scale of the problem, these might exceed the memory resources of the computational systems at hand, or in any case, their allocation and handling require a large computational effort.

Due to its diagonal nature, $\mathbf{Z}^{\text{mat}}$ does not require the storage of all the entries, but only of their $3N$ diagonal terms in the form of vectors. Moreover, as highlighted in (C.7), its entries can be calculated analytically.

On the contrary, $\mathbf{Z}^{\text{rad}}$ is a full matrix whose entries require a careful evaluation. However, thanks to the radiation operator's space invariance and symmetries, a reduced number of entries can be computed and stored. The matrix $\mathbf{Z}^{\text{rad}}$ is configured as follows

$$\mathbf{Z}^{\text{rad}} = \begin{bmatrix} \mathbf{Z}^{\text{rad}}_{xx} & \mathbf{Z}^{\text{rad}}_{xy} & \mathbf{Z}^{\text{rad}}_{xz} \\ \mathbf{Z}^{\text{rad}}_{yx} & \mathbf{Z}^{\text{rad}}_{yy} & \mathbf{Z}^{\text{rad}}_{yz} \\ \mathbf{Z}^{\text{rad}}_{zx} & \mathbf{Z}^{\text{rad}}_{zy} & \mathbf{Z}^{\text{rad}}_{zz} \end{bmatrix} \tag{C.27}$$

where each term $\mathbf{Z}^{\text{rad}}_{mn}$ is a block Toeplitz matrix which describes the interaction between m- and n-oriented currents. Thanks to reciprocity $\mathbf{Z}^{\text{rad}}_{mn} = \mathbf{Z}^{\text{rad}}_{nm}$ and thanks to the symmetries $\mathbf{Z}^{\text{rad}}_{xx} = \mathbf{Z}^{\text{rad}}_{yy} = \mathbf{Z}^{\text{rad}}_{zz}$, only four distinct submatrices exist. Each of these has N^2 entries and, therefore, cannot be conveniently stored for large problems. However, for the properties of Toeplitz matrices, it is sufficient to calculate and store $(2N_x - 1) \times (2N_y - 1) \times (2N_z - 1)$ specific entries to characterize the entire matrix. These can be arranged in a three-dimensional tensor, where all the entries in the same column have the same x, all the entries in the same row have the same y, and all the entries in the same page have the same z. For instance, page k of the mn polarizations

configures itself as follows

$$\ddot{\mathbf{z}}^{\mathrm{rad}}_{mn}\big|_k = \begin{bmatrix} Z^{mn}_{N_{x-1},N_{y-1}} & \cdots & Z^{mn}_{N_{x-1},1} & Z^{mn}_{N_{x-1},0} & Z^{mn}_{N_{x-1},-1} & \cdots & Z^{mn}_{N_{x-1},1-N_y} \\ \vdots & \ddots & \vdots & \vdots & \vdots & & \vdots \\ Z^{mn}_{1,N_{y-1}} & \cdots & Z^{mn}_{1,1} & Z^{mn}_{1,0} & Z^{mn}_{1,-1} & \cdots & Z^{mn}_{1,1-N_y} \\ Z^{mn}_{0,N_{y-1}} & \cdots & Z^{mn}_{0,1} & Z^{mn}_{0,0} & Z^{mn}_{0,-1} & \cdots & Z^{mn}_{0,1-N_y} \\ Z^{mn}_{-1,N_{y-1}} & \cdots & Z^{mn}_{-1,1} & Z^{mn}_{-1,0} & Z^{mn}_{-1,-1} & \cdots & Z^{mn}_{-1,1-N_y} \\ \vdots & & \vdots & \vdots & \vdots & \ddots & \vdots \\ Z^{mn}_{1-N_x,N_{y-1}} & \cdots & Z^{mn}_{1-N_x,1} & Z^{mn}_{1-N_x,0} & Z^{mn}_{1-N_x,-1} & \cdots & Z^{mn}_{1-N_x,1-N_y} \end{bmatrix}. \tag{C.28}$$

The subscripts in the entries of (C.28) indicate the distance in terms of basis functions between the source and the testing point. The third index in the subscript has been omitted, as all the elements involved share the same z. The tensor $\ddot{\mathbf{z}}^{\mathrm{rad}}_{mn}$ contains the minimum number of interactions needed to characterize the matrix $\mathbf{Z}^{\mathrm{rad}}_{mn}$. The tensor $\ddot{\mathbf{z}}^{\mathrm{rad}}_{mn}$ stores all the unique interactions, in such a way that the each $\ddot{\mathbf{z}}^{\mathrm{rad}}_{mn}\big|_{i,j,k}$ is the interaction between the first element i.e., the cell of index $(0,0,0)$, and the element (i,j,k). To distinguish the proper impedance matrix $\mathbf{Z}^{\mathrm{rad}}_{mn}$ from the tensor of the interactions, this latter is identified with the lowercase letter, and the three dots denoting its three dimensional storage.

Due to the rotational symmetries, only a tensor of co-polarized and a tensor of cross-polarized sources have to be calculated. Let us calculate $\ddot{\mathbf{z}}^{\mathrm{rad}}_{xx}$ and $\ddot{\mathbf{z}}^{\mathrm{rad}}_{xy}$, the remaining tensors can be derived as follows

$$\ddot{\mathbf{z}}^{\mathrm{rad}}_{yy}\big|_{i,j,k} = \ddot{\mathbf{z}}^{\mathrm{rad}}_{xx}\big|_{j,i,k} \tag{C.29}$$

$$\ddot{\mathbf{z}}^{\mathrm{rad}}_{zz}\big|_{i,j,k} = \ddot{\mathbf{z}}^{\mathrm{rad}}_{xx}\big|_{k,i,j} \tag{C.30}$$

$$\ddot{\mathbf{z}}^{\mathrm{rad}}_{xz}\big|_{i,j,k} = \ddot{\mathbf{z}}^{\mathrm{rad}}_{xy}\big|_{i,k,j} \tag{C.31}$$

$$\ddot{\mathbf{z}}^{\mathrm{rad}}_{yz}\big|_{i,j,k} = \ddot{\mathbf{z}}^{\mathrm{rad}}_{xy}\big|_{k,i,j}. \tag{C.32}$$

The calculation of $\ddot{\mathbf{z}}^{\mathrm{rad}}_{xx}$ and $\ddot{\mathbf{z}}^{\mathrm{rad}}_{xy}$ is sufficient only to characterize all the radiative interactions. However, the remaining tensors $\ddot{\mathbf{z}}^{\mathrm{rad}}_{yy}$, $\ddot{\mathbf{z}}^{\mathrm{rad}}_{zz}$, $\ddot{\mathbf{z}}^{\mathrm{rad}}_{xz}$, and $\ddot{\mathbf{z}}^{\mathrm{rad}}_{yz}$, calculated with the permutations shown above, have to be stored.

C.3.2. The Calculation of the Products and the Integrals of (C.24)

The calculation of $\ddot{\mathbf{z}}^{\mathrm{rad}}_{xx}$ and $\ddot{\mathbf{z}}^{\mathrm{rad}}_{xy}$ can be further simplified with some geometrical considerations, symmetries, and tensor operations.

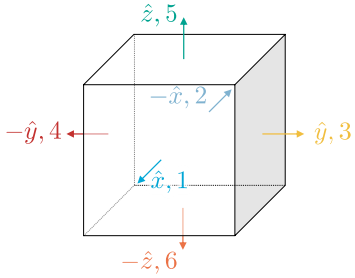

Figure C.3: Numbering of the faces, and their normal unit vectors, of each voxel.

Co-polarized Currents. When calculating $\ddot{\mathbf{z}}_{xx}^{\mathrm{rad}}$, (C.24) becomes as follows

$$\sum_{k=1}^{6}\sum_{l=1}^{6}\left(\hat{n}_{\mathcal{S}_{m,k}}\times\hat{x}\right)\cdot\left(\hat{n}_{\mathcal{S}_{n,l}}\times\hat{x}\right)I_{mn}^{kl} \tag{C.33}$$

where the straightforward calculation of the products $\left(\hat{n}_{\mathcal{S}_{m,k}}\times\hat{x}\right)\cdot\left(\hat{n}_{\mathcal{S}_{n,l}}\times\hat{x}\right)$ is summarized in the following table

	$\hat{x}$	$-\hat{x}$	$\hat{y}$	$-\hat{y}$	$\hat{z}$	$-\hat{z}$
$\hat{x}$	0	0	0	0	0	0
$-\hat{x}$	0	0	0	0	0	0
$\hat{y}$	0	0	1	−1	0	0
$-\hat{y}$	0	0	−1	1	0	0
$\hat{z}$	0	0	0	0	1	−1
$-\hat{z}$	0	0	0	0	−1	1

(C.34)

resulting into nonzero entries only for the eight cases for which $\hat{n}_{\mathcal{S}_{m,k}}$ and $\hat{n}_{\mathcal{S}_{n,l}}$ are both parallel to $\hat{y}$ or $\hat{z}$. Therefore, the double sum of (C.33) simplifies into

$$I_{mn}^{33}-I_{mn}^{34}-I_{mn}^{43}+I_{mn}^{44}+I_{mn}^{55}-I_{mn}^{56}-I_{mn}^{65}+I_{mn}^{66} \tag{C.35}$$

considering the superscript numbering of Fig. C.3. Due to the symmetries, one can recognize that $I_{mn}^{33}=I_{mn}^{44}=I_{mn}^{55}=I_{mn}^{66}$. When calculating all the entries of $\ddot{\mathbf{z}}_{xx}^{\mathrm{rad}}$, one can exploit the rotational and translational symmetries to reduce the number of integrals to perform.

Cross-polarized Currents. In the calculation of $\ddot{\mathbf{z}}_{xy}^{\mathrm{rad}}$, (C.24) becomes as follows

$$\sum_{k=1}^{6}\sum_{l=1}^{6}\left(\hat{n}_{\mathcal{S}_{m,k}}\times\hat{x}\right)\cdot\left(\hat{n}_{\mathcal{S}_{n,l}}\times\hat{y}\right)I_{mn}^{kl} \tag{C.36}$$

where the straightforward calculation of the products $\left(\hat{n}_{\mathcal{S}_{m,k}} \times \hat{x}\right) \cdot \left(\hat{n}_{\mathcal{S}_{n,l}} \times \hat{y}\right)$ is summarized in the following table

$$\begin{array}{r|cccccc} & \hat{x} & -\hat{x} & \hat{y} & -\hat{y} & \hat{z} & -\hat{z} \\ \hline \hat{x} & 0 & 0 & 0 & 0 & 0 & 0 \\ -\hat{x} & 0 & 0 & 0 & 0 & 0 & 0 \\ \hat{y} & -1 & 1 & 0 & 0 & 0 & 0 \\ -\hat{y} & 1 & -1 & 0 & 0 & 0 & 0 \\ \hat{z} & 0 & 0 & 0 & 0 & 0 & 0 \\ -\hat{z} & 0 & 0 & 0 & 0 & 0 & 0 \end{array} \tag{C.37}$$

resulting into nonzero values only for $\hat{n}_{\mathcal{S}_{m,k}} = \pm\hat{y}$ and $\hat{n}_{\mathcal{S}_{n,l}} = \pm\hat{x}$. Therefore (C.36) becomes as follows

$$-I_{mn}^{31} + I_{mn}^{32} + I_{mn}^{41} - I_{mn}^{42}. \tag{C.38}$$

When calculating all the entries of $\ddot{\mathbf{z}}_{xy}^{\cdot\mathrm{rad}}$, one can exploit the rotational and translational symmetries to reduce the number of integrals to perform.

C.3.3. The Calculation of the Matrix-Vector Products

Iterative solvers are the most viable option for the solution of large-scale problems. These require the computation of matrix-vector products in the form of (C.5) to obtain an approximate solution at each iteration.

The rightmost matrix vector product in its entire form can be decomposed as follows

$$\begin{bmatrix} \mathbf{Z}_{xx}^{\mathrm{rad}} & \mathbf{Z}_{xy}^{\mathrm{rad}} & \mathbf{Z}_{xz}^{\mathrm{rad}} \\ \mathbf{Z}_{xy}^{\mathrm{rad}} & \mathbf{Z}_{yy}^{\mathrm{rad}} & \mathbf{Z}_{yz}^{\mathrm{rad}} \\ \mathbf{Z}_{xz}^{\mathrm{rad}} & \mathbf{Z}_{yz}^{\mathrm{rad}} & \mathbf{Z}_{zz}^{\mathrm{rad}} \end{bmatrix} \begin{bmatrix} \mathbf{u}_x \\ \mathbf{u}_y \\ \mathbf{u}_z \end{bmatrix} = \begin{bmatrix} \mathbf{Z}_{xx}^{\mathrm{rad}} \\ \mathbf{Z}_{xy}^{\mathrm{rad}} \\ \mathbf{Z}_{xz}^{\mathrm{rad}} \end{bmatrix} \mathbf{u}_x + \begin{bmatrix} \mathbf{Z}_{xy}^{\mathrm{rad}} \\ \mathbf{Z}_{yy}^{\mathrm{rad}} \\ \mathbf{Z}_{yz}^{\mathrm{rad}} \end{bmatrix} \mathbf{u}_y + \begin{bmatrix} \mathbf{Z}_{xz}^{\mathrm{rad}} \\ \mathbf{Z}_{yz}^{\mathrm{rad}} \\ \mathbf{Z}_{zz}^{\mathrm{rad}} \end{bmatrix} \mathbf{u}_z \tag{C.39}$$

where the vectors $\mathbf{u}_x$, $\mathbf{u}_y$, and $\mathbf{u}_z$ contain the entries of the currents located in the x, y, and z oriented basis functions at the q-iteration. Being $\mathbf{Z}_{mn}^{\mathrm{rad}}$ a full matrix, its multiplication by $\mathbf{u}_m$ requires N^2 operations. However, thanks to the block Toeplitz form of the matrix, the computational burden of the product can be reduced with the use of the FFT, scaling the complexity to $\mathcal{O}(N \log_2 N)$. First, each of the currents has to be conveniently transformed into the following $(2N_x - 1) \times (2N_y - 1) \times (2N_z - 1)$ size tensor

$$\ddot{\mathbf{u}}_m^p = \left[\mathrm{reshape}\left(\mathbf{i}_m\right)_{N_x,N_y,N_z}, 0, \ldots, 0\right] \tag{C.40}$$

where the reshape operation rearranges the vector $\mathbf{u}_m$ into a three-dimensional tensor of size $N_x \times N_y \times N_z$, and a zero-padding is performed to bring it to the same size of any $\ddot{\mathbf{z}}_{mn}^{\cdot\mathrm{rad}}$ block. Then, the product is calculated for each block as follows

$$\left[\mathrm{IFFT}\left(\mathrm{FFT}\left(\ddot{\mathbf{z}}_{mn}^{\cdot\mathrm{rad}}\right) \odot \mathrm{FFT}\left(\ddot{\mathbf{u}}_m^{\cdot p}\right)\right)\right]_{N_x:2N_x-1,N_y:2N_y-1,N_z:2N_z-1} \tag{C.41}$$

where $\odot$ stands for the Hadamard product. Finally, the tensor resulting from the products of (C.41) can be reshaped into a vector. Due to the logarithmic number of operations of the FFT and IFFT, the complexity of (C.39) is scaled from $\mathcal{O}\left(N^2\right)$ to $\mathcal{O}(N \log_2 N)$.

Finally, the multiplications by the diagonal matrix $\mathbf{Z}^{\text{mat}}$ have to be treated. The product can be simply seen as an element-wise scaling of all the entries.

These alternative ways to perform the products of (C.5) can be embedded in the operations of any iterative solver [207, 208], allowing for the reduction of the computational complexity and relaxing the memory requirements, thanks to the smart storage described in Subsection C.3.1.

C.4. The Calculation of the Input Impedance

Considering a dipole oriented along x, having a feeding gap δ long, and a cross section A, the input impedance, when considering continuous quantities, is calculated as follows

$$Z_{\text{in}} = \frac{\frac{1}{A}\iint_A \int_\delta \vec{E} \cdot \hat{x} dV}{\iint_A \vec{J} \cdot \hat{x} dA}. \tag{C.42}$$

When the numerical solution is taken into account, considering a gap and a cross section comprising N_{gap} and N_{cross} cells, with an amplitude excitation v for every cell, the input impedance is calculated as follows

$$Z_{\text{in}} = \frac{N_{\text{gap}} v}{\frac{1}{N_{\text{gap}}} \sum_{j=1}^{N_{\text{gap}}} \sum_{h=1}^{N_{\text{cross}}} i_{jh}} \tag{C.43}$$

where i_{jh} are the currents associated with the x-component of the solution.

Appendix D

Semi-analytical Evaluation of the Transverse Green's Function

D.1. Expression of the Voltage Wave Solution in Layered Media

In the transmission line equivalent problem of Fig. 6.1(c), with the positive z-axis oriented upwards and the unitary current source located at z', the voltage solution at $z \in [t_1;\ t_2]$ can be expressed as the sum of two terms. One models the propagation in an infinite transmission line with characteristic impedance Z_{0i} and propagation constant k_{zi}, while the other one accounts for the reflections given by the discontinuities at $z = t_1$ and $z = t_2$.

This problem can be simplified with the transmission line sketched in Fig. D.1(a), where the loads Z_{L1} and Z_{L2} are the impedances seen at $z = t_1$ and $z = t_2$, looking downwards and upwards, respectively. The voltage at z is given by the following expressions

$$v_1(z) = V_1^+ e^{jk_{zi}z}\left(1 + \Gamma_{L1} e^{j2k_{zi}(t_1 - z)}\right) \tag{D.1}$$

$$v_2(z) = V_2^+ e^{-jk_{zi}z}\left(1 + \Gamma_{L2} e^{-j2k_{zi}(t_2 - z)}\right) \tag{D.2}$$

where 1 and 2 denote the section below and above the source, respectively, and

$$\Gamma_{L1} = \frac{Z_{L1} - Z_{0i}}{Z_{L1} + Z_{0i}} \tag{D.3}$$

$$\Gamma_{L2} = \frac{Z_{L2} - Z_{0i}}{Z_{L2} + Z_{0i}} \tag{D.4}$$

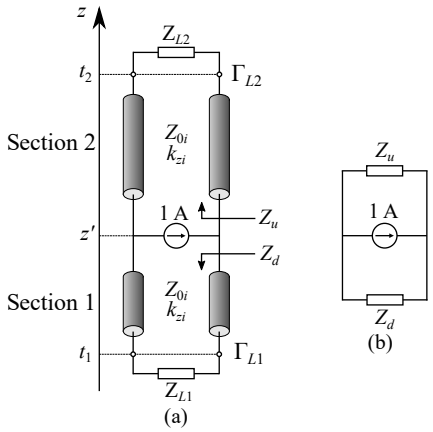

Figure D.1: (a) Transmission line circuit. (b) Lumped element circuit.

are the reflection coefficients between the loads Z_{L1} and Z_{L2} and the line, calculated at $z = t_1$ and $z = t_2$, respectively.

By enforcing the voltage at z' to be equal to the input impedance Z_{in} multiplied by the 1 A excitation, one can derive the following expressions for V_1^+ and V_2^+

$$V_1^+ = Z_{\mathrm{in}} \frac{e^{-jk_{zi}z'}}{1 + \Gamma_{L1} e^{j2k_{zi}(t_1 - z')}} \tag{D.5}$$

$$V_2^+ = Z_{\mathrm{in}} \frac{e^{jk_{zi}z'}}{1 + \Gamma_{L2} e^{-j2k_{zi}(t_2 - z')}} \tag{D.6}$$

which yield to the following expressions for $v_1(z)$ $v_2(z)$

$$v_1(z) = Z_{\mathrm{in}} \frac{1 + \Gamma_{L1} e^{j2k_{zi}(t_1 - z)}}{1 + \Gamma_{L1} e^{j2k_{zi}(t_1 - z')}} e^{jk_{zi}(z - z')} \tag{D.7}$$

$$v_2(z) = Z_{\mathrm{in}} \frac{1 + \Gamma_{L2} e^{-j2k_{zi}(t_2 - z)}}{1 + \Gamma_{L2} e^{-j2k_{zi}(t_2 - z')}} e^{-jk_{zi}(z - z')} \tag{D.8}$$

The input impedance Z_{in} is the parallel between Z_u and Z_d, i.e., the impedances seen at z'_+ upwards and z'_- downwards, respectively, as shown in Fig. D.1(b). The impedances Z_d and Z_u can be expressed as follows

$$Z_d = Z_{0i} \frac{1 + \Gamma_{L1} e^{j2k_{zi}(t_1 - z')}}{1 - \Gamma_{L1} e^{j2k_{zi}(t_1 - z')}} \tag{D.9}$$

$$Z_u = Z_{0i} \frac{1 + \Gamma_{L2} e^{-j2k_{zi}(t_2 - z')}}{1 - \Gamma_{L2} e^{-j2k_{zi}(t_2 - z')}} \tag{D.10}$$

which allow us to calculate Z_{in} as their parallel as follows

$$Z_{\text{in}} = \frac{Z_{0i}}{2} \frac{\left(1+\Gamma_{L2} e^{-j2k_{zi}\left(t_2-z'\right)}\right)\left(1+\Gamma_{L1} e^{j2k_{zi}\left(t_1-z'\right)}\right)}{1-\Gamma_{L1}\Gamma_{L2} e^{-j2k_{zi}(t_2-t_1)}}. \tag{D.11}$$

By using (D.11) in (D.7) and (D.8), one obtains the following expressions

$$v_1(z) = \frac{Z_{0i}}{2} \frac{\left(1+\Gamma_{L1} e^{j2k_{zi}(t_1-z)}\right)\left(1+\Gamma_{L2} e^{-j2k_{zi}\left(t_2-z'\right)}\right)}{1-\Gamma_{L1}\Gamma_{L2} e^{-j2k_{zi}(t_2-t_1)}} e^{jk_{zi}\left(z-z'\right)} \tag{D.12}$$

$$v_2(z) = \frac{Z_{0i}}{2} \frac{\left(1+\Gamma_{L1} e^{j2k_{zi}\left(t_1-z'\right)}\right)\left(1+\Gamma_{L2} e^{-j2k_{zi}(t_2-z)}\right)}{1-\Gamma_{L1}\Gamma_{L2} e^{-j2k_{zi}(t_2-t_1)}} e^{-jk_{zi}\left(z-z'\right)}. \tag{D.13}$$

By calculating the products in (D.12) and (D.13), one can write the following voltage expression,

$$v_1(z) = \frac{Z_{0i}}{2}\left(e^{jk_{zi}\left(z-z'\right)} + Q\left(z,z'\right)\right) \tag{D.14}$$

$$v_2(z) = \frac{Z_{0i}}{2}\left(e^{-jk_{zi}\left(z-z'\right)} + Q\left(z,z'\right)\right) \tag{D.15}$$

where

$$Q\left(z,z'\right) = \frac{\Gamma_{L2} e^{-jk_{zi}\left(2t_2-z-z'\right)} + \Gamma_{L1} e^{-jk_{zi}\left(z+z'-2t_1\right)}}{1-\Gamma_{L1}\Gamma_{L2} e^{-j2k_{zi}(t_2-t_1)}} + \frac{2\Gamma_{L1}\Gamma_{L2} e^{-j2k_{zi}(t_2-t_1)}\cos[k_{zi}(z-z')]}{1-\Gamma_{L1}\Gamma_{L2} e^{-j2k_{zi}(t_2-t_1)}}. \tag{D.16}$$

Therefore, one can write the following expression which is valid in either Section 1 and Section 2

$$v(z) = \frac{Z_{0i}}{2}\left(e^{-jk_{zi}|z-z'|} + Q\left(z,z'\right)\right). \tag{D.17}$$

D.2. Analytical Calculation of the Integrals in Space

In this section, we exploit the formulation for the voltage wave solution in the source region [168, eq. 72] as described in Section D.1 to have calculate analytically the integrals in z and z' of (6.14). The potentials in (6.7) can be split as in [168, eq. 72] (or (D.17) of this dissertation), allowing to separate the propagation in an unbounded

medium from the reflections, i.e., $Q(z,z')$. This allows us to write the Green's function as follows

$$G_{xx}^{\mathrm{EJ}}(k_x,k_y,z,z') = -\frac{1}{2}\frac{Z_{0i}^{\mathrm{TM}}\left(e^{-jk_{zi}|z-z'|}+Q^{\mathrm{TM}}(z,z')\right)k_x^2}{k_x^2+k_y^2} - \frac{1}{2}\frac{Z_{0i}^{\mathrm{TE}}\left(e^{-jk_{zi}|z-z'|}+Q^{\mathrm{TE}}(z,z')\right)k_y^2}{k_x^2+k_y^2} \quad \text{(D.18)}$$

and allowing us to split (6.14) into one integral for the unbounded medium and one integral for the reflections for both the TE and the TM mode. As the integrals for the unbounded medium and the reflections are essentially the same for the TE and TM, the solutions shown in this document are grouped in two classes.

The formulas presented here are referred to the current distribution (6.26) but can be easily extended to the two-flows formulation of (6.17) and (6.18).

D.2.1. Unbounded Medium

The term associated with the unbounded medium is written as follows for the TE and the TM case

$$-\frac{A}{4\pi}Z_{0i}^{\mathrm{TE/TM}}\int_{-\infty}^{+\infty}\frac{J_{tym}(k_y)\,\tilde{J}_{tyn}(-k_y)}{k_x^2+k_y^2}k_i^2\left[\int_0^{w_z}\int_0^{w_z}\left(Re^{-\frac{1+j}{\delta_p}z'}+e^{\frac{1+j}{\delta_p}(z'-w_z)}\right)\times\left(R^*e^{-\frac{1-j}{\delta_p}z}+e^{\frac{1-j}{\delta_p}(z-w_z)}\right)e^{-jk_{zi}|z-z'|}dzdz'\right]dk_y \quad \text{(D.19)}$$

with $i=\{x,y\}$ for TE and TM, respectively, and A the square of the normalization factor of (6.26). The integrals in z and z' are calculated analytically, while the remaining integral in k_y is calculated numerically. The space domain integrals are calculated with the following expression

$$\int_0^{w_z}\int_0^{w_z}\left(Re^{-\frac{1+j}{\delta_p}z'}+e^{\frac{1+j}{\delta_p}(z'-w_z)}\right)\left(R^*e^{-\frac{1-j}{\delta_p}z}+e^{\frac{1-j}{\delta_p}(z-w_z)}\right)e^{-jk_{zi}|z-z'|}dzdz' = I_1^{fs}+I_2^{fs}+I_3^{fs}+I_4^{fs}+I_5^{fs}+I_6^{fs} \quad \text{(D.20)}$$

where

$$I_1^{fs} = -\frac{\delta_p^2}{1-j(\delta_p k_{zi}+1)}\left\{(R^2+1)\left(1-e^{-\frac{2w_z}{\delta_p}}\right)-e^{-\frac{w_z}{\delta_p}}\,\mathrm{Im}\left[Re^{j\frac{w_z}{\delta_p}}\left(e^{-j\frac{2w_z}{\delta_p}}-1\right)\right]\right\}$$

$$I_2^{fs} = \frac{\delta_p^2\left(R^2+1\right)}{\left(k_{zi}\delta_p+1\right)^2+1}\left[1-e^{-w_z\left(jk_{zi}+\frac{1+j}{\delta_p}\right)}\right]$$

$$I_3^{fs} = 2\delta_p^2\frac{e^{-w_z\frac{1+j}{\delta_p}}-e^{-jk_{zi}w_z}}{k_{zi}^2\delta_p^2-2+2jk_{zi}\delta_p}\,\mathrm{Re}\left[R\right]$$

$$I_4^{fs} = \frac{\delta_p^2}{2}\frac{1}{1+j\left(k_{zi}\delta_p-1\right)}\Bigg\{2e^{-\frac{w_z}{\delta_p}}\,\mathrm{Im}\left[Re^{j\frac{w_z}{\delta_p}}\left(1-e^{-j\frac{2w_z}{\delta_p}}\right)\right] + \left(1-e^{-\frac{2w_z}{\delta_p}}\right)\left(R^2+1\right)\Bigg\}$$

$$I_5^{fs} = \frac{\delta_p^2\left(R^2+1\right)}{\left(k_{zi}\delta_p-1\right)^2+1}\left(e^{-\frac{2w_z}{\delta_p}}-e^{-w_z\left(jk_{zi}+\frac{1-j}{\delta_p}\right)}\right)$$

$$I_6^{fs} = 2\delta_p^2\frac{e^{-w_z\frac{1-j}{\delta_p}}-e^{-\frac{2w_z}{\delta_p}}e^{-jk_{zi}w_z}}{k_{zi}^2\delta_p^2-2-2jk_{zi}\delta_p}\,\mathrm{Re}\left[R\right]$$

D.2.2. Reflections

As for the term involving the propagation in an unbounded medium, the reflections are taken into account with the following integrals

$$-\frac{AZ_{0i}^{\mathrm{TE/TM}}}{4\pi}\int_{-\infty}^{+\infty}\frac{J_{tym}\left(k_y\right)\tilde{J}_{tyn}\left(-k_y\right)}{k_x^2+k_y^2}k_i^2\Bigg[\int_0^{w_z}\int_0^{w_z}\left(Re^{-\frac{1+j}{\delta_p}z}+e^{\frac{1+j}{\delta_p}(z-w_z)}\right) \times\left(R^*e^{-\frac{1-j}{\delta_p}z}+e^{\frac{1-j}{\delta_p}(z-w_z)}\right)Q^{\mathrm{TE/TM}}\left(z,z'\right)dzdz'\Bigg]dk_y \quad \text{(D.21)}$$

where $Q^{\mathrm{TE/TM}}\left(z,z'\right)$ is the reflection term defined in (D.16), where the reflection coefficients are calculated for the TE or TM case. As previously done, the space integral can be split as follows

$$\int_0^{w_z}\int_0^{w_z}\left(Re^{-\frac{1+j}{\delta_p}z}+e^{\frac{1+j}{\delta_p}(z-w_z)}\right)\left(R^*e^{-\frac{1-j}{\delta_p}z}+e^{\frac{1-j}{\delta_p}(z-w_z)}\right)Q^{\mathrm{TE/TM}}\left(z,z'\right)dzdz' = I_1^Q+I_2^Q+I_3^Q+I_4^Q \quad \text{(D.22)}$$

D

$$I_1^Q = \frac{\delta_p^2 e^{jk_{zi}2t_1}\Gamma_1^{\mathrm{TE/TM}}}{1-\Gamma_1^{\mathrm{TE/TM}}\Gamma_2^{\mathrm{TE/TM}}e^{-2jk_{zi}(t_2-t_1)}}\left(R\frac{1-e^{-w_z\left(jk_{zi}+\frac{1+j}{\delta_p}\right)}}{jk_{zi}\delta_p+1+j}\right.$$
$$\left.+\frac{e^{-w_z\frac{1+j}{\delta_p}}-e^{-jk_{zi}w_z}}{jk_{zi}\delta_p-1-j}\right)\left(R^*\frac{1-e^{-w_z\left(jk_{zi}+\frac{1-j}{\delta_p}\right)}}{jk_{zi}\delta_p+1-j}+\frac{e^{-w_z\frac{1-j}{\delta_p}}-e^{-jk_{zi}w_z}}{jk_{zi}\delta_p-1+j}\right)$$

$$I_2^Q = \frac{\delta_p^2 e^{-jk_{zi}2t_2}\Gamma_2^{\mathrm{TE/TM}}}{1-\Gamma_1^{\mathrm{TE/TM}}\Gamma_2^{\mathrm{TE/TM}}e^{-2jk_{zi}(t_2-t_1)}}\left(R\frac{e^{w_z\left(jk_{zi}-\frac{1+j}{\delta_p}\right)}-1}{jk_{zi}\delta_p-1-j}\right.$$
$$\left.+\frac{e^{jk_{zi}w_z}-e^{-w_z\frac{1+j}{\delta_p}}}{jk_{zi}\delta_p+1+j}\right)\left(R^*\frac{e^{w_z\left(jk_{zi}-\frac{1-j}{\delta_p}\right)}-1}{jk_{zi}\delta_p-1+j}+\frac{e^{jk_{zi}w_z}-e^{-w_z\frac{1-j}{\delta_p}}}{jk_{zi}\delta_p+1-j}\right)$$

$$I_3^Q = \frac{\delta_p^2 e^{-2jk_{zi}(t_2-t_1)}\Gamma_1^{\mathrm{TE/TM}}\Gamma_2^{\mathrm{TE/TM}}}{1-\Gamma_1^{\mathrm{TE/TM}}\Gamma_2^{\mathrm{TE/TM}}e^{-2jk_{zi}(t_2-t_1)}}\left[\left(R\frac{1-e^{w_z\left(jk_{zi}+\frac{1+j}{\delta_p}\right)}}{jk_{zi}\delta_p+1+j}\right.\right.$$
$$\left.\left.+\frac{e^{-w_z\frac{1+j}{\delta_p}}-e^{-jk_{zi}w_z}}{jk_{zi}\delta_p-1-j}\right)\left(R^*\frac{e^{w_z\left(jk_{zi}-\frac{1-j}{\delta_p}\right)}-1}{jk_{zi}\delta_p-1+j}+\frac{e^{jk_{zi}w_z}-e^{-w_z\frac{1-j}{\delta_p}}}{jk_{zi}\delta_p+1-j}\right)\right]$$

$$I_4^Q = \frac{\delta_p^2 e^{-2jk_{zi}(t_2-t_1)}\Gamma_1^{\mathrm{TE/TM}}\Gamma_2^{\mathrm{TE/TM}}}{1-\Gamma_1^{\mathrm{TE/TM}}\Gamma_2^{\mathrm{TE/TM}}e^{-2jk_{zi}(t_2-t_1)}}\left[\left(R\frac{e^{w_z\left(jk_{zi}-\frac{1+j}{\delta_p}\right)}-1}{jk_{zi}\delta_p-1-j}\right.\right.$$
$$\left.\left.+\frac{e^{jk_{zi}w_z}-e^{-w_z\frac{1+j}{\delta_p}}}{jk_{zi}\delta_p+1+j}\right)\left(R^*\frac{1-e^{-w_z\left(jk_{zi}+\frac{1-j}{\delta_p}\right)}}{jk_{zi}\delta_p+1-j}+\frac{e^{-w_z\frac{1-j}{\delta_p}}-e^{-jk_{zi}w_z}}{jk_{zi}\delta_p-1+j}\right)\right].$$

Appendix E

Study on the Current Spectrum of an Infinitely Long Dipole

E.1. Dynamic Current Space Distribution

Given the expression of the spectrum of the dynamic current (6.31), its space domain expression can be conveniently written as follows

$$i_{\mathrm{dyn}}(x) = f(x) * \frac{1}{\Delta}\,\mathrm{rect}\left(\frac{x}{\Delta}\right) = \frac{1}{\Delta}\int_{-\Delta/2}^{\Delta/2} f(x-x')\,dx' \tag{E.1}$$

where f is a function to be determined, whose spectrum is defined in (6.31), and which can be calculated with the following inverse Fourier transform

$$f(x) = \frac{1}{2\pi}\int_{-\infty}^{+\infty} \frac{2k_{xp}}{D'(k_{xp})(k_x - k_{xp})(k_x + k_{xp})} e^{-jk_x x} dk_x. \tag{E.2}$$

The considerations regarding the integral (E.2) are the same for (6.29). However, as we want do derive an analytical expression for f, both $x < 0$ and $x > 0$ must be considered. By combining the expressions resulting from the two conditions, one obtains $f(x)$ as follows

$$f(x) = -j\frac{e^{-jk_{xp}|x|}}{D'(k_{xp})} \tag{E.3}$$

which is a single expression valid for every value of x.

Consequently, one can calculate the dynamic current as follows

$$i_{\mathrm{dyn}}(x) = -\frac{j}{\Delta D'(k_{xp})} \int_{-\Delta/2}^{\Delta/2} e^{-jk_{xp}|x-x'|} dx' \tag{E.4}$$

where, due to the absolute value at the exponent, different approaches have to be used.

If $x < -\Delta/2$ or $x > \Delta/2$, (E.4) is written as follows

$$-\frac{je^{\mp jk_{xp}x}}{\Delta D'(k_{xp})} \int_{-\Delta/2}^{\Delta/2} e^{\pm jk_{xp}x'} dx' \tag{E.5}$$

where the choice of the signs at the exponent is for $x > \Delta/2$ and $x < -\Delta/2$, respectively, and by calculating the integral, one finds the expression (6.32).

If $-\Delta/2 < x < \Delta/2$, one can define the change of variable $x'' = x - x'$, write (E.4) as follows

$$-\frac{j}{\Delta D'(k_{xp})} \int_{x-\Delta/2}^{x+\Delta/2} e^{-jk_{xp}|x''|} dx'' \tag{E.6}$$

and expand the absolute value as follows

$$-\frac{j}{\Delta D'(k_{xp})} \left(\int_{x-\Delta/2}^{0} e^{jk_{xp}x''} dx'' + \int_{0}^{x+\Delta/2} e^{-jk_{xp}x''} dx'' \right) \tag{E.7}$$

and finally, by integration, one obtains the expression (6.33).

E.2. Asymptotic Transverse Green's Function

By recalling the definition of the sinc function

$$\mathrm{sinc}\left(\frac{k_y w_y}{2}\right) = \frac{1}{w_y} \int_{-w_y/2}^{w_y/2} e^{jk_y y} dy \tag{E.8}$$

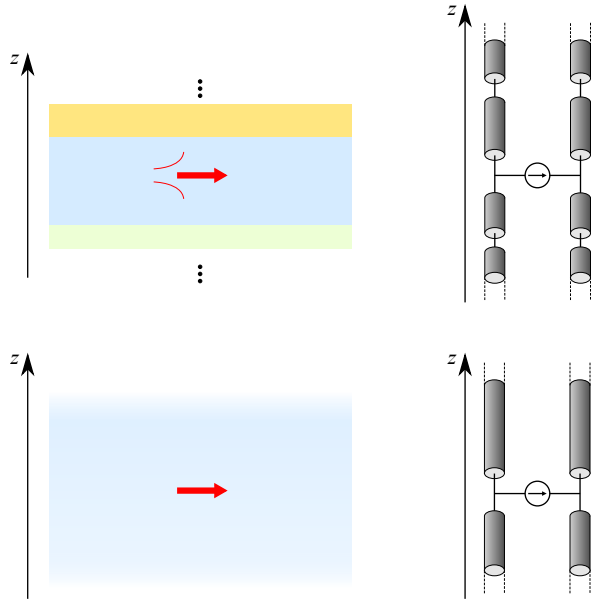

Figure E.1: Sketch of cut-off modes propagating in stratified media and their equivalent propagation in an homogeneous medium.

the integral between $-w_y/2$ and $w_y/2$ can be written as the superposition of three contributions as follows

$$\frac{1}{w_y}\left(\int_{-\infty}^{+\infty} e^{jk_y y}dy - \int_{-\infty}^{-w_y/2} e^{jk_y y}dy - \int_{w_y/2}^{+\infty} e^{jk_y y}dy\right). \tag{E.9}$$

By substituting (E.9) into (6.14), one obtains the following expression

$$D(k_x) = D_0 + D_1(k_x) + D_2(k_x) \tag{E.10}$$

where

$$D_0 = \rho\langle j_t, \tilde{j}_t\rangle_A \tag{E.11}$$

$$D_1(k_x) = -\frac{J_{t,y}(0)}{w_y}\int_0^{w_z}\int_0^{w_z} G_{xx}^{EJ}(k_x, 0, z, z')j_{t,z}(z')\tilde{j}_{t,z}^*(z)\,dzdz' \tag{E.12}$$

$$D_2(k_x) = \frac{1}{2\pi w_y} \int_{C_\infty} \left[\int_0^{w_z} \int_0^{w_z} \left(\int_{-\infty}^{+\infty} G_{xx}^{EJ}(k_x, k_y, z, z') \times J_{t,y}(k_y)\, e^{jk_y y} dk_y \right) j_{t,z}(z')\, \tilde{j}_{t,z}^{*}(z)\, dz dz' \right] dy \quad \text{(E.13)}$$

with $C_\infty = [-\infty, -w_y/2] \cup [w_y/2, +\infty]$. For large values of k_x, k_z has a large imaginary part, making the propagation along z strongly attenuated. Therefore the contributions of the reflections are negligible, and the source can be represented as to be radiating in an homogeneous medium, as shown in Fig. E.1. The integral between the round brackets in (E.13) can be written in the following form

$$\left(k^2 - k_x^2\right) \int_{-\infty}^{+\infty} \frac{J_0\left(k_y w_y/2\right)}{\sqrt{k^2 - k_x^2 - k_y^2}} e^{jk_y y'} dk_y \quad \text{(E.14)}$$

where J_0 is the first-kind zeroth-order Bessel function and the homogeneous space Green's function has been used. The solution of (E.14) can be seen as the field radiated at $y' \in C_\infty$ by lines of current located between $-w_y/2$ and $w_y/2$ and having the profile of j_{ty}, having expression

$$\pi \left(k^2 - k_x^2\right) H_0^{(2)} \left(\sqrt{k^2 - k_x^2}|y'|\right) * j_{ty}(y') \quad \text{(E.15)}$$

where $H_0^{(2)}$ is the second kind zeroth order Hankel function. For $k_x \to \infty$, the Hankel function represents a spatial decay, which can be made arbitrarily small. Therefore, the contribution of (E.13) results negligible with respect to (E.11) and (E.12).

E.3. Calculation of the Dynamic Admittance

The dynamic admittance Y_{dyn} is defined with the spectral domain integral (6.35) and due to its integrand function can be expressed – in a similar fashion as (E.1) – with the following space integrals

$$Y_{\text{dyn}} = \frac{1}{\Delta^2} \int_{-\Delta/2}^{\Delta/2} \int_{-\Delta/2}^{\Delta/2} f(x - x')\, dx dx' \quad \text{(E.16)}$$

where the function f is the same as (E.3), and which allows us to express Y_{dyn} as follows

$$Y_{\text{dyn}} = -\frac{j}{D'\left(k_{xp}\right)\Delta^2} \int_{-\Delta/2}^{\Delta/2} \left(\int_{-\Delta/2}^{\Delta/2} e^{-jk_{xp}|x-x'|} dx' \right) dx. \tag{E.17}$$

The integral in brackets can be calculated as in (E.7), which results into (6.33), allowing us to calculate the dynamic admittance with the following single integral

$$-\frac{2}{D'\left(k_{xp}\right)\Delta k_{xp}} \int_{-\Delta/2}^{\Delta/2} \left(1-\cos(k_{xp}x)e^{-jk_{xp}\Delta/2}\right) dx \tag{E.18}$$

which can be closed into the following expression

$$\frac{2}{D'\left(k_{xp}\right)\Delta k_{xp}} \left(e^{-jk_{xp}\Delta/2}\,\text{sinc}\left(k_{xp}\Delta/2\right) - 1\right). \tag{E.19}$$

By expanding the complex exponential in (E.19) into sine and cosine, and by using the identity $\cos\left(x\right)\text{sinc}\left(x\right) = \text{sinc}\left(2x\right)$, (E.19) can be rewritten as follows

$$\frac{2\left(\text{sinc}\left(k_{xp}\Delta\right) - 1\right)}{\Delta k_{xp} D'\left(k_{xp}\right)} - \frac{j}{D'\left(k_{xp}\right)} \text{sinc}^2\left(\frac{k_{xp}\Delta}{2}\right) \tag{E.20}$$

which yields (6.36), (6.37), and (6.38).

Bibliography

[1] "Huawei 5G wireless network planning solution white paper," Huawei, White Paper, 2018. [Online]. Available: https://tinyurl.com/9vx94yxr

[2] "5G wireless access: an overview," Ericsson, White Paper, 2020. [Online]. Available: https://tinyurl.com/yc7pvtcy

[3] "6G: The next horizon white paper," Huawei, White Paper, 2022. [Online]. Available: https://tinyurl.com/pyx5s79a

[4] "6G – connecting a cyber-physical world," Ericsson, White Paper, 2022. [Online]. Available: https://tinyurl.com/5me9p8th

[5] X. Lin, J. Zhang, Y. Liu, and J. Kim, *Fundamentals of 6G communications and networking*. Cham, Switzerland: Springer, 2024.

[6] F. Grijpink, E. Kutcher, A. Ménard, S. Ramaswamy, D. Schiavotto, J. Manyika, M. Chui, R. Hamill, and E. Okan, "Connected world: An evolution in connectivity beyond the 5G revolution," McKinsey & Company, Tech. Rep., Feb. 2020. [Online]. Available: https://tinyurl.com/ychm8uy8

[7] S. Bandyopadhyay, P. Jain, J. Leing, and S. Prisacaru, "Navigating the three horizons of 5G business building," McKinsey & Company, Tech. Rep., Feb. 2024. [Online]. Available: https://tinyurl.com/bdednx7v

[8] Sustainable development goals. United Nations. [Online]. Available: https://sdgs.un.org/goals

[9] F. Boccardi, R. W. Heath, A. Lozano, T. L. Marzetta, and P. Popovski, "Five disruptive technology directions for 5G," *IEEE Commun. Mag.*, vol. 52, no. 2, pp. 74–80, Feb. 2014.

[10] J. G. Andrews, S. Buzzi, W. Choi, S. V. Hanly, A. Lozano, A. C. K. Soong, and J. C. Zhang, "What will 5G be?" *IEEE J. Sel. Areas Commun.*, vol. 32, no. 6, pp. 1065–1082, Jun. 2014.

[11] R. W. Heath, N. González-Prelcic, S. Rangan, W. Roh, and A. M. Sayeed, "An overview of signal processing techniques for millimeter wave mimo systems," *J. Sel. Topics Signal Process.*, vol. 10, no. 3, pp. 436–453, Apr. 2016.

[12] K. Kibaroglu, M. Sayginer, and G. M. Rebeiz, "A low-cost scalable 32-element 28-GHz phased array transceiver for 5G communication links based on a 2×2 beamformer flip-chip unit cell," *IEEE J. Solid-State Circuits*, vol. 53, no. 5, pp. 1260–1274, May 2018.

[13] K. Kibaroglu, M. Sayginer, T. Phelps, and G. M. Rebeiz, "A 64-element 28-GHz phased-array transceiver with 52-dBm EIRP and 8–12-Gb/s 5G link at 300 meters without any calibration," *IEEE Trans. Microw. Theory Techn.*, vol. 66, no. 12, pp. 5796–5811, Dec. 2018.

[14] A. A. Farid, A. S. H. Ahmed, A. Dhananjay, and M. J. W. Rodwell, "A fully packaged 135-GHz multiuser mimo transmitter array tile for wireless communications," *IEEE Trans. Microw. Theory Techn.*, vol. 70, no. 7, pp. 3396–3405, Jul. 2022.

[15] A. Bisognin, N. Nachabe, C. Luxey, F. Gianesello, D. Gloria, J. R. Costa, C. A. Fernandes, Y. Alvarez, A. Arboleya-Arboleya, J. Laviada, F. Las-Heras, N. Dolatsha, B. Grave, M. Sawaby, and A. Arbabian, "Ball grid array module with integrated shaped lens for 5G backhaul/fronthaul communications in F-band," *IEEE Trans. Antennas Propag.*, vol. 65, no. 12, pp. 6380–6394, Dec. 2017.

[16] T. S. Rappaport, F. Gutierrez, E. Ben-Dor, J. N. Murdock, Y. Qiao, and J. I. Tamir, "Broadband millimeter-wave propagation measurements and models using adaptive-beam antennas for outdoor urban cellular communications," *IEEE Trans. Antennas Propag.*, vol. 61, no. 4, pp. 1850–1859, Apr. 2013.

[17] T. S. Rappaport, Y. Xing, G. R. MacCartney, A. F. Molisch, E. Mellios, and J. Zhang, "Overview of millimeter wave communications for fifth-generation (5G) wireless networks—with a focus on propagation models," *IEEE Trans. Antennas Propag.*, vol. 65, no. 12, pp. 6213–6230, Dec. 2017.

[18] W. Hong, Z. H. Jiang, C. Yu, J. Zhou, P. Chen, Z. Yu, H. Zhang, B. Yang, X. Pang, M. Jiang, Y. Cheng, M. K. T. Al-Nuaimi, Y. Zhang, J. Chen, and S. He, "Multibeam antenna technologies for 5G wireless communications," *IEEE Trans. Antennas Propag.*, vol. 65, no. 12, pp. 6231–6249, Dec. 2017.

[19] W. Hong, K.-H. Baek, and S. Ko, "Millimeter-wave 5G antennas for smartphones: Overview and experimental demonstration," *IEEE Trans. Antennas Propag.*, vol. 65, no. 12, pp. 6250–6261, Dec. 2017.

[20] M. Arias Campo, D. Blanco, S. Bruni, A. Neto, and N. Llombart, "On the use of fly's eye lenses with leaky-wave feeds for wideband communications," *IEEE Trans. Antennas Propag.*, vol. 68, no. 4, pp. 2480–2493, Apr. 2020.

[21] O. Quevedo-Teruel, J. Miao, M. Mattsson, A. Algaba-Brazalez, M. Johansson, and L. Manholm, "Glide-symmetric fully metallic Luneburg lens for 5G communications at Ka-band," *IEEE Antennas Wirel. Propag. Lett.*, vol. 17, no. 9, pp. 1588–1592, 2018.

[22] O. Zetterstrom, J. Rico-Fernández, J. L. Gómez-Tornero, and A. Algaba-Brazález, "Industrial evolution of lens antennas towards 6G radio access applications," *IEEE Antennas Wirel. Propag. Lett.*, pp. 1–5, 2024.

[23] E. Martini and S. Maci, "Theory, analysis, and design of metasurfaces for smart radio environments," *Proc. IEEE*, vol. 110, no. 9, pp. 1227–1243, Sep. 2022.

[24] Y. J. Guo, M. Ansari, R. W. Ziolkowski, and N. J. G. Fonseca, "Quasi-optical multi-beam antenna technologies for B5G and 6G mmwave and THz networks: A review," *IEEE Open J. Antennas Propag.*, vol. 2, pp. 807–830, 2021.

[25] J. Ruiz-García, E. Martini, C. della Giovampaola, D. González-Ovejero, and S. Maci, "Reflecting luneburg lenses," *IEEE Trans. Antennas Propag.*, vol. 69, no. 7, pp. 3924–3935, Jul. 2021.

[26] N. Llombart and S. O. Dabironezare, "Feasibility study of quasi-optical MIMO antennas for radiative near-field links," *IEEE Trans. Antennas Propag.*, vol. 70, no. 8, pp. 7073–7083, Aug. 2022.

[27] M. Ettorre and D. Gonzalez-Ovejero, "High speed and resilient wireless interconnects in the near field," in *Proc. Intern. Workshop Antenna Technol.*, Aalborg, Denmark, May 15-17 2023.

[28] 3GPP, "New frequency range for NR (24.25-29.5 GHz)," 3rd Generation Partnership Project, Valbonne, France, Tech. Rep. 38.815, Sep. 2021. [Online]. Available: https://www.3gpp.org/ftp/Specs/archive/38_series/38.815/

[29] ——, "New frequency range for NR (39.5 - 43.5 GHz)," 3rd Generation Partnership Project, Valbonne, France, Tech. Rep. 38.887, Jun. 2020. [Online]. Available: https://www.3gpp.org/ftp/Specs/archive/38_series/38.887/

[30] ETSI, "User equipment (UE) radio transmission and reception; part 1: Range 1 standalone," European Telecommunications Standards Institute, Sophia Antipolis, France, Tech. Spec. 38.887, Feb. 2024. [Online]. Available: https://tinyurl.com/bbjmbk4t

[31] N. Llombart, D. Emer, M. Arias Campo, and E. McCune, "Fly's eye spherical antenna system for future Tbps wireless communications," in *Proc. Eur. Conf. Antennas Propag.*, Paris, France, Mar. 19-24 2017.

[32] Ericsson, "Breaking the 100Gbps barrier," Ericsson, Stockholm, Sweden, Extract Ericsson Microw. Outlook Rep. EAB-17:014270 Uen, 2019. [Online]. Available: https://tinyurl.com/yfxm27rs

[33] H. Zhang, S. Bosma, A. Neto, and N. Llombart, "A dual-polarized 27 dBi scanning lens phased array antenna for 5G point-to-point communications," *IEEE Trans. Antennas Propag.*, vol. 69, no. 9, p. 5640–5652, Sep. 2021.

[34] J. Ala-Laurinaho, J. Aurinsalo, A. Karttunen, M. Kaunisto, A. Lamminen, J. Nurmiharju, A. V. Räisänen, J. Säily, and P. Wainio, "2-D beam-steerable integrated lens antenna system for 5G *E*-band access and backhaul," *IEEE Trans. Microw. Theory Techn.*, vol. 64, no. 7, pp. 2244–2255, Jul. 2016.

[35] J. L. González-Jiménez, F. Foglia Manzillo, A. Hamani, A. Siligaris, N. Cassiau, A. Clemente, P. Courouve, F. Chaix, and C. Dehos, "A D-band transmitter achieving 57.6-Gb/s and 30-dBm EIRP based on channel-aggregation 45-Nm ICs and a low-profile flat lens antenna," *IEEE Trans. Microw. Theory Techn.*, vol. 72, no. 1, pp. 836–850, Jan. 2024.

[36] E. Basar, M. Di Renzo, J. De Rosny, M. Debbah, M.-S. Alouini, and R. Zhang, "Wireless communications through reconfigurable intelligent surfaces," *IEEE Access*, vol. 7, pp. 116 753–116 773, 2019.

[37] M. Di Renzo, A. Zappone, M. Debbah, M.-S. Alouini, C. Yuen, J. de Rosny, and S. Tretyakov, "Smart radio environments empowered by reconfigurable intelligent surfaces: How it works, state of research, and the road ahead," *IEEE J. Sel. Areas Commun.*, vol. 38, no. 11, pp. 2450–2525, Nov. 2020.

[38] UNB-lens-arrays (UNB-LA). THz Sensing Group, Delft University of Technology. Delft, The Netherlands. [Online]. Available: https://terahertz.tudelft.nl/Research/project.php?id=182&pid=697

[39] A. Neto and J. J. Lee, "'Infinite bandwidth' long slot array antenna," *IEEE Antennas Wireless Propag. Lett.*, vol. 4, p. 75–78, 2005.

[40] ——, "Ultrawide-band properties of long slot arrays," *IEEE Trans. Antennas Propag.*, vol. 54, no. 2, pp. 534–543, Feb. 2006.

[41] D. Cavallo, W. H. Syed, and A. Neto, "Connected-slot array with artificial dielectrics: A 6 to 15 GHz dual-pol wide-scan prototype," *IEEE Trans. Antennas Propag.*, vol. 66, no. 6, pp. 3201–3206, Jun. 2018.

[42] A. van Katwijk and D. Cavallo, "Analysis and design of connected slot arrays with artificial dielectrics," in *Proc. IEEE Int. Symp. Phased Array Syst. Technol.*, Waltham, MA, USA, Oct. 2019, pp. 1–5.

[43] A. J. van Katwijk, A. Neto, G. Toso, and D. Cavallo, "Design of wideband wide-scanning dual-polarized phased array covering simultaneously both the Ku- and the Ka-satcom bands," in *Proc. Eur. Conf. Antennas Propag.*, Copenhagen, Denmark, Mar. 15-20 2020.

[44] D. Cavallo, A. Neto, and G. Gerini, "Green's function based equivalent circuits for connected arrays in transmission and in reception," *IEEE Trans. Antennas Propag.*, vol. 59, no. 5, pp. 1535–1545, May 2011.

[45] W. H. Syed, D. Cavallo, H. Thippur Shivamurthy, and A. Neto, "Wideband, wide-scan planar array of connected slots loaded with artificial dielectric superstrates," *IEEE Trans. Antennas Propag.*, vol. 64, no. 2, pp. 543–553, Feb. 2016.

[46] D. Cavallo, W. H. Syed, and A. Neto, "Closed-form analysis of artificial dielectric layers—Part I: Properties of a single layer under plane-wave incidence," *IEEE Trans. Antennas Propag.*, vol. 62, no. 12, pp. 6256–6264, Dec. 2014.

[47] ——, "Closed-form analysis of artificial dielectric layers—Part II: Extension to multiple layers and arbitrary illumination," *IEEE Trans. Antennas Propag.*, vol. 62, no. 12, pp. 6265–6273, Dec. 2014.

[48] D. Cavallo and R. M. van Schelven, "Closed-form analysis of artificial dielectric layers with non-periodic characteristics," in *Proc. Eur. Conf. Antennas Propag.*, Warsaw, Poland, Mar. 31 - Apr. 5 2019, pp. 1–5.

[49] D. Cavallo and C. Felita, "Analytical formulas for artificial dielectrics with nonaligned layers," *IEEE Trans. Antennas Propag.*, vol. 65, no. 10, pp. 5303–5311, Oct. 2017.

[50] R. M. van Schelven and D. Cavallo, "Analysis of nonsquare artificial dielectric layers and application to the design of anisotropic slabs," *IEEE Antennas Wirel. Propag. Lett.*, vol. 21, no. 2, pp. 302–306, 2022.

[51] E. G. Larsson, O. Edfors, F. Tufvesson, and T. L. Marzetta, "Massive MIMO for next generation wireless systems," *IEEE Commun. Mag.*, vol. 52, no. 2, pp. 186–195, Feb. 2014.

[52] M. Akrout, V. Shyianov, F. Bellili, A. Mezghani, and R. W. Heath, "Super-wideband massive MIMO," *IEEE J. Sel. Areas Commun.*, vol. 41, no. 8, pp. 2414–2430, Aug. 2023.

[53] E. Björnson, C.-B. Chae, R. W. Heath, T. L. Marzetta, A. Mezghani, L. Sanguinetti, F. Rusek, M. R. Castellanos, D. Jun, and O. T. Demir, "Towards 6G MIMO: Massive spatial multiplexing, dense arrays, and interplay between electromagnetics and processing," *Proc. IEEE*, 2024, submitted for publication. [Online]. Available: https://arxiv.org/abs/2401.02844

[54] A. A. D'Amico and L. Sanguinetti, "Holographic MIMO communications: What is the benefit of closely spaced antennas?" *IEEE Trans. Wirel. Commun.*, 2024, submitted for publication. [Online]. Available: https://arxiv.org/abs/2307.13467v3

[55] C. Ehrenborg and M. Gustafsson, "Physical bounds and radiation modes for MIMO antennas," *IEEE Trans. Antennas Propag.*, vol. 68, no. 6, pp. 4302–4311, Jun. 2020.

[56] C. Ehrenborg, M. Gustafsson, and M. Capek, "Capacity bounds and degrees of freedom for MIMO antennas constrained by Q-factor," *IEEE Trans. Antennas Propag.*, vol. 69, no. 9, pp. 5388–5400, Sep. 2021.

[57] C. Ehrenborg and M. Gustafsson, "Fundamental bounds on MIMO antennas," *IEEE Antennas Wirel. Propag. Lett.*, vol. 17, no. 1, pp. 21–24, 2018.

[58] L. Passalacqua, C. Yepes, A. M. Barrera, B. Biscontini, E. Martini, and S. Maci, "Maximum gain of lossy antennas without and with Q-bounds," *IEEE Trans. Antennas Propag.*, vol. 72, no. 4, pp. 3033–3043, Apr. 2024.

[59] L. Passalacqua, C. Yepes, E. Martini, and S. Maci, "Q-bounded maximum directivity of self-resonant antennas," *IEEE Trans. Antennas Propag.*, vol. 71, no. 12, pp. 9549–9558, Dec. 2023.

[60] W. H. Syed, G. Fiorentino, D. Cavallo, M. Spirito, P. M. Sarro, and A. Neto, "Design, fabrication, and measurements of a 0.3 THz on-chip double slot antenna enhanced by artificial dielectrics," *IEEE Transactions on Terahertz Science and Technology*, vol. 5, no. 2, pp. 288–298, Mar. 2015.

[61] E. Darve, "The fast multipole method: Numerical implementation," *J. Comput. Phys.*, vol. 160, no. 1, pp. 195–240, 2000.

[62] J. C. Rautio and M. A. Thelen, "Method of moments analysis of arbitrary structures in shielded layered media," *IEEE Transactions on Microwave Theory and Techniques*, vol. 69, no. 1, pp. 509–517, Jan. 2021.

[63] N. van Rooijen, M. Alonso-delPino, M. Spirito, and N. Llombart, "Core-shell leaky-wave lens antenna for 150 GHz fly's eye communication systems," in *Proc. Eur. Conf. Antennas Propag.*, Madrid, Spain, Mar. 27 - Apr. 1 2022.

[64] N. van Rooijen, M. Alonso-delPino, J. Bueno, M. Spirito, and N. Llombart, "Electrically small high permittivity lens antenna using artificially loaded thermoplastics at 170 GHz," in *Proc. Int. Conf. Infrared Millim. Terahertz Waves*, Montreal, Canada, Sep. 17 - 22 2023.

[65] E. Lima, J. R. Costa, M. G. Silveirinha, and C. A. Fernandes, "ILASH — software tool for the design of integrated lens antennas," in *Proc. IEEE Antennas Propag. Soc. Int. Symp.*, San Diego, CA, USA, Jul. 5-11 2008.

[66] J. Budhu and Y. Rahmat-Samii, "A novel and systematic approach to inhomogeneous dielectric lens design based on curved ray geometrical optics and particle swarm optimization," *IEEE Trans. Antennas Propag.*, vol. 67, no. 6, pp. 3657–3669, Jun. 2019.

[67] A. Paraskevopoulos, F. Maggiorelli, M. Albani, and S. Maci, "Radial GRIN lenses based on the solution of a regularized ray congruence equation," *IEEE Trans. Antennas Propag.*, vol. 70, no. 2, pp. 888–899, Feb. 2022.

[68] Q. Liao, N. J. G. Fonseca, M. Camacho, Á. Palomares-Caballero, F. Mesa, and O. Quevedo-Teruel, "Ray-tracing model for generalized geodesic-lens multiple-beam antennas," *IEEE Trans. Antennas Propag.*, vol. 71, no. 3, pp. 2640–2651, Mar. 2023.

[69] P. Castillo-Tapia, J. Rico-Fernández, S. Clendinning, F. Mesa, and O. Quevedo-Teruel, "Evaluation of losses in 3-D-printed geodesic lenses using a ray-tracing model," *IEEE Trans. Antennas Propag.*, vol. 72, no. 1, pp. 234–242, Jan. 2024.

[70] M. Chen, O. Habiboglu, F. Mesa, and O. Quevedo-Teruel, "Ray-tracing and physical-optics model for planar mikaelian lens antennas," *IEEE Trans. Antennas Propag.*, vol. 72, no. 2, pp. 1735–1744, Feb. 2024.

[71] W. Hu, C. M. Coco Martin, and D. Cavallo, "Design formulas for flat gradient index lenses with planar or spherical output wavefront," *IEEE Trans. Antennas Propag.*, vol. 72, no. 3, pp. 2555–2563, Mar. 2024.

[72] I. Gashi, A. Paraskevopoulos, S. Maci, and M. Albani, "GO analysis of GRIN lens antennas by combining in a single ODE, field and wavefront-curvature transport to the ray tracing," *IEEE Trans. Antennas Propag.*, vol. 72, no. 3, pp. 2147–2160, Mar. 2024.

[73] M. Pubill-Font, F. Mesa, A. Algaba-Brazález, S. Clendinning, M. Johansson, and O. Quevedo-Teruel, "2D ray tracing model for multilayer dielectric dome arrays with inner reflections," *IEEE Open J. Antennas Propag.*, 2024, to be published.

[74] S. O. Dabironezare, A. Nair, A. Neto, and N. Llombart, "Estimation of mutual coupling in integrated lens arrays using a geometrical optics based technique with a bi-directional forward ray-tracing," *IEEE Trans. Antennas Propag.*, 2024, to be published.

[75] D. F. Filipovic, S. S. Gearhart, and G. M. Rebeiz, "Double-slot antennas on extended hemispherical and elliptical silicon dielectric lenses," *IEEE Trans. Microw. Theory Tech.*, vol. 41, no. 10, pp. 1738–1749, Oct. 1993.

[76] H. Zhang, S. O. Dabironezare, G. Carluccio, A. Neto, and N. Llombart, "A Fourier optics tool to derive the plane wave spectrum of quasi-optical systems [EM programmer's notebook]," *IEEE Antennas Propag. Mag.*, vol. 63, no. 1, pp. 103–116, Feb. 2021.

[77] G. Godi, R. Sauleau, and D. Thouroude, "Performance of reduced size substrate lens antennas for millimeter-wave communications," *IEEE Trans. Antennas Propag.*, vol. 53, no. 4, pp. 1278–1286, Apr. 2005.

[78] S. Bosma, "Scanning lens phased array antennas analysis, design," PhD thesis, Faculty of EEMCS, Delft Univ. of Technology, Delft, The Netherlands, Jan. 2023.

[79] J. C. R. Poirier, G. A. Morin, Y. M. M. Antar, and J. W. Moffat, "Millimetre-wave limited-scan array using small lenses," in *Proc. IEEE Antennas Propag. Soc. Int. Symp.*, vol. 2, Boston, MA, USA, Jul. 8-13 2001, pp. 823–826.

[80] J. G. Andrews, T. Bai, M. N. Kulkarni, A. Alkhateeb, A. K. Gupta, and R. W. Heath, "Modeling and analyzing millimeter wave cellular systems," *IEEE Trans. Commun.*, vol. 65, no. 1, pp. 403–430, Jan. 2017.

[81] T. Schneider, A. Wiatrek, S. Preussler, M. Grigat, and R.-P. Braun, "Link budget analysis for terahertz fixed wireless links," *IEEE Trans. Terahertz Sci. Technol.*, vol. 2, no. 2, pp. 250–256, Mar. 2012.

[82] K. S. Rao, G. A. Morin, M. Q. Tang, S. Richard, and K. K. C. Cham, "Development of a 45 GHz multiple-beam antenna for military satellite communications," *IEEE Trans. Antennas Propag.*, vol. 43, no. 10, pp. 1036–1047, Oct. 1995.

[83] S. K. Rao, "Design and analysis of multiple-beam reflector antennas," *IEEE Antennas Propag. Mag.*, vol. 41, no. 4, pp. 53–59, Aug. 1999.

[84] S. K. Rao, C.-C. Hsu, and K. K. Chan, "Antenna system supporting multiple frequency bands and multiple beams," *IEEE Trans. Antennas Propag.*, vol. 56, no. 10, pp. 3327–3329, Oct. 2008.

[85] N. Llombart, A. Neto, G. Gerini, M. Bonnedal, and P. De Maagt, "Leaky wave enhanced feed arrays for the improvement of the edge of coverage gain in multibeam reflector antennas," *IEEE Trans. Antennas Propag.*, vol. 56, no. 5, pp. 1280–1291, May 2008.

[86] T. N. Kaifas, D. G. Babas, G. Toso, and J. N. Sahalos, "Multibeam antennas for global satellite coverage: Theory and design," *IET Microw. Antennas Propag.*, vol. 10, no. 14, pp. 1475–1484, Nov. 2016.

[87] B. Biscontini, A. Murillo, J. Segador, and I. Gonzalez, "Active antenna architectures for enhanced 5G system performance," in *Proc. Eur. Conf. Antennas Propag.*, Mar. 15-20 2020.

[88] O. M. Bucci and G. Franceschetti, "On the degrees of freedom of scattered fields," *IEEE Trans. Antennas Propag.*, vol. 37, no. 7, pp. 918–926, Jul. 1989.

[89] P.-S. Kildal, E. Martini, and S. Maci, "Degrees of freedom and maximum directivity of antennas: A bound on maximum directivity of nonsuperreactive antennas," *IEEE Antennas Propag. Mag.*, vol. 59, no. 4, pp. 16–25, Aug. 2017.

[90] S. Stein, "On cross coupling in multiple-beam antennas," *IRE Trans. Antennas Propag.*, vol. 10, no. 5, pp. 548–557, Sep. 1962.

[91] A. Neto, N. Llombart, and A. Freni, "The observable field for antennas in reception," *IEEE Trans. Antennas Propag.*, vol. 66, no. 4, pp. 1736–1746, Apr. 2018.

[92] A. Neto, A. Fiorellini Bernardis, D. Emer, A. Freni, and N. Llombart, "The observable field in complex scattering scenarios," *IEEE Trans. Antennas Propag.*, vol. 68, no. 7, pp. 5544–5555, Jul. 2020.

[93] R. Harrington, "On the gain and beamwidth of directional antennas," *IEEE Trans. Antennas Propag*, vol. 6, no. 3, pp. 219–225, Jul. 1958.

[94] D.-H. Kwon and D. M. Pozar, "Optimal characteristics of an arbitrary receive antenna," *IEEE Trans. Antennas Propag.*, vol. 57, no. 12, pp. 3720–3727, Dec. 2009.

[95] V. Rumsey, "On the design and performance of feeds for correcting spherical aberration," *IEEE Trans. Antennas Propag.*, vol. 18, no. 3, pp. 343–351, May 1970.

[96] ——, "Reaction concept in electromagnetic theory," *Phys. Rev.*, vol. 94, no. 6, pp. 1483–1491, Jun. 1954.

[97] J. van Bladel, *Electromagnetic Fields*. Hoboken, NJ, USA: Wiley, 2007.

[98] A. T. De Hoop, "The N-port receiving antenna and its equivalent electrical network," *Philips Res. Rep.*, vol. 30, pp. 302–315, 1975.

[99] P. F. Goldsmith, "Radiation patterns of circular apertures with gaussian illumination," *Int. J. Infr. Millim. Waves*, vol. 8, no. 7, pp. 718–771, Jul. 1987.

[100] W. Xiang, K. Zheng, and X. Shen, *5G Mobile Communications*. Cham: Springer International Publishing, 2017.

[101] J. Allen, "A theoretical limitation on the formation of lossless multiple beams in linear arrays," *IRE Trans. Antennas Propag.*, vol. 9, no. 4, pp. 350–352, Jul. 1961.

[102] W. White, "Pattern limitations in multiple-beam antennas," *IRE Trans. Antennas Propag.*, vol. 10, no. 4, pp. 430–436, Jul. 1962.

[103] R. G. Vaughan and J. B. Andersen, "Antenna diversity in mobile communications," *IEEE Trans. Veh. Technol.*, vol. 36, no. 4, pp. 149–172, Nov. 1987.

[104] S. Blanch, J. Romeu, and I. Corbella, "Exact representation of antenna system diversity performance from input parameter description," *Electron. Lett.*, vol. 39, pp. 705–707, May 2003.

[105] S. M. Mikki and Y. M. M. Antar, "On cross correlation in antenna arrays with applications to spatial diversity and MIMO systems," *IEEE Trans. Antennas Propag.*, vol. 63, no. 4, pp. 1798–1810, Apr. 2015.

[106] D. Sarkar, S. M. Mikki, and Y. M. M. Antar, "An efficient analytical evaluation of the electromagnetic cross correlation Green's function in MIMO systems," *IEEE Trans. Antennas Propag.*, vol. 67, no. 11, pp. 6947–6956, Nov. 2019.

[107] P. N. Fletcher, M. Dean, and A. R. Nix, "Mutual coupling in multi-element array antennas and its influence on MIMO channel capacity," *Electron. Lett.*, vol. 39, pp. 342–344, Feb. 2003.

[108] X. Li and Z.-P. Nie, "Mutual coupling effects on the performance of MIMO wireless channels," *IEEE Antennas Wirel. Propag. Lett.*, vol. 3, pp. 344–347, 2004.

[109] B. Wang, Y. Chang, and Y. Sun, "Performance of the large-scale adaptive array antennas in the presence of mutual coupling," *IEEE Trans. Antennas Propag.*, vol. 64, no. 6, pp. 2236–2245, Jun. 2016.

[110] X. Chen, S. Zhang, and Q. Li, "A review of mutual coupling in MIMO systems," *IEEE Access*, vol. 6, pp. 24 706–24 719, Apr. 2018.

[111] Z. Li, Z. Du, M. Takahashi, K. Saito, and K. Ito, "Reducing mutual coupling of MIMO antennas with parasitic elements for mobile terminals," *IEEE Trans. Antennas Propag.*, vol. 60, no. 2, pp. 473–481, Feb. 2012.

[112] I. Nadeem and D.-Y. Choi, "Study on mutual coupling reduction technique for MIMO antennas," *IEEE Access*, vol. 7, pp. 563–586, 2019.

[113] H. Steyskal and J. S. Herd, "Mutual coupling compensation in small array antennas," *IEEE Trans. Antennas Propag.*, vol. 38, no. 12, pp. 1971–1975, Dec. 1990.

[114] S. Bellofiore, C. A. Balanis, J. Foutz, and A. S. Spanias, "Smart-antenna systems for mobile communication networks. part 1. overview and antenna design," *IEEE Antennas Propag. Mag.*, vol. 44, no. 3, pp. 145–154, Jun. 2002.

[115] F. De Flaviis, L. Jofre, J. Romeu, and A. Grau, *Multiantenna Systems for MIMO Communications.* Cham, Switzerland: Springer, 2008.

[116] A. Ludwig, "Mutual coupling, gain and directivity of an array of two identical antennas," *IEEE Trans. Antennas Propag.*, vol. 24, no. 6, pp. 837–841, Nov. 1976.

[117] I. Tzanidis, G. Z. Hutcheson, Y. Li, J. Oh, W. Hong, G. Xu, and J. Zhang, "Method and apparatus for miniaturization of MIMO systems via tightly coupled antenna array," U.S. Patent 0 334 565 A1, Nov. 13, 2014.

[118] W. Kahn, "Impedance-match and element-pattern constraints for finite arrays," *IEEE Trans. Antennas Propag.*, vol. 25, no. 6, pp. 747–755, Nov. 1977.

[119] C. Yepes, E. Gandini, S. Monni, A. Neto, F. E. van Vliet, and D. Cavallo, "Analysis of tilted dipole arrays: Impedance and radiation properties," *IEEE Trans. Antennas Propag.*, vol. 68, no. 1, pp. 254–265, Jan. 2020.

[120] D. Cavallo, W. H. Syed, and A. Neto, "Equivalent transmission line models for the analysis of edge effects in finite connected and tightly coupled arrays," *IEEE Trans. Antennas Propag.*, vol. 65, no. 4, pp. 1788–1796, Apr. 2017.

[121] E. Bjornson, L. Van der Perre, S. Buzzi, and E. G. Larsson, "Massive MIMO in sub-6 GHz and mmwave: Physical, practical, and use-case differences," *IEEE Wirel. Commun.*, vol. 26, no. 2, pp. 100–108, Jan. 2019.

[122] *Radio-Frequency Channel Arrangements for Medium- and High-Capacity Digital Fixed Wireless Systems Operating in the 6425–7125 MHz Band*, Int. Telecommun. Union, Geneva, Switzerland, 2012. [Online]. Available: https://www.itu.int/rec/R-REC-F.384-11-201203-I

[123] Y. Wang, L. Zhu, H. Wang, Y. Luo, and G. Yang, "A compact, scanning tightly coupled dipole array with parasitic strips for next-generation wireless applications," *IEEE Antennas Wireless Propag. Lett*, vol. 17, no. 4, pp. 534–537, Apr. 2018.

[124] D.-M. Sun, Z.-C. Hao, W.-Y. Liu, and C.-Y. Ding, "An ultrawideband dual-polarized phased array antenna for sub-3–GHz 5G applications with a high polarization isolation," *IEEE Trans. Antennas Propag.*, vol. 71, no. 5, pp. 4055–4065, May. 2023.

[125] M. H. Novak, F. A. Miranda, and J. L. Volakis, "Ultra-wideband phased array for millimeter-wave ISM and 5G bands, realized in PCB," *IEEE Trans. Antennas Propag.*, vol. 66, no. 12, pp. 6930–6938, Dec. 2018.

[126] S. M. Moghaddam, J. Yang, and A. U. Zaman, "Fully-planar ultrawideband tightly-coupled array (FPU-TCA) with integrated feed for wide-scanning millimeter-wave applications," *IEEE Trans. Antennas Propag.*, vol. 68, no. 9, pp. 6591–6601, Sep. 2020.

[127] T.-L. Zhang, L. Chen, S. M. Moghaddam, A. U. Zaman, and J. Yang, "Millimeter-wave ultrawideband circularly polarized planar array antenna using bold-C spiral elements with concept of tightly coupled array," *IEEE Trans. Antennas Propag.*, vol. 69, no. 4, pp. 2013–2022, Apr. 2021.

[128] D. H. Schaubert, S. Kasturi, A. O. Boryssenko, and W. M. Elsallal, "Vivaldi antenna arrays for wide bandwidth and electronic scanning," in *Proc. Eur. Conf. Antennas Propag.*, Edinburgh, U.K., Nov. 11-16 2007, pp. 1–6.

[129] J. J. Lee, S. Livingston, and R. Koenig, "A low-profile wide-band (5:1) dual-pol array," *IEEE Antennas Wireless Propag. Lett*, vol. 2, pp. 46–49, 2003.

[130] W. Elsallal, J. B. West, J. Wolf, R. Freeman, R. Legge, V. Olen, T. W. Darymple, M. B. Longbrake, and P. E. Buxa, "Charateristics of decade-bandwidth, balanced antipodal vivaldi antenna (BAVA) phased arrays with time-delay beamformer systems," in *Proc. IEEE Int. Symp. Phased Array Syst. Technol.*, Waltham, MA, USA, Oct. 2013, pp. 111–116.

[131] H. Holter, "Dual-polarized broadband array antenna with BOR-elements, mechanical design and measurements," *IEEE Trans. Antennas Propag.*, vol. 55, no. 2, pp. 305–312, Feb. 2007.

[132] R. W. Kindt and W. R. Pickles, "Ultrawideband all-metal flared-notch array radiator," *IEEE Trans. Antennas Propag.*, vol. 58, no. 11, pp. 3568–3575, Nov. 2010.

[133] J. J. Lee, S. Livingston, R. Koenig, D. Nagata, and L. L. Lai, "Compact light weight UHF arrays using long slot apertures," *IEEE Trans. Antennas Propag.*, vol. 54, no. 7, pp. 2009–2015, Jul. 2006.

[134] J. J. Lee, S. Livingston, and D. Nagata, "A low profile 10:1 (200–2000 MHz) wide band long slot array," in *Proc. IEEE Antennas Propag. Soc. Int. Symp.*, San Diego, CA, USA, Jul. 5-11 2008.

[135] J. P. Doane, K. Sertel, and J. L. Volakis, "A wideband, wide scanning tightly coupled dipole array with integrated balun (TCDA-IB)," *IEEE Trans. Antennas Propag.*, vol. 61, no. 9, pp. 4538–4548, Sep. 2013.

[136] W. F. Moulder, K. Sertel, and J. L. Volakis, "Ultrawideband superstrate-enhanced substrate-loaded array with integrated feed," *IEEE Trans. Antennas Propag.*, vol. 61, no. 11, pp. 5802–5807, Nov. 2013.

[137] M. H. Novak and J. L. Volakis, "Ultrawideband antennas for multiband satellite communications at UHF–Ku frequencies," *IEEE Trans. Antennas Propag.*, vol. 63, no. 4, pp. 1334–1341, Apr. 2015.

[138] R. J. Bolt, D. Cavallo, G. Gerini, D. Deurloo, R. Grooters, A. Neto, and G. Toso, "Characterization of a dual-polarized connected-dipole array for Ku-band mobile terminals," *IEEE Trans. Antennas Propag.*, vol. 64, no. 2, pp. 591–598, Feb. 2016.

[139] D. Cavallo, A. Neto, G. Gerini, A. Micco, and V. Galdi, "A 3- to 5-GHz wideband array of connected dipoles with low cross polarization and wide-scan capability," *IEEE Trans. Antennas Propag.*, vol. 61, no. 3, pp. 1148–1154, Mar. 2013.

[140] S. S. Holland, D. H. Schaubert, and M. N. Vouvakis, "A 7–21 GHz dual-polarized planar ultrawideband modular antenna (PUMA) array," *IEEE Trans. Antennas Propag.*, vol. 60, no. 10, pp. 4589–4600, Oct. 2012.

[141] J. A. Kasemodel, C.-C. Chen, and J. L. Volakis, "Wideband planar array with integrated feed and matching network for wide-angle scanning," *IEEE Trans. Antennas Propag.*, vol. 61, no. 9, pp. 4528–4537, Sep. 2013.

[142] E. Magill and H. Wheeler, "Wide-angle impedance matching of a planar array antenna by a dielectric sheet," *IEEE Trans. Antennas Propag.*, vol. 14, no. 1, pp. 49–53, Jan. 1966.

[143] Z. Chen, "Wideband feeding network design for dual-polarized connected arrays," Master's thesis, Faculty of EEMCS, Delft Univ. Technol., Delft, The Netherlands, 2021.

[144] J. Fuhl, J.-P. Rossi, and E. Bonek, "High-resolution 3-D direction-of-arrival determination for urban mobile radio," *IEEE Trans. Antennas Propag.*, vol. 45, no. 4, pp. 672–682, Apr. 1997.

[145] J. M. Edwards, R. O'Brient, A. T. Lee, and G. M. Rebeiz, "Dual-polarized sinuous antennas on extended hemispherical silicon lenses," *IEEE Trans. Antennas Propag.*, vol. 60, no. 9, pp. 4082–4091, Sep. 2012.

[146] A. J. Alazemi, H.-H. Yang, and G. M. Rebeiz, "Double bow-tie slot antennas for wideband millimeter-wave and terahertz applications," *IEEE Trans. Terahertz Sci. Technol.*, vol. 6, no. 5, pp. 682–689, Sep. 2016.

[147] K. Konstantinidis, A. P. Feresidis, C. C. Constantinou, E. Hoare, M. Gashinova, M. J. Lancaster, and P. Gardner, "Low-THz dielectric lens antenna with integrated waveguide feed," *IEEE Trans. Terahertz Sci. Technol.*, vol. 7, no. 5, pp. 572–581, Sep. 2017.

[148] M. Arias Campo, D. Blanco, S. Bruni, A. Neto, and N. Llombart, "On the use of fly's eye lenses with leaky-wave feeds for wideband communications," *IEEE Trans. Antennas Propag.*, vol. 68, no. 4, p. 2480–2493, Apr. 2020.

[149] M. Arias Campo, K. Holc, C. De Martino, M. Spirito, A. Leuther, S. Bruni, and N. Llombart, "H-band quartz-silicon leaky-wave lens with air-bridge interconnect to GaAs front-end," *IEEE Trans. Terahertz Sci. Technol.*, vol. 11, no. 3, pp. 297–309, May 2021.

[150] M. Hoogelander, S. L. van Berkel, E. S. Malotaux, M. Alonso-delPino, D. Cavallo, M. Spirito, and N. Llombart, "Chessboard focal plane array for a CMOS-integrated terahertz camera," *IEEE Trans. Terahertz Sci. Technol.*, vol. 13, no. 6, pp. 704–717, Nov. 2023.

[151] A. Neto, S. Maci, and P. J. I. de Maagt, "Reflections inside an elliptical dielectric lens antenna," *IEE Proc. Microw. Antennas Propag.*, vol. 145, no. 3, p. 243 – 247, Jun. 1998.

[152] R. Garg, I. Bahl, and M. Bozzi, *Microstrip Lines and Slotlines*, 3rd ed. Norwood, MA, USA: Artech House, 2007.

[153] *Sonnet*, Sonnet Soft., Syracuse, NY, USA, 2023.

[154] *CST Studio Suite*, Dassault Systèmes, Vélizy-Villacoublay, France, 2023.

[155] *Ansys Electronics*, Ansys, Canonsburg, PA, USA, 2023.

[156] *Advanced Design System*, Keysight, Santa Rosa, CA, USA, 2023.

[157] C. di Nallo, F. Mesa, and D. R. Jackson, "Excitation of leaky modes on multilayer stripline structures," *IEEE Trans. Microw. Theory Techn.*, vol. 46, no. 8, pp. 1062–1071, Aug. 1998.

[158] P. P. Burghignoli, C. Di Nallo, F. Frezza, A. Galli, and P. Lampariello, "Efficient description of impedance and radiation features in printedcircuit leaky-wave structures—an unconventional scattering-matrix approach," *IEEE Trans. Microw. Theory Techn.*, vol. 48, no. 10, p. 1661–1672, Oct. 2000.

[159] A. Neto and S. Maci, "Green's function for an infinite slot printed between two homogeneous dielectrics. I. Magnetic currents," *IEEE Trans. Antennas Propag.*, vol. 51, no. 7, p. 1572–1581, Jul. 2003.

[160] J. Bernal, F. Mesa, and D. R. Jackson, "Effects of losses on the current spectrum of a printed-circuit line," *IEEE Trans. Microw. Theory Techn.*, vol. 55, no. 7, p. 1511–1519, Jul. 2007.

[161] J. Bernal, F. Mesa, D. R. Jackson, W. L. Langston, and J. T. Williams, "High-frequency pulse distortion on a lossy microstrip line with a top cover," *IEEE Trans. Microw. Theory Techn.*, vol. 58, no. 7, p. 1774–1785, Jul. 2010.

[162] S. Paulotto, G. Lovat, P. Baccarelli, and P. Burghignoli, "Green's function calculation for a line source exciting a 2-D periodic printed structure," *IEEE Microw. Wireless Compon. Lett.*, vol. 20, no. 4, p. 181–183, Apr. 2010.

[163] S. Bruni and A. Neto, "The ultrawideband leaky lens antenna," *IEEE Trans. Antennas Propag.*, vol. 55, no. 10, p. 2642–2653, Oct. 2007.

[164] R. M. van Schelven, D. Cavallo, and A. Neto, "Equivalent circuit models of finite slot antennas," *IEEE Trans. Antennas Propag.*, vol. 67, no. 7, p. 4367–4376, Jul. 2019.

[165] S. L. van Berkel. Transmission line calculator. THz Sensing Group. Delft, The Netherlands. [Online]. Available: https://terahertz.tudelft.nl/Research/project.php?id=74&ti=27

[166] S. L. van Berkel, A. Garufo, N. Llombart, and A. Neto, "A quasi-analytical tool for the characterization of transmission lines at high frequencies [EM programmer's notebook]," *IEEE Antennas Propag. Mag.*, vol. 58, no. 3, pp. 82–90, Jun. 2016.

[167] D. Cavallo, "Connected array antennas: Analysis and design," PhD thesis, Dept. Elect. Eng., Eindhoven,The Netherlands, 2011.

[168] K. A. Michalski and D. Zheng, "Electromagnetic scattering and radiation by surfaces of arbitrary shape in layered media. I. Theory," *IEEE Trans. Antennas Propag.*, vol. 38, no. 3, p. 335–344, Mar. 1990.

[169] S. Ramo, J. R. Whinnery, and T. van Duzer, *Fields and Waves in Communication Electronics.* Hoboken, NJ, USA: Wiley, 1994.

[170] D. S. Jones, *Methods in Electromagnetic Wave Propagation.* Piscataway, NJ, USA: IEEE Press, 1995.

[171] D. Cavallo, W. H. Syed, and A. Neto, "Equivalent transmission line models for the analysis of edge effects in finite connected and tightly coupled arrays," *IEEE Trans. Antennas Propag.*, vol. 65, no. 4, pp. 1788–1796, Apr. 2017.

[172] N. K. Das, "A new theory of the characteristic impedance of general printed transmission lines applicable when power leakage exists," *IEEE Trans. Microw. Theory Techn.*, vol. 48, no. 7, p. 1108–1117, Jul. 2000.

[173] F. Mesa and D. R. Jackson, "A novel approach for calculating the characteristic impedance of printed-circuit lines," *IEEE Microw. Wireless Compon. Lett.*, vol. 15, no. 4, p. 283–285, Apr. 2005.

[174] J. C. Rautio and V. Demir, "Microstrip conductor loss models for electromagnetic analysis," *IEEE Trans. Microw. Theory Techn.*, vol. 51, no. 3, p. 915–921, Mar. 2003.

[175] E. M. Hamham, F. Mesa, F. Medina, and M. Khalladi, "Surface impedance quasi-transverse electromagnetic approach for the efficient calculation of conductor losses in multilayer single and coupled microstrip lines," *IET Microw., Antennas Propag.*, vol. 6, no. 5, p. 519–526, 2012.

[176] J. Aguilera, R. Marques, and M. Horno, "Quasi-TEM surface impedance approaches for the analysis of mic and mmic transmission lines, including both conductor and substrate losses," *IEEE Trans. Microw. Theory Techn.*, vol. 43, no. 7, p. 1553–1558, Jul. 1995.

[177] A. Neto and S. Maci, "Input impedance of slots printed between two dielectric media and fed by a small Δ-gap," *IEEE Antennas Wireless Propag. Lett.*, vol. 3, p. 113–116, 2004.

[178] R. Rodriguez-Berral, F. Mesa, and D. R. Jackson, "A high-frequency circuit model for the gap excitation of a microstrip line," *IEEE Trans. Microw. Theory Techn.*, vol. 54, no. 12, p. 4100–4110, Dec. 2006.

[179] R. F. Harrington, *Field Computation by Moment Methods.* Hoboken, NJ, USA: Wiley, 1993.

[180] G. Burke and A. Poggio, "Numerical electromagnetics code (NEC)-method of moments; Part I: Program description-theory," Nav. Ocean Syst. Centre, San Diego, CA, USA, Tech. Rep. TD 116, Jan. 1981.

[181] L. Knockaert, "Comparing three different formulas for the internal impedance of a circular wire," *Microw. Opt. Technol. Lett.*, vol. 43, no. 1, p. 1–3, 2004.

[182] D. B. Davidson, "Convergence of the MPIE Galerkin MoM thin wire formulation," *IEEE Trans. Antennas Propag.*, vol. 69, no. 10, pp. 7073–7078, Oct. 2021.

[183] D. B. Davidson and K. F. Warnick, "MoM modeling of thin wires with finite conductivity for radio astronomy applications," in *Proc. 2023 IEEE Antennas Propag. Soc. Int. Symp.*, Portland, OR, USA, Jul. 2023, pp. 769–770.

[184] W. R. Dommisse, J. T. Du Plessis, P. I. Cilliers, M. M. Botha, and T. Rylander, "Macro basis functions for efficient analysis of thick wires in the MoM," *IEEE Trans. Antennas Propag.*, vol. 72, no. 7, pp. 5865–5876, Jul. 2024.

[185] N. Uzunoglu, N. Alexopoulos, and J. Fikioris, "Radiation properties of microstrip dipoles," *IEEE Trans. Antennas Propag.*, vol. 27, no. 6, pp. 853–858, Nov. 1979.

[186] I. Rana and N. Alexopoulos, "Current distribution and input impedance of printed dipoles," *IEEE Trans. Antennas Propag.*, vol. 29, no. 1, pp. 99–105, Jan. 1981.

[187] N. Alexopoulos and D. Jackson, "Fundamental superstrate (cover) effects on printed circuit antennas," *IEEE Trans. Antennas Propag.*, vol. 32, no. 8, pp. 807–816, Aug. 1984.

[188] D. Cavallo, A. Neto, and G. Gerini, "Analytical description and design of printed dipole arrays for wideband wide-scan applications," *IEEE Trans. Antennas Propag.*, vol. 60, no. 12, pp. 6027–6031, Dec. 2012.

[189] F. Mesa, C. di Nallo, and D. R. Jackson, "The theory of surface-wave and space-wave leaky-mode excitation on microstrip lines," *IEEE Trans. Microw. Theory Techn.*, vol. 47, no. 2, pp. 207–215, Feb. 1999.

[190] J. R. Mosig, "Scattering by arbitrarily-shaped slots in thick conducting screens: an approximate solution," *IEEE Trans. Antennas Propag.*, vol. 52, no. 8, pp. 2109–2117, Aug. 2004.

[191] A. Mazzinghi, A. Freni, and M. Albani, "Influence of the finite slot thickness on RLSA antenna design," *IEEE Trans. Antennas Propag.*, vol. 58, no. 1, pp. 215–218, Jan. 2010.

[192] S. Monni, G. Gerini, A. Neto, and A. G. Tijhuis, "Multimode equivalent networks for the design and analysis of frequency selective surfaces," *IEEE Trans. Antennas Propag.*, vol. 55, no. 10, pp. 2824–2835, Oct. 2007.

[193] F. Costa, A. Monorchio, and G. Manara, "Efficient analysis of frequency-selective surfaces by a simple equivalent-circuit model," *IEEE Antennas Propag. Mag.*, vol. 54, no. 4, pp. 35–48, Aug. 2012.

[194] F. Mesa, M. García-Vigueras, F. Medina, R. Rodríguez-Berral, and J. R. Mosig, "Circuit-model analysis of frequency selective surfaces with scatterers of arbitrary geometry," *IEEE Antennas Wirel. Propag. Lett.*, vol. 14, pp. 135–138, 2015.

[195] A. J. van Katwijk, A. Neto, G. Toso, and D. Cavallo, "Efficient semi-analytical method for the analysis of large finite connected slot arrays," *IEEE Trans. Antennas Propag.*, vol. 71, no. 1, pp. 402–410, Jan. 2015.

[196] D. Rutledge and M. Muha, "Imaging antenna arrays," *IEEE Trans. Antennas Propag.*, vol. 30, no. 4, pp. 535–540, Jul. 1982.

[197] M. Gustafsson and M. Capek, "Maximum gain, effective area, and directivity," *IEEE Trans. Antennas Propag.*, vol. 67, no. 8, pp. 5282–5293, Aug. 2019.

[198] D. Cavallo, "Parallel-plate waveguide-feeding structure for planar-connected arrays," *IEEE Antennas Wirel. Propag. Lett.*, vol. 21, no. 4, pp. 765–768, 2022.

[199] H. Zhang, S. O. Dabironezare, J. J. A. Baselmans, and N. Llombart, "Focal plane array of shaped quartz lenses for wide field-of-view submillimeter imaging systems," *IEEE Trans. Antennas Propag.*, vol. 72, no. 2, pp. 1263–1274, Feb. 2024.

[200] M. Abramowitz and I. A. Stegun, *Handbook of Mathematical Functions with Formulas, Graphs, and Mathematical Tables.* New York, NY, USA: Dover, 1964.

[201] J. Markkanen, P. Yla-Oijala, and A. Sihvola, "Discretization of volume integral equation formulations for extremely anisotropic materials," *IEEE Trans. Antennas Propag.*, vol. 60, no. 11, pp. 5195–5202, Nov. 2012.

[202] A. G. Polimeridis, J. F. Villena, L. Daniel, and J. K. White, "Stable FFT-JVIE solvers for fast analysis of highly inhomogeneous dielectric objects," *J. Comput. Phys.*, vol. 269, pp. 280–296, 2014.

[203] M. C. van Beurden and S. J. L. van Eijndhoven, "Well-posedness of domain integral equations for a dielectric object in homogeneous background," *J. Eng. Math.*, vol. 62, pp. 289–302, 2008.

[204] C. A. Balanis, *Anthenna Theory: Analysis and Design.* Hoboken, NJ, USA: Wiley, 2016.

[205] A. A. Tambova, M. S. Litsarev, G. Guryev, and A. G. Polimeridis, "On the generalization of DIRECTFN for singular integrals over quadrilateral patches," *IEEE Trans. Antennas Propag.*, vol. 66, no. 1, pp. 304–314, Jan. 2018.

[206] M. F. Catedra, E. Gago, and L. Nuno, "A numerical scheme to obtain the RCS of three-dimensional bodies of resonant size using the conjugate gradient method and the fast Fourier transform," *IEEE Trans. Antennas Propag.*, vol. 37, no. 5, pp. 528–537, May 1989.

[207] J. R. Shewchuk, "An introduction to the conjugate gradient method without the agonizing pain," 1994. [Online]. Available: https://www.cs.cmu.edu/~quake-papers/painless-conjugate-gradient.pdf

[208] Y. Saad, "Iterative methods for sparse linear systems," 2003. [Online]. Available: https://www-users.cse.umn.edu/~saad/IterMethBook_2ndEd.pdf

Propositions Accompanying the Doctoral Thesis

I. The massive MIMO performance of an antenna design or even a manufactured prototype can be assessed with the aid of the observable field, which also allows a comparison with the maximum gain antenna located within the same space. *This proposition pertains to Chapter 2 of this dissertation.*

II. In a phased array system, it is possible to radiate orthogonal beams regardless of the mutual coupling levels between the feeding ports. The only constraints regard the beam overlap and the side lobes. *This proposition pertains to Chapter 3 of this dissertation.*

III. When analyzing integrated antennas, it is possible to split the reflections caused by the material discontinuities from an outwardly propagating wave emerging from the feed. *This proposition pertains to Chapter 5 of this dissertation.*

IV. The input impedance of a dipole is given by the superposition of three different phenomena: the capacitance of the feed, the propagation on the dipole's arms, and the endpoint contribution. *This proposition pertains to Chapters 6 and 7 of this dissertation.*

V. Thanks to rationality and scientific knowledge, we have created an unprecedented wave of progress that has meliorated our quality of life. As we all live longer, healthier, and with easy access to food, some of us can dedicate their time to intellectual efforts, and this constitutes a self-sustaining process.

VI. Communicating science to the general public is somewhat the opposite of what the scientific method is.

VII. According to Kahneman and Tversky's studies, two modes of reasoning co-exist: System 1, which is instinctive and fast, and System 2, which is rational but slow. Ordinary daily lives often rely on the autopilot mode of System 1. Scientific researchers have to rewire their brains to let System 2 act most of the time.

VIII. Our society constantly exposes us to news, mostly which diverts our attention and triggers our instincts. Under these circumstances, it is difficult to distinguish the truth from the false, delve deeply into the matter, and form an opinion that is factual, independent, and rational.

IX. You should not compare yourself to others. Everyone's starting point is different, and we are all immersed in different circumstances. Therefore, the highest recognition is only the one you obtain from yourself.

X. Irony and self-mockery allow to see critically the outer world and yourself, and these both are essential tools to bear existence. Unfortunately, they are not at everyone's disposal.

These propositions are regarded as opposable and defendable, and have been approved as such by the promotors prof. dr. ing. A. Neto and dr. D. Cavallo.

Acknowledgements

We live in this world in order always to learn industriously and to enlighten each other by means of discussion and to strive vigorously to promote the progress of science and the fine arts.

–W. A. Mozart

First of all, I want to thank my promotor, prof. dr. ing. Andrea Neto, for his invaluable, constant, and energetic help during my PhD. You have given me an immense opportunity to offer me, as a true outsider, this position. I have always been fascinated by your sharp intuitions and by how you can grasp physical interpretations from the most complex formulas. Your ambitions, contagious enthusiasm, and curiosity have been exceptional stimuli that have encouraged me to keep on working. My early career could not benefit more from our interactions. Working in such close collaboration with you and being kept in such high consideration have been true privileges.

My gratitude also goes to my co-promotor, dr. Daniele Cavallo. Thank you, Daniele, for having personally taught me about connected arrays when I was a master student, and for having patiently helped me to put things into practice. Besides this, you have shown me how to troubleshoot my work when needed and to present it nicely. I hope I have learned a bit of this.

I also want to thank prof. Angelo Freni, for having started teaching me electromagnetics many years ago and for having given me the opportunity to have my master's thesis in the Netherlands, which set off the beginning of this work. During our interactions, you showed me how your work can benefit from a rigorous and skeptical attitude. Also, thank you for hosting me in Florence in 2021 when I started working on numerical methods. I also want to thank your inseparable colleague, prof. Luca Facheris, with whom I am still whimsically in touch. I will soon bring to both of you some *tortelli*, when I visit the department there.

I would like to thank prof. dr. Nuria Llombart, an invaluable member of the THz Sensing Group, for all of her comments and questions during and after the group

presentations these years. These have helped me enormously to look at my work critically and strengthen my statements.

Thank you, dr. *Hansi* Lager, for the productive collaboration in "Electricity and Magnetism", my help in the course has been extremely formative to me. I also want to thank dr. Paolo *Paul* Sberna, for all the serious and less serious interactions we have had in the past year. I want to thank dr. Maria Alonso-delPino, for all our good moments spent at the conferences all around the world over these years.

I would like to thank Ulrik Imberg, our industrial partner from Huawei Sweden, for having financed the project, for his esteem towards us, and for all the interesting interactions that gave me an idea about the industrial mindset.

A thought also goes to all the other colleagues from the THz Sensing Group, for their help when needed, but also for the time together. My office mate Martijn, not only for having been an excellent person to spend working hours with but also for having some good memories together. Thank you, and Mechteld, for the providential car ride from Schiphol and for inviting me to your great wedding party, even if I was liquefying due to the temperature and my suit and tie. Thank you, Alejandro ~~Pascual~~ Laguna, for having been such a good friend; I hope you are doing great in Madrid. Thank you, Nina, for all of the laughs and jokes during the long workdays.

I am profoundly in debt to Zhuang, Jinglin, Roderick, Erik, and Cesare, whom I have supervised during these years and who have helped me obtain many good results in this dissertation. I want to thank my paranymphs Jinglin and Roderick, for lifting the spirits when many things were not okay. Moreover, thank you, Roderick, for translating the summary into fine Dutch, and thank you, Martijn Huiskes and Caspar, for revising it.

I want to thank all the friends I have shared memories with during these years.

All the friends from padel, especially Giovanni, for the innumerable matches you have organized.

My golf friends Edgar, Willem, Max, Chris, and Gabriel for the rounds at Delfland in the good summer weather and during the windy winter days.
Thank you, Gabriel, for being such a supportive friend. Your concept of friendship is really admirable.

All the friends from the Silent Book Club, thank you for our discussions and chats.

A great thank you also goes to my friends from my university years. Thank you, Nicolò G., for keeping in touch in these years. I hope more adventures and good memories will follow in the coming years. Thank you, Niccolò B.; you were a true friend when we moved to Delft.

Thank you, Andrea A., for being a great role model when I started my studies in engineering and decided to follow a path similar to yours. We finally managed to reconnect after a long time last year in California.

Thank you, Alessandro, for having been such an example of dedication, leadership, confidence, and problem-solving. Thanks to you, I have understood that there are other things in life besides my studies. Attending your wedding remotely was definitely a very unique experience.

I want to thank my friends at home, finally. Thank you, Francesco, for reconnecting with me after so many years. It was great that we had things in common, such as playing golf and having a passion for that disgusting show every day on air on Confindustria's radio. Thank you, Letizia, for the endless phone calls, all the gossip, and your sharp humor. Thank you, Marco *Astrakan* for your unshakeable friendship, humor, and inside jokes even if I was far away.

I also want to thank all the people whose written or spoken words have accompanied me over these years and have sharpened my critical mind: Dr. Dario Bressanini, Luca Romano, aka Avvocato dell'Atomo, Prof. Guido Silvestri, Dr. Beatrice Mautino and Emanuele Menietti, Prof. Hans Rosling, Prof. Alberto Grandi, and Prof. Michele Boldrin.

A special and completely undeserved thank also goes to Giuseppe Cruciani and Davìd *il Tigre* Parenzo, who have delighted me nearly every day, despite their exceptionally long holidays, with their *disgraziata trasmissione* on air on Confindustria's radio. I am still questioning whether earning a PhD in a world-renowned institution is compatible with being a listener of yours.

I want to thank all of my cousins, who are, for different reasons, older brothers or sisters, and we are all mourning the loss of one of us. A great thank you goes to Giovanni for all the calls and for hosting me at your place in Tenerife. Thank you, *my almost cousin* Lorenzo; I really cherish thinking about the daily video calls we had during the lockdown. You, Giovanni, and I have created a trio that keeps me company daily.

My research has also benefited from the help of my aunt Giuseppina and uncle Giovanni Vittorio, who patiently hosted me in Florence when I was learning the method of moments. I also treasure all our early morning rounds every summer in Poppi, zio.

A great thought goes to my dear parents, Luciana and Giulio, who have lovingly supported me. Since a young age, you have encouraged me towards the path of study, learning, and knowledge. Thanks to your guidance and support, I was privileged to focus on my education. These last years have been more difficult for us than any of the subjects in this dissertation, and unintelligible to the most. I am really sorry for not having always been physically present. I hope, however, that you will be proud of me.

Un grande pensiero va ai miei genitori, Luciana e Giulio, che mi hanno sempre supportato con amore. Fin da piccolo mi avete incoraggiato verso lo studio, l'apprendimento e la conoscenza. Grazie alla vostra guida e supporto, ho avuto il privilegio di potermi concentrare sui miei studi. Questi ultimi anni sono stati per noi più difficili di tutti gli argomenti di questa tesi ed incomprensibili ai più. Mi dispiace davvero di non essere stato sempre fisicamente presente. Spero, tuttavia, che possiate essere orgogliosi di me.

The final thank goes to myself and my virtues, which have allowed me to successfully carry out my education and research despite the many adverse circumstances.

Riccardo Ozzola
Delft, September 2024

About the Author

Riccardo Ozzola was born on February 18, 1994 in Bibbiena (Arezzo), Italy.

He received the BSc and MSc degrees, both with honors and the honorable mention from the committee, from the University of Florence, Florence, Italy, in 2017 and 2019, respectively. His master thesis project was developed at the Terahertz Sensing Group, Delft University of Technology (TU Delft), Delft, The Netherlands, where he started working in May 2020 as a PhD candidate.

His current research interests include the design of wideband phased arrays, the electromagnetic characterization of multiple-input and multiple-output (MIMO) systems, and the development of analytical and numerical methods for electromagnetics.

This research has been carried out under the supervision of prof. dr. ing. A. Neto and of dr. D. Cavallo as promotors. This has resulted in two phased array prototypes and an electromagnetic full-wave solver code, which yielded six journal publications, one paper currently under development, and sixteen contributions at international conferences. During his PhD, he co-supervised five MSc students, two of whom graduated *cum laude*. Furthermore, he was actively involved in several teaching and organizational tasks within the Terahertz Sensing Group's activities.

He was shortlisted for the Best Electromagnetics Paper Award at the European Conference on Antennas and Propagation (EuCAP) in Düsseldorf in 2021 and in Glasgow in 2024.

Riccardo Ozzola is a member of IEEE. He serves as a reviewer for the IEEE Transactions on Antennas and Propagation, and for the main conferences in antennas and applied electromagnetics.

List of Publications

Journal Papers

J.1 R. Ozzola, D. Cavallo, and A. Neto, "On the relation between beam coupling and feed coupling in wideband antenna arrays," *IEEE Trans. Antennas Propag.*, vol. 70, no. 1, pp. 260-267, Jan. 2022.

J.2 R. Ozzola, D. Cavallo, A. Freni, N. Llombart, and A. Neto, "A benchmark for the number of independent line of sight links on a given volume platform," *IEEE Trans. Antennas Propag.*, vol. 70, no. 12, pp. 12071-12080, Dec. 2022.

J.3 R. Ozzola, A. Neto, U. Imberg, and D. Cavallo, "Connected slot array with interchangeable ADL radome for sub-8 GHz 5G applications," *IEEE Trans. Antennas Propag.*, vol. 72, no. 1, pp. 992-997, Jan. 2024.

J.4 E. A. Speksnijder, R. Ozzola, and A. Neto, "Spectral domain Green's function of an infinite dipole with nonzero metal thickness and rectangular cross section," *IEEE Trans. Microw. Theory Tech.*, vol. 72, no. 8, pp. 4530-4541, Aug. 2024.

J.5 R. Ozzola, C. Tadolini and A. Neto, "Spectral domain analysis of lossy and nonzero thickness dipoles of finite length radiating in layered media," *IEEE Trans. Antennas Propag.*, to be published, doi: 10.1109/TAP.2024.3456966.

J.6 R. Ozzola, C. Tadolini, E. A. Speksnijder, and A. Neto, "Full-wave lens antenna analysis with the proxy sources method," *IEEE Trans. Antennas Propag.*, submitted for publication.

J.7 R. Ozzola, C. Tadolini, R. G. Tapia Barroso, D. Cavallo, and A. Neto, "Massive MIMO performance assessment of an ultrawideband phased array," *IEEE Trans. Antennas Propag.*, in preparation.

Conference Papers

C.1 R. Ozzola, D. Cavallo, A. Neto, "Efficiency analysis in multibeam wideband phased arrays," in *Proc. Eur. Conf. Antennas Propag.*, Copenhagen, Denmark, Mar. 15–20 2020.

C.2 R. Ozzola, A. Neto, U. Imberg, D. Cavallo, "Design of a wideband wide-scanning dual-polarized phased array for mobile communications," in *Proc. Eur. Conf. Antennas Propag.*, Düsseldorf, Germany, Mar. 22–26 2021.

C.3 R. Ozzola, D. Cavallo, A. Freni, N. Llombart, A. Neto, "The number of independent wireless links on a given volume platform," in *Proc. Eur. Conf. Antennas Propag.*, Düsseldorf, Germany, Mar. 22–26 2021.
Finalist for the Best Electromagnetic Paper award

C.4 R. Ozzola, Z. Chen, A. Neto, U. Imberg, and D. Cavallo, "Connected array design for mobile communications," in *Proc. IEEE Antennas Propag. Soc. Int. Symp*, Singapore, Dec. 4–10 2021.

C.5 R. Ozzola, Z. Chen, A. Neto, U. Imberg, and D. Cavallo, "2-8 GHz connected array for wireless base stations," in *Proc. Eur. Conf. Antennas Propag.*, Madrid, Spain, Mar. 27–Apr. 1 2022.

C.6 R. Ozzola, J. Geng, N. Llombart, A. Freni, D. Cavallo, and A. Neto, "On the use of the volumetric method of moments for the analysis and design of integrated feeds," in *Proc. Eur. Conf. Antennas Propag.*, Madrid, Spain, Mar. 27–Apr. 1 2022.

C.7 R. Ozzola, J. Geng, A. Freni, and A. Neto, "Full-wave solver for radiation from thermal sources," in *Proc. Int. Conf. Infrared Millim. Terahertz Waves*, Delft, The Netherlands, Aug. 28–Sept. 2 2022.

C.8 R. Ozzola, J. Geng, N. Llombart, A. Freni, D. Cavallo, and A. Neto, "A volumetric method of moments for integrated lens antennas," in *Proc. Int. Conf. Infrared Millim. Terahertz Waves*, Delft, The Netherlands, Aug. 28–Sept. 2 2022.

C.9 R. Ozzola, J. Geng, D. Cavallo, N. Llombart, A. Freni, and A. Neto, "On the use of the volumetric method of moments for THz applications," in *Proc. Eur. Conf. Antennas Propag.*, Florence, Italy, Mar. 26–31 2023.

C.10 R. Ozzola, R. G. Tapia Barroso, D. Cavallo, and A. Neto, "Study on the generation of independent beams from planar domains," in *Proc. Eur. Conf. Antennas Propag.*, Florence, Italy, Mar. 26–31 2023.

C.11 R. Ozzola, J. Geng, D. Cavallo, N. Llombart, A. Freni, and A. Neto, "A volumetric method of moments for the analysis of THz lens antennas," in *Proc. IEEE Antennas Propag. Soc. Int. Symp*, Portland, OR, USA, Jul. 23–28 2023.

C.12 R. Ozzola, R. G. Tapia Barroso, D. Cavallo, and A. Neto, "Generation of independent beams from arbitrary domains," in *Proc. IEEE Antennas Propag. Soc. Int. Symp*, Portland, OR, USA, Jul. 23–28 2023.

C.13 R. Ozzola, C. Tadolini, R. G. Tapia Barroso, U. Imberg, D. Cavallo, and A. Neto, "Design, measurements, and performance assessment of a massive MIMO wideband phased array," in *Proc. Eur. Conf. Antennas Propag.*, Glasgow, UK, Mar. 17–22 2024.

C.14 E. Speksnijder, R. Ozzola, and A. Neto, "Spectral domain Green's function of an infinite dipole with nonzero metal thickness," in *Proc. Eur. Conf. Antennas Propag.*, Glasgow, UK, Mar. 17–22 2024.
Finalist for the Best Electromagnetic Paper award

C.15 R. Ozzola, C. Tadolini, and A. Neto, "Spectral domain characterization of nonzero thickness dipoles in layered media," in *Proc. IEEE Antennas Propag. Soc. Int. Symp*, Florence, Italy, Jul. 14–19 2024.

C.16 R. Ozzola, C. Tadolini, E. Speksnijder, and A. Neto, "Reflection extraction with auxiliary sources method," in *Proc. IEEE Antennas Propag. Soc. Int. Symp*, Florence, Italy, Jul. 14–19 2024.

Co-Supervised Master Theses

T.1 Z. Chen, "Wideband feeding network design for dual-polarized connected arrays," M.S. thesis, Fac. EEMCS, Delft Univ. Technol., Delft, The Netherlands, 2021.

T.2 J. Geng, "Volumetric method of moments: a numerical tool for high frequency problems analysis," M.S. thesis, Fac. EEMCS, Delft Univ. Technol., Delft, The Netherlands, 2022.

T.3 R. G. Tapia Barroso, "Study on the number of independent beams from planar domains," M.S. thesis, Fac. EEMCS, Delft Univ. Technol., Delft, The Netherlands, 2023.

T.4 E. Speksnijder, “Development of spectral domain techniques for the analysis of printed transmission lines with nonzero conductor thickness,” M.S. thesis, Fac. EEMCS, Delft Univ. Technol., Delft, The Netherlands, 2023.

T.5 C. Tadolini, “On the modelling of the feeds for integrated lens antennas,” M.S. thesis, Fac. EEMCS, Delft Univ. Technol., Delft, The Netherlands, 2024.

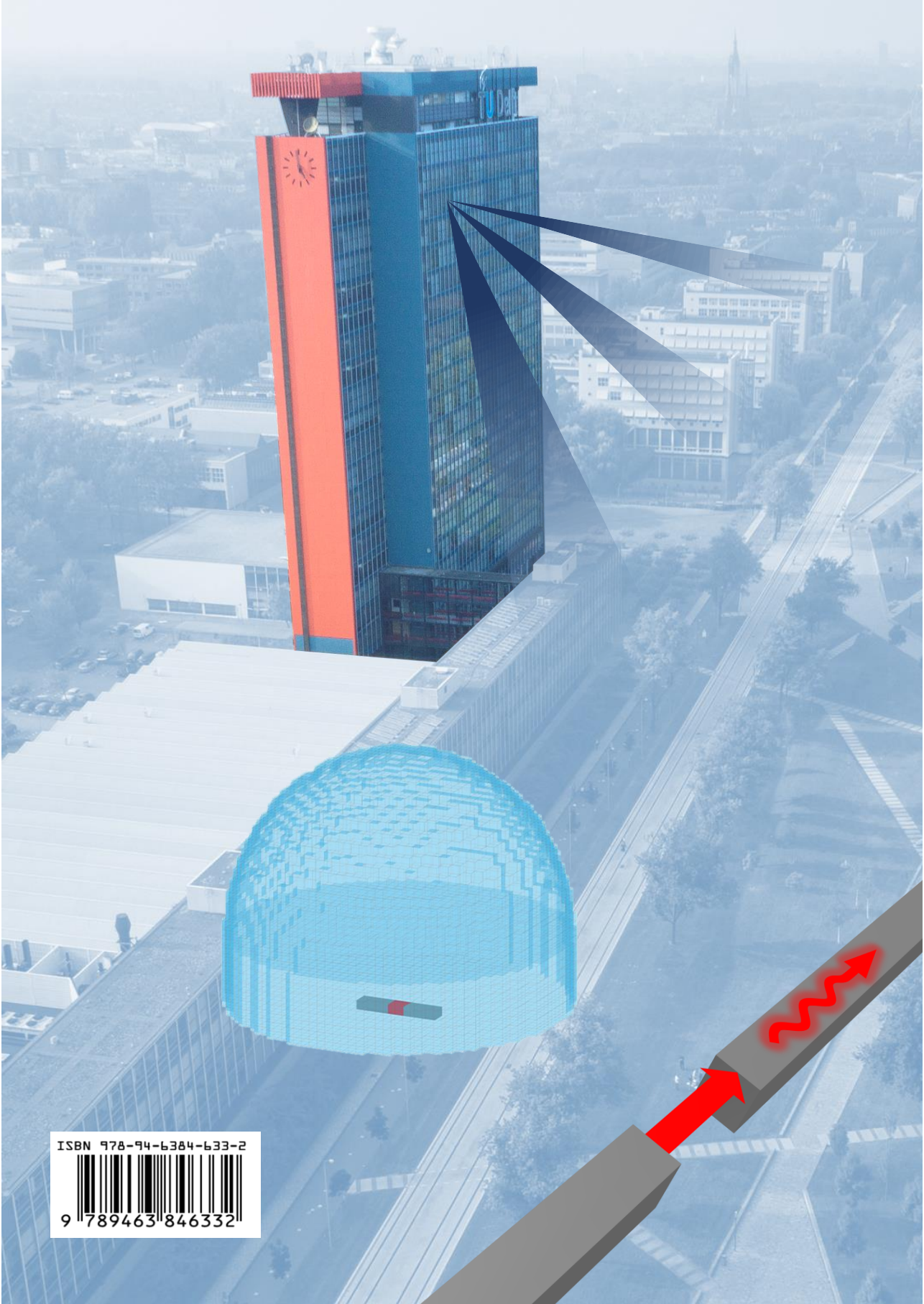

ISBN 978-94-6384-633-2